UNIVERSITY OF OKLAHOMA

GRADUATE COLLEGE

THE IMPACT OF SINGLE- AND MULTI-MOMENT MICROPHYSICS ON NUMERICAL SIMULATIONS OF SUPERCELLS AND TORNADOES OF THE 3 MAY 1999 OKLAHOMA TORNADO OUTBREAK

A DISSERTATION

SUBMITTED TO THE GRADUATE FACULTY

in partial fulfillment of the

Degree of

DOCTOR OF PHILOSOPHY

By

DANIEL THOMAS DAWSON II
Norman, Oklahoma
2009

THE IMPACT OF SINGLE- AND MULTI-MOMENT MICROPHYSICS ON NUMERICAL SIMULATIONS OF SUPERCELLS AND TORNADOES OF THE 3 MAY 1999 OKLAHOMA TORNADO OUTBREAK

A DISSERTATION APPROVED FOR THE
SCHOOL OF METEOROLOGY

BY

_____
Dr. Ming Xue, Committee Chair

_____
Dr. Frederick Carr

_____
Dr. Kelvin Droegemeier

_____
Dr. Alan Shapiro

_____
Dr. Jerry Straka

_____
Dr. S. Lakshmivarahan

DEDICATION

This dissertation is dedicated to my grandfather, Douglas Geib, who first ignited in me a passion for science.

ACKNOWLEDGEMENTS

The financial support for this research came mainly from the National Defense Science and Engineering Graduate Fellowship, the National Science Foundation Fellowship, and NSF grant ATM-0530814. Many of the simulations were performed on various supercomputers at the Pittsburgh Supercomputing Center (PSC), the Texas Advanced Computing Center, and the OU Supercomputing Center for Education and Research (OSCER).

As I have progressed through the graduate program in the School of Meteorology at the University of Oklahoma, and before that, my undergraduate years at Purdue University, it has become obvious to me that I can never rightfully claim satisfaction in my accomplishments without recognizing and acknowledging that all my efforts, at every step of the way, were supported and helped by so many friends colleagues and family members. A Ph.D., like any worthy pursuit in life, is never done in a vacuum. For starters, I wish to thank those that helped propel me on my path toward a Ph.D., even while I was an undergraduate student. Dr. Ernest Agee took me under his wing and supported me in my undergraduate research endeavors. More than that though, he became a good friend and a great encouragement to me. Thanks are also in order to my other professors at Purdue for their support and encouragement; among them are Drs. Phil Smith, Dayton Vincent, Carol Anne Clayson, and Grant Petty.

I wish to wholeheartedly thank my graduate research advisor, Dr. Ming Xue, who reached out to me when I was first accepted as an incoming M.S. student at OU. During the years, he has continually encouraged me, provided excellent research

advice and physical insight into difficult problems, but more than anything, gave me the freedom to carve out my own path, even if it meant the path was tortuous and uncertain at times. He has always had unflagging confidence in my abilities, even when I myself frequently doubted them.

To my Ph.D. committee members, I owe an immense debt of gratitude. Dr. Kelvin Droegemeier was one of the first professors I met when I first came to OU, and he immediately impressed me with his boundless enthusiasm for science. Dr. Frederick Carr provided helpful advice at many steps along the way. Dr. Jerry Straka was always willing to answer questions and discuss many issues related to the complex subject of cloud and precipitation microphysics, and the course he taught on this subject gave me the edge I needed to continue in my chosen line of study. Dr. Alan Shapiro provided many helpful comments on various aspects of my work, and we've had many interesting conversations over the years. Finally, it has been a delight to have Dr. S. Lakshmivarahan (or just Varahan to his friends and students) serve on my committee, and has always shown enthusiastic interest in my work. In turn, I learned a great deal from him in his Dynamic Data Assimilation class, which I count as one of the best courses I have ever taken.

I wish to thank Dr. Charles Doswell, who has become a good friend, for his scientific and moral support, in equal parts. He was never afraid to give me the "straight dope" about various aspects of graduate research, and has also given much helpful career advice. Our Friday night "quorums" have been one of the highlights of my experience here at OU. I thank Dr. Louis Wicker for many insightful conversations. I remember a significant turning point in my research occurred when,

showing him some results from my multi-moment simulations, he remarked simply, “I think you’re on to something here.” Thanks are also in order to Jim and Daphne LaDue, Celia Jones, and Marcia Palluto for their support and friendship. Scott Hill and Don Giuliano provided much help with the CAPS computer systems over the years, as has Henry Neeman and the other folks at OSCER, who also helped me with getting my many large computer simulations running smoothly. Finally, I wish to thank Dr. Jason Milbrandt for his patient answering of the many questions I had about his microphysics scheme which features prominently in this work, for his many encouraging emails, and for his collaboration on our conference papers and journal article related to this work. Without his help, and that of the others mentioned here, none of this would have been possible. Also, I owe thanks to Dr. Paul Markowski, whose work on RFD thermodynamics and tornadogenesis provided a significant source of inspiration for my work, and who has encouraged me in my pursuits.

Space does not permit me to thank in detail all my friends and fellow students from both school and church who have impacted my life over the years. Brad Barrett, Nate Snook, Youngsun Jung, Ming Hu, Andy Taylor, Aaron Botnick, and many others – thanks for your friendship. I owe a great debt of thanks to my dear friend and steadfast companion, Robin Tanamachi. Without her unflagging support and love over the years, always ready to dry a tear or rejoice with me in an accomplishment, I would not have made it this far, for which I thank God daily. My family has been a constant source of encouragement and love to me, which I could never hope to be able to repay. Mom and Dad and Grant, thanks for always encouraging me in my goals. My grandparents, aunts, and uncles on both sides of my

family have also always been there to support me. My aunt Aleta, in particular, who received her Ph.D. in sociology while I was growing up, was a significant inspiration to me due to her hard work and determination. My maternal grandfather, to whom this dissertation is dedicated, ignited a passion for science within me at an early age that has fanned into a mighty flame.

Finally, and most of all, concerning the One who saved me and brought me this far by His grace, the following words are embedded in my heart,

"…being confident in this, that he who began a good work in you will carry it on to completion until the day of Christ Jesus." – Philippians 1:6

TABLE OF CONTENTS

LIST OF TABLES

LIST OF FIGURES

ABSTRACT

Accurate parameterization of cloud and precipitation microphysical processes is critically important in simulation and prediction of severe convective storms, including supercell storms and their associated circulations. The 3 May 1999 Oklahoma tornado outbreak was characterized by several discrete tornadic supercells in relatively close spatial and temporal proximity, which in general displayed relatively weak and small cold pools. In this work, a sophisticated multi-moment bulk microphysics parameterization scheme capable of predicting up to three moments of the drop or particle size distribution (PSD) for several liquid and ice hydrometeor species is evaluated and compared with traditional single-moment schemes through numerical simulations of the 3 May 1999 event.

First, idealized simulations of this outbreak are conducted at horizontal grid spacings from 1 km down to 250 m, using a sounding extracted from a real-data simulation at 3 km grid spacing. The impacts of microphysics on cold pool strength and structure and on the overall reflectivity structure of the simulated storms are analyzed. It is shown through microphysics budget and trajectory analyses within the low level downdraft regions that the multi-moment scheme has several important advantages which lead to a much more realistic weaker and smaller cold pool and better reflectivity structure particularly in the forward flank region of the simulated supercells. Specifically, the improved treatment of evaporation and melting processes and their effects on the predicted rain and hail PSDs by the multi-moment scheme helps to control the cold bias often found in simulations using typical single-moment schemes. The multi-moment results are more consistent with observed

thermodynamic conditions within the cold pools of the discrete supercells of the 3 May 1999 outbreak.

Real-data simulations of this event down to 100 m horizontal resolution are performed, with an emphasis on the prediction of the Moore, Oklahoma F5 tornado produced by one of the supercells. The performance of the multi-moment microphysics scheme is tested and several issues are discussed in relation to the thermodynamic properties of the rear-flank downdrafts of the storms, which includes the tendency for the single-moment schemes to produce large temperature and moisture deficits in the rear-flank downdraft/hook echo region of the storm, as opposed to much smaller temperature and moisture deficits (and in some cases temperature excesses) seen in the multi-moment runs, which are much more consistent with mobile mesonet observations. The multi-moment simulations also in general produce a better prediction of the tornado track and intensity than the single-moment simulations; reasons for these differences are uncovered through analyses of the thermodynamic fields, terms in the vertical momentum equation and differences in the PSDs of rain and hail in the RFD/hook echo region of the simulated storms. The multi-moment simulations produce overall larger particle diameters for both rain and hail in the hook echo region, and have significantly less negative buoyancy in the near-tornado surface air, which is found to enhance tornadogenesis, whereas the strong negative buoyancy in the single-moment runs tends to suppress tornadogenesis. Finally, broader implications for numerical supercell tornado simulation and prediction are also discussed.

Chapter 1 General Introduction

1.1 Background and Motivation

Numerical simulation has historically been an important tool in examining the dynamics of supercell thunderstorms, successfully reproducing and explaining many features and behaviors. Supercell thunderstorms are those thunderstorms that can be characterized by a "deep, persistent mesocyclone" (Doswell and Burgess 1993), and they are responsible for a wide range of severe weather (often occurring simultaneously in the same storm), including damaging surface winds, large hail, lightning, flooding rains, and significant tornadoes. Early findings (and confirmation of theory and observations) from simulations of supercell behavior include the development of mid-level updraft rotation due to tilting of environmental horizontal vorticity into the vertical (Klemp and Wilhelmson 1978a), the phenomenon of splitting cells (Klemp and Wilhelmson 1978b; Wilhelmson and Klemp 1978; Schlesinger 1980; Wilhelmson and Klemp 1981), and the development of low-level rotation potentially associated with tornadogenesis (Klemp and Rotunno 1983). Other studies examined portions of the parameter space associated with storm types in regards to environmental shear and buoyancy (Weisman and Klemp 1982; 1984), in which supercells were found to dominate in environments of high CAPE and/or high environmental wind shear. Adlerman et al. (1999) explored the phenomenon of cyclic mesocyclogenesis, and later studies examined the impact of varying model resolution and physical and model-based parameters on the timing and evolution of this process (Adlerman and Droegemeier 2002; 2005).

One of the long-standing challenges in successful numerical simulation and prediction of supercells has been the parameterization of cloud and precipitation microphysics (MP), which is the particular focus of this study. Most numerical studies of supercells have relied on bulk MP parameterizations (hereafter BMP, or simply "scheme"), in which a certain functional form for the particle or drop size distribution (PSD or DSD) of one or more categories of cloud and hydrometeor species is prescribed. Many numerical modeling studies of supercells have focused on the impact of systematically varying microphysical parameters of a single-moment (SM) microphysics scheme (Johnson et al. 1993; Gilmore et al. 2004a,b, hereafter GSR04a,b; Cohen and McCaul 2006; Snook and Xue 2006; 2008). These studies have shown that simulated storm properties, including precipitation intensity and amount, propagation speed and direction, general storm morphology, and cold pool size and intensity, are very sensitive to the choices of these parameters. Such marked sensitivity to the microphysical parameterization has important implications for numerical prediction of supercells, impacts the interpretation of prior numerical studies of supercells, as well as fundamental understanding of the feedbacks of microphysical processes on supercell dynamics. Thus, this apparent deficiency in many current microphysics parameterizations is a primary motivating factor for this study.

Gilmore and Wicker (1998) showed in their idealized numerical supercell simulations that large and strong cold pools were produced as a result of mid-level dry air reaching the surface in the downdrafts, and that the drier the air, the stronger the cold pools tended to be, due to enhanced evaporation potential; this is one

example of the many feedbacks of microphysics to other storm processes. They used a simple warm-rain MP scheme and did not otherwise investigate the impact of microphysics. They also pointed out that the typical continental supercell environment was indeed characterized by a prominent mid-level dry air layer, which is attributed to the advection of a hot and dry mixed layer from the southwestern U.S. desert plateau over the top of a moist boundary layer (originating from the Gulf of Mexico) over the Great Plains.

With this in mind, it is surprising that many supercells, particularly the most tornadic ones, do not produce large and strong cold pools, at least not in the rear-flank downdraft (RFD) region (Markowski et al. 2002, hereafter MSR02). The impact of microphysics on thunderstorm cold pool behavior is important because the strength and size of the cold pool can potentially affect storm propagation, mode, longevity, interactions between storms, and tornadogenesis potential. In regards to the latter, MSR02 showed that significantly more strong tornadoes were associated with supercell thunderstorms that produced relatively warm and buoyant outflow, as opposed to many more nontornadic cases where storms were characterized by strong cold pools. However, experience has shown that many numerical simulations of supercells in typical continental environments produce cold pools that are too large and intense when typical SM MP schemes (mostly with exponential PSDs) are used with typical intercept parameter values (MSR02). Understanding the source of this bias, which is related to the aforementioned sensitivity issue, is another primary motivating factor for this study.

1.2 Overview of Dissertation

A common theme of most previous numerical studies of microphysical impacts on supercells is the use of a SM-BMP, in which an *a priori* fixed value for one of the distribution parameters for a given simulation is varied across several simulations. As will be discussed, however, these studies were most often concerned with other aspects of BMPs other than the effect of varying the PSDs, such as the effect of the number of ice hydrometeor categories, or different methods of computing various microphysical process rates. Usually, the parameter that is fixed is the intercept parameter N_0 of the exponential distribution, which most SM-BMPs assume for all precipitating categories. Observational studies have shown that N_0 varies considerably in time and space for convection (e.g., Waldvogel 1974). This suggests that more sophisticated *multi-moment* (MM) schemes that allow N_0 (and other PSD parameters, depending on the form of the distribution chosen) in time and space during the course of a simulation, may be more appropriate for the simulation of convection. For example, as pointed out by MY05a and Seifert (2008), theoretical considerations of certain microphysical processes, such as accretion, diffusion, and evaporation indicate that number concentration and mixing ratio can vary non-monotonically and that the assumption of constant N_0 in these cases is therefore invalid. To date, there have been very few studies that have examined the impact of MM schemes on supercell simulations. It will be shown in this study that the additional flexibility in the PSD parameters offered by a MM scheme effectively

removes some of the uncertainty associated with the need to pre-specify N_0, at least for the type of storm investigated: the tornadic supercell.

The over-arching purpose of this study, therefore, is to examine the impact of MM vs. SM microphysics on simulated supercell behavior, with an emphasis on the overall storm morphology (e.g., as revealed by radar reflectivity), on the low-level downdrafts and cold pools, and on the numerical prediction of the storms and associated tornadoes. As such, it focuses on the impact on variations in the PSDs, whereas most former studies have focused on other aspects of BMPs, as previously mentioned. The former two goals are accomplished mainly through idealized simulations, while the latter is examined through real-data experiments. The particular case examined in this study is the 3 May 1999 Oklahoma (OK) tornado outbreak, which contained many strong-to-violent tornadoes (Speheger et al. 2002, hereafter SDS02). This case was chosen primarily due to the observations of relatively small and weak cold pools, at least in the RFD region (Markowski 2002, hereafter M02), which in the light of the aforementioned connection of warm RFDs to tornadogenesis and the experience of a "cold bias" to most numerically simulated supercell RFDs, make it a particularly interesting and challenging case.

The numerical model used is the Advanced Regional Prediction System (ARPS, Xue et al. 2000; Xue et al. 2001; Xue et al. 2003), a multi-purpose nonhydrostatic numerical weather prediction (NWP) model. A sophisticated MM microphysics scheme (the MY scheme, Milbrandt and Yau 2005a,b, hereafter MY05a,b) has recently been interfaced with the ARPS model, and this scheme is compared and contrasted with other, more typically-used SM schemes.

This dissertation is organized as follows. Chapter 2 discusses fundamentals of bulk microphysical parameterizations, past microphysics impact studies on numerically-simulated convection, the implementation of several microphysical schemes (including both SM and MM schemes) within the ARPS model, and some of the relevant feedbacks from microphysics to grid-scale thermodynamic changes within convective storm simulations. Chapter 3 provides a brief overview of the 3 May 1999 OK tornado outbreak, from the synoptic scale down to the tornado scale, and discusses past observational and numerical studies of the event. In Chapter 4, a description of the results of an early attempt at real-data numerical simulations of the outbreak with the ARPS model are presented, in which simulations using the MY MM scheme are compared with SM schemes. An intermittent data assimilation strategy, in which multiple data sources are assimilated, is used. These data include surface and upper-air observations to analyze the storm environment, and radar reflectivity observations to analyze individual storms and build them up in the initial conditions of the model. Improvements in the prediction and structure of the storms, including the reflectivity and cold pool structure, when using the MM scheme are discussed.

Chapter 5 discusses a detailed idealized numerical modeling study of a supercell storm in a single-sounding environment taken from the real-data simulations in Chapter 4, and characteristic of that found in the 3 May 1999 outbreak. The focus is on the impact of microphysics and grid resolution on the evolution and behavior of the storms, and on comparisons with surface thermodynamic observations of the convective cold pools. In this study, several significant benefits of the MM schemes

over that of the SM schemes are revealed through detailed budget analyses of microphysical source and sink terms in the thermodynamic energy equation, and through the analysis of trajectories that pass through the low-level downdrafts and cold pools. These benefits include better representation of relevant physical processes, including the treatment of gravitational size-sorting and the effect of evaporation and melting on the PSDs. Simple 1D column model experiments are also performed to bolster these arguments.

In Chapter 6, results from real-data prediction experiments of the 3 May 1999 outbreak, with an emphasis on the main storm that produced an F5 (Fujita 1971) tornado in parts of Moore and Oklahoma City, OK, are presented. As in the experiments of Chapter 4, these experiments make us of an intermittent data assimilation approach in which multiple sources of data, including radar data, are assimilated. Experiments down to 250 m and 100 m horizontal grid spacing are performed in an attempt to resolve and predict the tornadic circulations, though only results from the 250-m experiments are discussed here. The choice of microphysics scheme (or variations in parameters in a scheme) is found to have a significant impact on the predicted storm behavior, including tornadogenesis. The advantages of MM in this case and implications for explicit prediction of supercells and tornadoes are discussed. Chapter 7 summarizes the dissertation and discusses broader implications of the results of this study for improved scientific understanding and numerical prediction of supercells and other convective storms. Future work is also discussed, in which more detailed analyses of the simulated tornadogenesis is planned, with an emphasis on the microphysics impact on the RFD thermodynamics, and in which the

interplay between the model microphysics and the data assimilation system will be explored in more detail.

Chapter 2 Single- and Multi-moment Bulk Microphysics Parameterization Schemes and Their Implementations in ARPS

2.1 Introduction to microphysics parameterizations and their use in convective storm modeling

The past few decades have seen an enormous expansion in the use of high-resolution numerical simulations to quantify and understand the behavior of small-scale deep convective systems. Invariably, these simulations have required some way of faithfully representing the extremely complex development and interaction mechanisms of various cloud and precipitation particles resulting from phase changes of water within cloud systems. In this section, we overview the main approaches used in storm-scale numerical simulation to represent this complex smorgasbord of cloud and precipitation processes, which collectively can be referred to as cloud and precipitation *microphysics*. The term *microphysics* is so used because the processes involved are in the microscale of atmospheric phenomena. Individual particles can range in diameter from a few microns for cloud droplets to several centimeters for large hailstones, but even the largest hailstones are far too small to be explicitly represented in numerical simulations of entire cloud systems on current computer hardware, in which typical horizontal and vertical grid spacings are on the order of tens of meters to several kilometers. Instead, *parameterizations* of the effects of the various hydrometeors on the grid-scale thermodynamics and dynamics within a numerical model have been employed.

Two basic types of parameterization schemes are commonly used: *spectral bin* and *bulk* schemes. Spectral schemes divide the size or mass distributions of a given category of hydrometeors within a certain volume (typically a grid cell volume)

into several size bins. The mass and number concentrations of particles within these size bins are then explicitly predicted (see, e.g., Seifert et al. 2006 for a description of the spectral bin approach and comparison with a bulk scheme). The shape of the particle (or drop) size distribution (PSD or DSD) is thus permitted to evolve over time and space and an *a priori* specification of the distribution is not needed. This flexibility is a primary advantage of the spectral approach. However, spectral schemes are typically very computationally expensive due to the requirement of the calculation of microphysical processes for many size bins, each with their own scalar conservation equation in the model. For example, the spectral bin model described in Seifert et al. (2006) requires a total of 264 model prognostic equations for the microphysics! Due to their high computational demand, studies using spectral schemes have mainly been limited to applications on the scale of individual clouds using a limited number of hydrometeor categories (but see Lynn et al. 2005a; b, for a recent study employing a spectral scheme with multiple ice categories within a mesoscale NWP model).

Bulk schemes, as compared to spectral schemes, are typically less accurate and require an *a priori* specification of the form of the PSD, but are also much more computationally feasible. This is because a single mathematical function is used to describe the entire distribution of particles for a given hydrometeor type in a grid cell, and one ore more moments of this function are predicted by the scheme. Thus, the hydrometeors within the grid cell are treated as a single "bulk" quantity. Due primarily to their relative simplicity and computational feasibility, most past numerical studies of convective storm dynamics have employed bulk schemes (or

bulk microphysics parameterizations; BMP). In the remainder of this section, we will discuss various aspects of BMPs in more detail.

2.1.1 Hydrometeor categories in BMPs

Within BMPs, hydrometeors are typically grouped into various categories, based mainly upon observed morphology (which is related to their microphysical history). The most commonly-defined categories of hydrometeors are cloud droplets, rain drops, pristine ice crystals, snow crystals and/or aggregates, and graupel and/or hail. Throughout the rest of this dissertation, the subscripts *c*,*r*,*i*,*s*,*g*, and *h*, respectively, will be used to signify these categories, as appropriate. Some examples of hydrometeor interactions that can occur within a convective cloud include: cloud droplet nucleation on aerosol particles, growth of cloud droplets by condensation and coalescence (possibly into rain-size particles) freezing of cloud and raindrops into ice particles, growth of snow crystals by vapor deposition, aggregation of snow crystals into snowflakes, conversion of snowflakes to graupel particles by riming of supercooled cloud droplets, production of hailstones from frozen rain or graupel nuclei, and many other interactions and processes. Many of these processes can occur essentially simultaneously within a small area of space and short time interval within a cloud.

Variations and subdivisions of the basic hydrometeor categories mentioned previously have been employed in various bulk schemes. Some of the earlier studies (e.g. Kessler 1969, hereafter K69) treat only liquid categories, while more recent schemes add various ice categories. One of the most widely-used of these is that introduced by Lin et al. (1983, hereafter LFO), which predicts mixing ratios of cloud,

rain, ice crystals, snow, and graupel/hail (i.e. graupel and hail, though recognized as different in nature, are treated as one category). Many subsequent BMPs are based on the LFO scheme and are currently used in various operational and research-oriented numerical models (e.g. Tao and Simpson 1993, hereafter LIN, GSR04b; Hong and Lim 2006).

Other schemes add other categories in addition to those used in LFO and variations (e.g. Ferrier 1994, hereafter F94; Walko et al. 1995; Meyers et al. 1997, MY05b). These latter schemes are similar in that all include both a hail and graupel category. Walko et al. (1995) and Meyers et al. (1997) also divide the "generic" snow category into snow and snow aggregates; the basic snow category consists of "relatively large ice crystals which have grown by vapor deposition and riming", while snow aggregates are considered to be amalgamations of the ice and snow categories. Even more recently (Straka and Mansell 2005, hereafter SM05), some researchers have introduced even more ice categories, for example choosing to differentiate between various densities of graupel, different ice crystal habits, and small and large hailstones.

2.1.2 Size distributions in BMPs

As mentioned previously, a BMP requires that the size distribution for a given hydrometeor category be pre-specified. Typically, the size distribution is written as a function of equivalent diameter according to $N_x(D) = f_x(D)$, where $N_x(D)$ is the number density as a function of particle diameter D, and $f_x(D)$ is the functional form specified. The equivalent diameter D can be specified in different ways. In some applications, it is considered to be the diameter a particle of a given volume or mass

would have if melted or formed into a perfect sphere of liquid water (see, e.g., Pruppacher and Klett 1978). In other applications, including in the BMPs examined in this study, D represents the equivalent ice sphere diameter at a given bulk density ρ_x, which is chosen to represent the density of the air-ice mixture characteristic of the ice hydrometeor category in question.

Based primarily on observational studies, particularly those of Marshall and Palmer (1948) and Gunn and Marshall (1958), the most common functional form of the size distribution employed by BMPs is the inverse exponential distribution, given by

$$N_x(D) = N_{0x} \exp(-\lambda_x D), \tag{1}$$

where N_0 is the intercept parameter, λ the slope parameter, and the subscript x is a placeholder for a given hydrometeor category. On a semi-logarithmic plot, the exponential distribution is a straight line with slope λ_x and y-intercept N_{0x}, which are the two free parameters of the function.

Equation (1) is a special case of a more general class of *gamma* distribution functions, a popular form of which can be written as

$$N_x(D) = N_{0x} D^{\alpha_x} \exp(-\lambda_x D), \tag{2}$$

where α_x is the shape parameter. Note that (2) reduces to (1) for $\alpha_x = 0$. Ulbrich (1983) suggested that the gamma distribution better characterizes many observed raindrop size distributions, and indeed, the additional free parameter allows more flexibility in describing the relative number concentrations of large vs. small drops in a given distribution, although the added complexity vs. additional benefit of moving to a gamma distribution has recently been brought into question by Smith (2003).

Fig. 2.1 (taken from Ulbrich 1983, Fig. 2) shows the gamma distribution for rain with the indicated values of liquid water content and median volume diameter for different values of α (μ in Ulbrich 1983). For positive values, the curve is concave down on a semi-logarithmic plot, with relatively smaller numbers of both small and large particles, while the opposite is true for negative values of α.

As discussed extensively by Pruppacher and Klett (1978), observed hydrometeor distributions invariably are only approximately modeled by either a gamma or exponential distribution, and furthermore, these are not the only possible functions that can be used to fit observed distributions – a lognormal distribution (see, e.g., eqn. 2-2 in Pruppacher and Klett 1978) is sometimes used. Nevertheless, the majority of BMPs use either (1) or (2), including those employed in the current study.

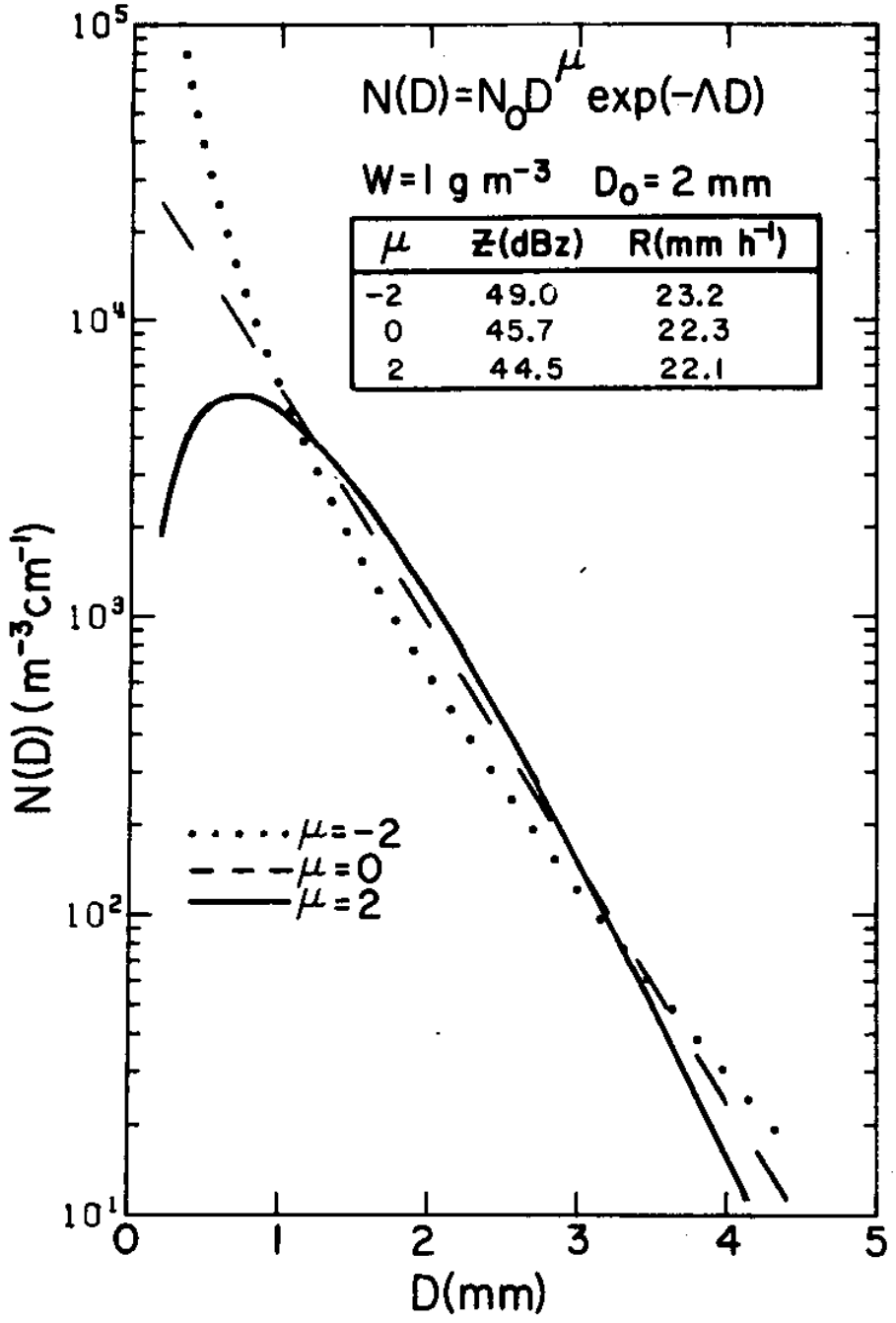

Fig. 2.1. Plot of the gamma size distribution for 3 values of the shape parameter (μ = α = -2, 0, and 2) for liquid water content W = 1 g m^{-3} and median volume diameter D_0 = 2 mm. From Ulbrich (1983).

2.1.3 PSD moments and sensitivity of simulated convection to parameters in SM schemes

Various properties of a distribution of hydrometeors can be elucidated by examining the moments of the distribution. After MY05b, the p^{th} moment of a general hydrometeor distribution is given by,

$$M_x(p) \equiv \int_0^\infty D^p N_x(D) dD \tag{3}$$

For a gamma distribution of the form (2), the p^{th} moment is given by,

$$M_x(p) = \frac{N_{tx}}{\lambda_x^p} \frac{\Gamma(1+\alpha_x+p)}{\Gamma(1+\alpha_x)}. \tag{4}$$

where N_{tx} is the total number concentration and Γ is the gamma function. For example, the mass mixing ratio q_x of a hydrometeor distribution is proportional to $M_x(3)$, the total number concentration N_{tx} is proportional to $M_x(0)$, and the radar reflectivity factor Z_x is proportional to $M_x(6)$.

In most BMPs that use the exponential distribution (1), the two free parameters are not independent of each other. Typically, one of the parameters (usually the intercept parameter N_{0x}) is fixed or diagnosed as a single-valued function of the other, and the hydrometeor mixing ratio q_x [proportional to $M_x(3)$] is predicted. This quantity can then be used, along with the fixed (or diagnosed) parameter, to determine the value of the remaining free parameter, thus closing the system. Such BMPs are known as single-moment (SM) schemes because only one moment of the DSD is predicted. For a given q_x, decreasing (increasing) N_{0x} leads to a relatively smaller (larger) number of small drops in the resulting distribution.

GSR04b demonstrated that both the qualitative (in terms of storm structure and evolution) and quantitative (in terms of cold pool area, strength, and precipitation type and intensity at the surface) results for a series of idealized multicell and supercell simulations using a SM-BMP are very sensitive to changes in the value of the intercept parameter for graupel/hail and the prescribed density of graupel/hail. They found that by varying the values of the intercept parameters for hail over the range of observed values in nature, widely different storm structure and precipitation characteristics resulted. For example, large values of the intercept parameter for graupel/hail (i.e., weighting the PSD toward small graupel) led to weak cold pools initially, primarily due to less precipitation reaching low-levels, but becoming stronger over time (i.e. toward the end of their 2-h integration). Smaller values of the hail intercept parameter (weighting toward large hail) led to initially stronger cold pools that peaked in intensity earlier. The strongest cold pools were found for the value of N_{0h} = 4.0 x 10^4 m^{-4} used in LFO. van den Heever and Cotton (2004) also demonstrated significant sensitivity in various simulated idealized supercell storm characteristics to proscribed changes in the characteristic (mean) diameter D_{nh} of the gamma hail distribution. Their results indicated that setting D_{nh} to smaller (larger) values led to overall stronger (weaker) cold pools, in contrast to GSR04b. GSR04b suggested this result as being due to more overall hail mass in the low-levels in the small D_{nh} (large N_{0h}) case of van den Heever and Cotton (2004) than in their runs. Snook and Xue (2006; 2008) further demonstrate that the presence or absence, intensity, and timing of tornadogenesis in a simulated supercell thunderstorm at high horizontal resolutions (100 m grid spacing) is strongly dependent on the values of the

intercept parameter of rain and hail. In particular, they found that cold pools were weaker and tornadogenesis was enhanced when the exponential rain and/or hail PSDs were biased toward larger particles (by setting N_{0x} to relatively small values).

2.1.4 Improvements over the SM fixed parameter approach

In light of the results of these studies, it is natural to seek methods by which the uncertainties inherent in the choice of the fixed parameter in a SM scheme might be reduced. In this section, we briefly outline a few common methods, ending with a description of the multi-moment (MM) approach, which is the main subject of this dissertation. The first method is to provide one or more diagnostic formulae that relate one or more free parameters in the DSD to another DSD-derived parameter. Typically, these formulae are based on functional fits to observations or detailed analytical models. This approach is followed by Zhang et al. (2008) in which a diagnostic relationship between N_{0r} and water content W is provided based on 2D video disdrometer observations of rain DSDs. Zhang et al. (2006) provided a diagnostic formula relating the shape parameter μ (same as α_x in the current study) to the slope parameter λ in gamma rain DSDs, also based on 2D video disdrometer observations. Thus, a "constrained-gamma" (CG) model was adopted in which the resulting gamma distribution, along with the diagnostic relation, has only two free parameters, just as in the exponential model (see also Ulbrich 1983 for a discussion on the empirical dependence of these two parameters). MY05a studied the effects of varying the shape parameter α_x in the gamma distribution on the sedimentation of hydrometeors using a simple 1D sedimentation-only model and argued that gravitational size-sorting is an important process in changing α_x due to the narrowing

of the size distribution. From these results, they provided diagnostic formulae that relate the shape parameter α_x of the gamma distribution to the mean-mass diameter D_m for several categories of precipitating hydrometeors. The mean-mass diameter D_m, which is defined as the diameter of the drop with the average mass of the distribution, and will be discussed more later, is given by (after MY05a, eqn. 10),

$$D_{mx} = \left[\frac{\rho q_x}{c_x N_{Tx}} \right]^{1/d_x} \tag{5}$$

where ρ is the air density, and c_x and d_x are constants in the mass-diameter relationship for a given particle category x (i.e., $m_x(D_x) = c_x D_x^{d_x}$).

The common motivation for adopting this approach is to reduce the number of free parameters in the assumed DSD in a manner that is constrained by empirical data. It also has the advantage of being straightforward to apply to existing microphysics parameterizations and thereby avoiding the problem of having to choose the "proper" value of these parameters, such as the intercept parameter in SM schemes.

Another approach to improve upon existing SM-BMPs is to increase the number of hydrometeor categories represented in the model. McCumber et al. (1991), after evaluating several 3-class and 2-class bulk ice schemes, recommended this approach, suggesting that at least 4 ice categories be included in future bulk schemes, particularly including separate graupel and hail categories. Indeed, Ferrier et al. (1995) found that splitting the traditional graupel/hail category into two separate categories improved the prediction of a numerically-simulated squall line. This is also the approach taken by SM05, in which, as previously mentioned, several

subcategories of ice crystals, graupel, and hail are defined, each with their own densities and fixed DSD parameters. SM05 argue that this approach provides greater flexibility by parameterizing a larger range of the types of ice hydrometeors actually encountered in real cloud systems of many types (i.e. tropical vs. continental) and to thus reduce the amount of case-specific "tuning" required (SM05). The original version of the scheme described in SM05 was SM, but the authors indicate that future versions would include double-moment (DM) capability, by providing for prognostic equations for number concentration. They point out that predicting more than one moment of the distribution for a given hydrometeor category would have a similar effect in reducing the amount of "tuning" required as increasing the number of categories. We now turn to a discussion of this *multi-moment* (MM) approach.

In light of the above discussion, one might wonder whether a BMP that allows the intercept parameter to vary naturally both temporally and spatially during the course of the simulation might serve to reduce or eliminate the aforementioned sensitivity problem (particularly the well-documented sensitivity to the prescribed N_{0x} in SM schemes). DM BMPs are often employed for this purpose. Most DM-BMPs predict both mixing ratio and total number concentration (e.g., Ziegler 1985; Nickerson et al. 1986; Murakami 1990; Wang and Chang 1993, F94; Meyers et al. 1997, MY05b). The total number concentration N_t is proportional to the 0^{th} moment of the distribution. Since two moments of the distribution are predicted, both free parameters in an exponential distribution are allowed to vary independently, which should lead to more realistic spatial and temporal variation of N_{0x} and associated improvement in the prediction of storm structure and precipitation, provided the

parameterized microphysical processes are sufficiently accurate and the exponential (or gamma) distribution faithfully represents true hydrometeor size distributions. It should be emphasized that the MM method is different from the previously-mentioned method of providing diagnostic formulae to relate the two free parameters in the exponential DSD to each other. In that method, the two parameters are not actually independent of each other: given the value of one, the value of the other can be uniquely determined. This is more restrictive than the MM approach, in which the two parameters can vary independently. This greater flexibility comes at the cost of more computational demand associated with the requirement of providing prognostic equations and equations for the process rates for the additional predicted moment(s).

Recently, multi-moment (MM) schemes have enjoyed increasing popularity in cloud and storm modeling (Ferrier et al. 1995; Meyers et al. 1997; Reisner et al. 1998; Seifert and Beheng 2001; 2006; Seifert et al. 2006; Mansell 2008; Morrison et al. 2008). As examples, Ferrier et al. (1995) and Morrison et al. (2008), examined the impact of a DM scheme on simulations of idealized 2D squall lines, and found that N_{0r} varied significantly between the convective and stratiform regions of the system, with the stratiform region typically having smaller N_{0r} than the convective region, and thus, reduced evaporation rates in this region compared to the fixed-N_{0r} SM scheme. This yielded a much better representation of the stratiform rain region in the DM scheme than in the SM scheme. Mansell (2008) compared DM and SM schemes for ensemble Kalman filter (EnKF) experiments for a tornadic supercell storm and noted a better representation of the cold pool structure and forward flank reflectivity region of the supercell when using the DM scheme. The results of these studies suggest that

allowing more parameters of the various hydrometeor DSDs to vary independently in time and space, as in MM schemes, improves the overall simulation of convective storms, with much less case-specific "tuning" of the parameters necessary.

As mentioned previously, some BMPs utilize a gamma distribution for one or more categories, of which the exponential distribution is a special case (with $\alpha = 0$). The use of a gamma distribution instead of an exponential distribution means that an additional parameter (α) has to be determined. In a DM-BMP, this parameter must be pre-specified or diagnosed (as in the case of the diagnostic-α relations of MY05a discussed previously). A triple-moment (TM) scheme allows for this parameter to vary independently. The MY-TM scheme (MY3) predicts mixing ratio, number concentration, and radar reflectivity for most microphysics categories, and thus allows all three free parameters in the gamma distribution to vary independently in time and space during the course of a simulation. This scheme will be discussed in more detail in section 2.3 of this chapter.

2.2 Single-moment schemes in ARPS

The ARPS contains several SM BMPs available as options to the user. These include the K69 warm-rain scheme, the Lin-Tao 3-ICE (LIN) scheme (LFO, Tao and Simpson 1993), the WRF Single-moment 6-class (3 ice, 2 liquid, 1 vapor) microphysics scheme (WSM6, Hong and Lim 2006), the Schultz NEM scheme (Schultz 1995), the GSR04b version of the LFO scheme, and the SM version of the MY05b scheme (MY1). In this study, we will only examine the LIN, WSM6, and the MY05b schemes. The WSM6 scheme is further divided into the original fixed-N_{0r} formulation and a formulation where the intercept parameter for rain, N_{0r}, is diagnosed as a function of liquid water content (WSM6DN0R), based on fitting to disdrometer observations (Zhang et al. 2008). Otherwise, the ARPS input namelist allows the user to specify values of N_{0x} for a given model run for each of the precipitating categories in these schemes where applicable. In addition, the LIN scheme includes a hail category, but not a graupel category; the WSM6 scheme includes a graupel category, but not a hail category; the MY1 scheme includes both. All other hydrometeor categories are common across the 3 schemes. In the case of the LIN scheme, the values of N_{0r}, N_{0s}, and N_{0h} (as well as the densities of these hydrometeors) can be specified, while ice crystals are assumed to be monodisperse. In the WSM6 scheme, N_{0r} and N_{0g} may be specified, but N_{0s} is diagnosed as a function of temperature using the relation $N_{0s} = 2\times10^{6}\exp\left[0.12(T - T_0)\right]$, where T and T_0 = 273.16 K, are the temperature and reference temperature, respectively. In

the WSM6DN0R scheme, N_{0r} is given as a function of q_r by $N_{0r} = 7.8355 \times 10^6 (1000 \rho_a q_r)^{0.681}$ (see Zhang et al. 2008 for an updated formula). In addition, in the WSM6 schemes, the total number concentration of ice N_{ti} is diagnosed as a function of q_i by the formula $N_{ti} = 5.38 \times 10^7 (\rho_a q_i)^{0.75}$ (Hong et al. 2004, Eq. 5c).

The code subroutines for each of these schemes are called within the model after the state variables have been updated through the advective, diffusive, and other physical processes. In other words, the microphysics scheme is the last physical process computed in a given time step. The microphysics scheme updates the future values of the microphysics state variables, that is, those valid at the third time level of the three-time-level leapfrog time integration scheme used within ARPS. In addition, the schemes modify the potential temperature field based on the various microphysical processes relating to phase changes of water and associated heating and cooling.

As discussed previously, all of these schemes are based on the assumption that the distribution of precipitating hydrometeors can be represented by an exponential or gamma distribution. In particular, the LIN and WSM6 schemes both assume an exponential distribution for all precipitating hydrometeors (r,s,g/h), while the MY1 scheme uses a gamma distribution and can be configured with a fixed value of α for any of the precipitating water and ice categories (r,i,s,g,h).

2.3 Milbrandt and Yau multi-moment scheme

2.3.1 Scheme overview

In addition to the SM schemes mentioned previously, a new MM scheme has recently been interfaced with the ARPS model, the scheme described in MY05a,b. The MY scheme is a 4-class ice (ice crystals, snow, graupel, and hail), 2-class liquid water (cloud and rain) bulk parameterization, in which all precipitating hydrometeors are assumed to have gamma-DSDs of the form (2). Up to three moments of the size distribution are predicted, including the mixing ratio (proportional to the 3rd moment), the number concentration (proportional to the 0th moment), and radar reflectivity factor (proportional to the 6th moment) for all categories except for cloud droplets, for which reflectivity, being negligible, is not predicted. In this manner, for the full TM version of the scheme, all of the three free parameters of the gamma distribution (N_0, λ, and α) are allowed to vary independently. For the SM scheme, both N_0 and α are fixed at constant values *a priori* for all precipitating categories except ice crystals, in which N_{0i} is diagnosed from the temperature-dependent number concentration of ice crystals (N_{ti}) given by the Cooper equation (Cooper 1986) as $N_{ti} = 5.0\exp\left[0.304(T_0 - T)\right]$ (in the DM and TM schemes, this equation is not used: N_{ti} is explicitly predicted) . In the basic DM scheme, only α needs to be fixed, as q_x and N_{tx} are predicted for all categories. In addition, a version of the DM scheme is provided in which the shape parameter α is diagnosed as a function of the mean-mass diameter D_m for all precipitating categories (that is, all categories except cloud, which is assumed to have negligible terminal velocity), based on comparisons with an

analytical model for pure sedimentation (MY05a). This version of the DM scheme will hereafter be referred to as the MY2DA scheme.

2.3.1.1 Consistency between moments and interfacing with model numerics

A unique challenge that arises when interfacing a MM microphysics scheme with an existing model's numerical treatment of advection and diffusion, as opposed to a SM scheme, is the problem of maintaining consistency between each of the predicted moments for a given category, when the conservation equation for each moment is integrated numerically by the model. In the MY scheme, each of the (potential) predicted moments, q_x, N_x, and Z_x, are by physical definition non-negative quantities, with units of kg kg^{-1}, m^{-3}, and m^3, respectively (note that Z_x is expressed in linear rather than the logarithmic units of *dbZ*). The conservation equations for each (not shown) contain terms for advection and turbulent mixing. The ARPS model has options for 2nd-order and 3 different 4th-order centered-in-space numerical advection schemes (Xue et al. 2003). Due to the even-ordered nature of the basic 2nd-order and 4th-order schemes, the leading term in the truncation error can be shown to be dispersive in nature. A consequence of this is that the development of regions of negative values of positive definite (or positive semi-definite) quantities such as the microphysical moments in the MY scheme are possible due to unphysical small-scale dispersive noise being produced as a result of the truncation error. This is especially true if the advected quantity at a given grid point has a small absolute magnitude, which increases the probability that the small scale dispersive waves will produce oscillations that reduce the advected quantity below zero. As might be expected, this would happen most often at the edges of cloudy regions.

In the SM BMPs in ARPS, the problem is typically handled (albeit in a somewhat *ad hoc* manner) by simply setting any negative values of the hydrometeor fields to zero before passing them to the microphysics subroutine. In the MM scheme, however, the problem is exacerbated because, in certain circumstances, the local value of one of the predicted moments for a given quantity (e.g. the mixing ratio of rain q_r), may have a physically-reasonable positive quantity after being advected, while the value of another moment (e.g., the number concentration for rain N_{tr}) at the same grid point may actually be negative. In other words, it is possible for physical inconsistencies between two moments of the hydrometeor distribution to arise due to the numerical truncation error in the advection scheme. One way of handling this is the same as in the SM scheme, namely clipping all predicted moments to zero at a particular grid point if any of them are found to be negative (or below a certain minimum threshold set ahead of time). This is in fact, what is done in the current implementation of the scheme in the ARPS. However, experience has shown that such wholesale clipping, which usually happens most often along the edges of the cloud (or rain, hail, etc.) regions can lead to solution-destroying or noisy behavior in the model hydrometeor fields even though the clipped hydrometeor mass is added back to the water vapor field in an effort to conserve total water mass.

In light of this, experience has also shown that the use of the flux-corrected-transport (FCT, Zalesak 1979) 4^{th}-order forward-in-time advection scheme for scalars significantly mitigates the above issues by ensuring that no negative values of positive definite quantities are produced by the advection scheme in the first place (that is, the scheme is monotonic). Skamarock and Weisman (2009) found significant

improvement when using a similar positive-definite (PD) scalar advection scheme on predicted precipitation amounts in convection-resolving Advanced Research-Weather Research and Forecasting (WRF-ARW, Skamarock et al. 2005) model forecasts; the too-high precipitation bias was significantly reduced owing to the elimination of the need to clip negative values. To illustrate some of the benefits of using a monotonic advection scheme when a MM microphysics scheme is used, Fig. 2.2 shows a comparison between two experiments with the MY2DA scheme using the default supercell test case in ARPS, an idealized simulation of the 20 May 1977 Del City tornadic supercell, which is a staple of several previous numerical studies (Klemp et al. 1981; Klemp and Rotunno 1983; Grasso and Cotton 1995; Adlerman et al. 1999; Adlerman and Droegemeier 2002; 2005a; b). The figure shows surface fields of equivalent radar reflectivity and water vapor mixing ratio at 45 min into the simulation. One experiment (Fig. 2.2a) used the default 4^{th}-order scalar advection option in ARPS, while the other (Fig. 2.2b) used the FCT 4^{th}-order advection scheme. Clearly, the use of the FCT advection scheme produces a solution that is much more noise-free, particularly in the region just northeast of the hook echo near the edge of the forward flank. The experiment in Fig. 2.2a became unstable shortly after the time shown in Fig. 2.2.

In addition to the problems inherent in the advection schemes, the 4^{th} and 6^{th}-order computational mixing schemes available in ARPS (Xue et al. 2003) are also capable of producing negative values of positive definite quantities for similar reasons. However, the ARPS also contains options for monotonic versions of the 4^{th} and 6^{th}-order computational mixing schemes (Xue 2000). These schemes were found

to be very helpful in reducing additional small-scale noise and oscillatory behavior (particularly in regions of large gradients of hydrometeor fields) still leftover after the application of FCT advection and that was most apparent in the DM and higher microphysics simulations. From these results, it is recommended that care be taken in choosing sufficiently accurate and/or monotonic numerical advection and mixing schemes when using multi-moment microphysics parameterizations. In the future, further sensitivity tests will be performed in an effort to better quantify the benefits of using monotonic advection and mixing schemes in combination with a MM microphysics scheme.

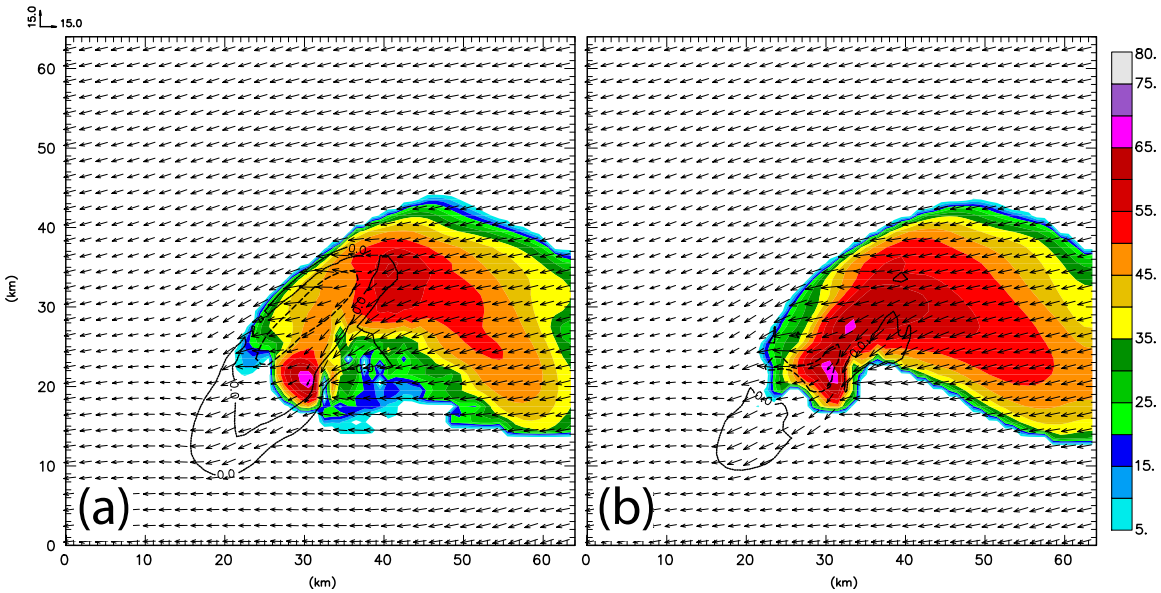

Fig. 2.2. Surface equivalent radar reflectivity (color fill), perturbation water vapor specific humidity (black contours, 2.0 g kg^{-1} increment) and wind vectors (plotted every 2 km, scale in m s^{-1} at upper-left) at 45 min (2700 s) for the idealized 20 May 1977 Dell City supercell simulation with a) default (non-monotonic) 4th-order scalar advection, and b) FCT 4th-order scalar advection.

2.3.2 Previous studies applying the MY scheme

Due to the relatively new nature of the MY scheme, there have been few published studies applying the scheme to the simulation of deep convection.

Milbrandt and Yau (2006a; 2006b, hereafter MY06a,b), as parts III and IV of their series of papers introducing their new scheme, interfaced it with a mesoscale model, the Canadian Mesoscale Compressible Community model (MC2), and performed real-data simulations of the 14 July 2000 large hail-producing supercell thunderstorms in Alberta, Canada. Nested grids down to 1 km horizontal grid spacing for the smallest grid were employed. In MY06a, the goal was to compare the observed reflectivity structure and observed maximum hail sizes at the ground with the simulated reflectivity and surface hail sizes, as a means of validating the full TM version of the scheme. It was found that the simulated and observed storms, despite having some differences in propagation direction and locations, were very similar to each other in both the reflectivity structure and surface hail fall fields. In addition, MY06a found that the observed golf-ball sized hail was consistent with the simulated maximum "physically observable" hail sizes reaching the surface in their TM control simulation. The values of mixing ratio and number concentration for the various hydrometeor categories (i.e. cloud, rain, ice, snow, graupel, and hail) in their simulation were shown to be consistent with the range of published observed values.

MY06b performed sensitivity tests of the SM, DM, and TM versions of the scheme for the same supercell case in MY06a. Two SM configurations, one with a fixed value of N_{0h} (as well as the intercept parameters for the other categories), and one with a diagnostic relation for N_{0h} as a function of λ_h were tested. Four DM configurations, one with a fixed $\alpha = 3$, one with a fixed $\alpha = 0$, and two with two different formulations of the diagnostic α relation introduced in MY05a were tested. The results indicated that the DM schemes were all fairly successful at reproducing

most of the salient features of the TM simulation, with the DM schemes with diagnostic α performing the best. On the other hand, the SM schemes were both significantly worse than the DM schemes at reproducing the TM storm characteristics. For example, the SM scheme with fixed $N_{0h} = 1.0 \times 10^4$ m^{-4} (i.e., characteristic of graupel-sized particles, SM_A) dramatically over-predicted the cold pool strength of the simulated storm, whereas the SM scheme with diagnostic N_{0h} (i.e. more characteristic of large, high-density hail, SM_B) significantly under-predicted it (Fig. 2.3). It was shown, in fact, that the maximum physically-observable hail sizes in the SM_B simulation approached the diameter of a basketball (24 cm)! These results are consistent with previously discussed sensitivity studies (van den Heever and Cotton 2004, GSR04b; Snook and Xue 2006; 2008) in which varying the hail size distribution parameters to favor small (large) hailstones resulted in weaker (stronger) cold pools in simulated deep convective storms. In summary, MY06b found that a dramatic improvement in simulated storm characteristics was seen (taking the full TM control run as "truth") in moving from SM to DM schemes, with comparatively less, but still significant, improvement in moving from fixed-α to diagnostic-α versions of the DM scheme.

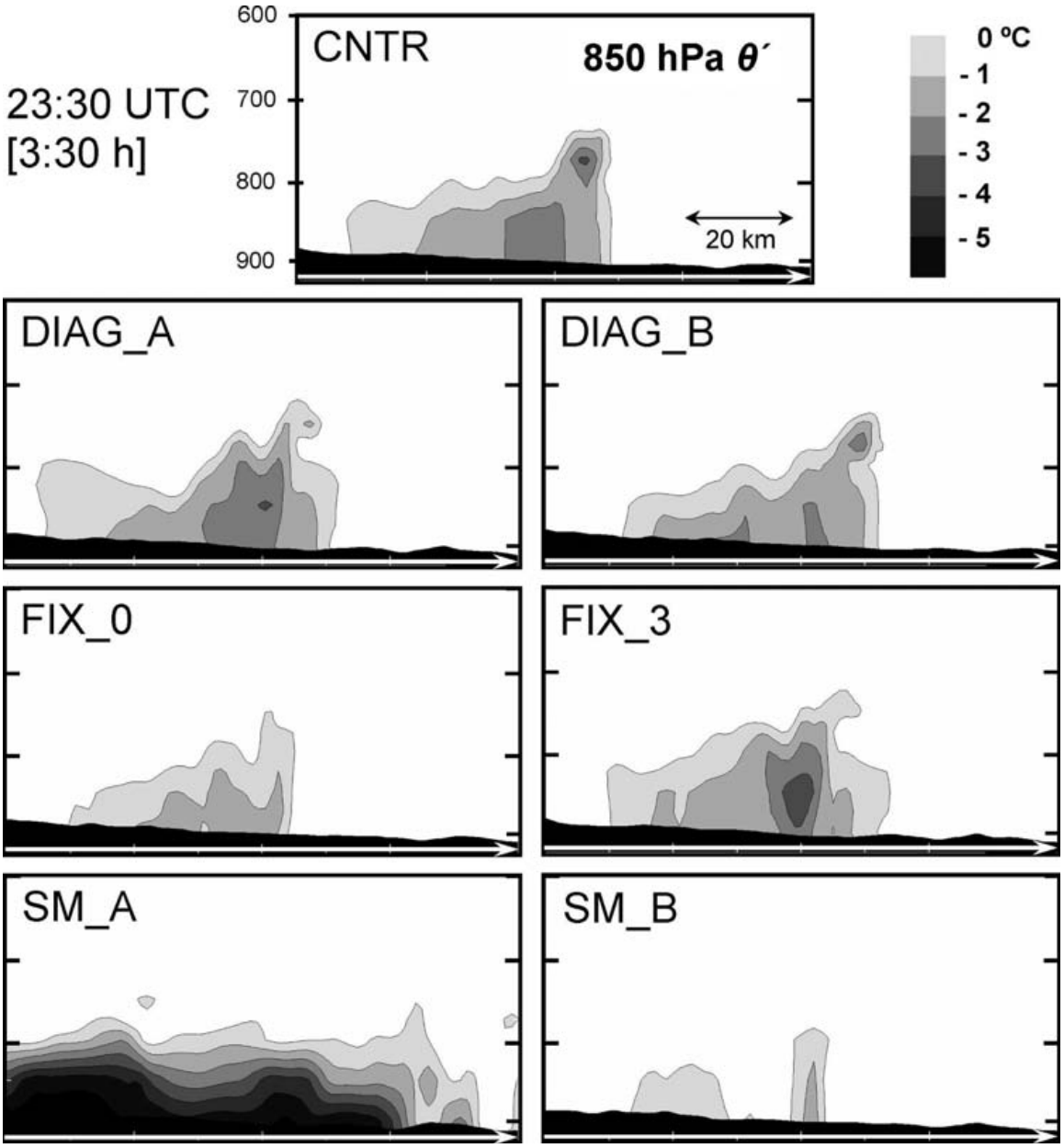

Fig. 2.3. Vertical cross section through the simulated supercell cold pool in each of the sensitivity tests in MY06b, showing θ' contours in increments of 1 °C. From MY06b Fig. 10.

2.3.3 Comparison with the ARPS LIN scheme and relevance to downdraft and cold pool forcing

For many microphysical processes, the MY scheme follows the formulations of LFO, and are similar or identical to the corresponding processes in the ARPS SM LIN scheme. For the sake of brevity, we will focus in this section on those processes that are likely to be most relevant to the enhancement of convective downdrafts and cold pools. Straka and Anderson (1993), for example, found that the processes most significant to the enhancement of downdrafts within simulated microburst-producing storms were precipitation loading from rain and graupel/hail, melting of graupel/hail, and evaporation of rain. Melting and sublimation of snow and ice crystals were found to have a much smaller impact. In the current study of simulated supercell storms, evaporation of cloud was also found to be significant, and, depending on the scheme used, collection of rain by hail as a counter-acting heating effect in the downdrafts was also found to be important[1]. These results will be discussed in more detail in Chapter 5. We now turn to a discussion of the formulation of these processes and similarities and differences between the LIN and MY schemes.

[1] It is possible that cloud evaporation was not as significant in the study of Straka and Anderson (1993) due to the relatively weak wind shear profiles and moist mid-levels in the thermodynamic profiles used in their simulations, which would tend to reduce the entrainment of dry air into the clouds before significant scavenging of cloud water by precipitating hydrometeors could take place. In the case of the classic supercells in this study, strong storm-relative mid-level winds transporting dry air into the sides of the updrafts would tend to result in comparatively larger amounts of cloud evaporation.

2.3.3.1 Cloud evaporation

In LIN, cloud evaporation is treated with a saturation adjustment process (Tao et al. 1989), in which all cloud is allowed to evaporate into subsaturated air until saturation is reached or cloud water is depleted, before any rain present at a particular grid point is allowed to evaporate. The technique uses a weighted average between the saturation vapor mixing ratio with respect to water and that with respect to ice in a range of temperatures below freezing, and requires that the adjustment, which is assumed to take place completely in one time step, to proceed moist-adiabatically.

In the MY scheme, the saturation adjustment technique of Kong and Yau (1997, Appendix A) is used to determine the amount of condensation or evaporation allowed in one time step of the model. From Kong and Yau (1997) equation A7, we have

$$X = -\Delta q_v = \frac{q_v^* - q_{vs}^*}{1 + \dfrac{4098.17 q_{vs}^* L_v}{c_p (T - 35.86)^2}} \tag{6}$$

where X is the capacity of condensation or evaporation for one time step of the model, q_v^* and q_{vs}^* are the water vapor mixing ratio and saturation water vapor mixing ratio before the adjustment, respectively, L_v is the latent heat of vaporization of water, c_p is the specific heat at constant pressure of dry air, and T is the air temperature. (6) is derived based on the conservation of equivalent potential temperature during saturation adjustment. Similar to the adjustment technique of Tao et al. (1989), if $X < 0$ at a grid point, evaporation is indicated, and any cloud water (q_c) present at the grid point is transferred to vapor up to the amount allowed by the magnitude of X. If the

air is still subsaturated after all available q_c is exhausted, and rain water (q_r) is also present, evaporation of rain takes place, to be discussed in the next section.

2.3.3.2 Rain evaporation

Instead of the instantaneous saturation adjustment approach used in both the LIN and MY schemes, the rain evaporation rate is calculated explicitly in both schemes. In this section, we will concentrate on a description of the process in the MY scheme, since the approach in the LIN scheme is very similar.

For rain evaporation, MY05b uses the following formulation (Eqs. 7, 8, and 9 in MY05b):

$$QVD_{vr} = \frac{2\pi(S_w - 1)N_{0r}VENT_r}{AB_w} \quad (7),$$

$$\mathrm{VENT}_r = A_r \frac{\Gamma[2+\alpha_r]}{\lambda_r^{2+\alpha_r}} + B_r S_c^{1/3} \left(\frac{\gamma a_r}{\nu}\right)^{1/2} \frac{\Gamma(2.5+\alpha_r+0.5b_r)}{\lambda_r^{2.5+\alpha_r+0.5b_r}} \quad (8),$$

$$AB_w = \frac{L_v^2}{K_a R_v T^2} + \frac{1}{\rho q_s \psi} \quad (9),$$

For the definition of symbols, and a more thorough discussion of the nomenclature for the process rates, see MY05b. In brief, the nomenclature for the process rates discussed in this study follows that of MY05b and is as follows: *Q* represents a mixing ratio rate, *VD* represents a vapor diffusion process, *ML* a melting process, and *CL* a collection process. The subscript symbols represent the transfer from one category to another (i.e., *vr* represents transfer to/from vapor and rain, *hr* from hail to rain, etc.). The bulk rain evaporation rate equation (7) is derived by first considering the rate of change of diameter due to evaporation in a subsaturated environment of a single drop falling at its terminal velocity (see, e.g., Byers 1965;

Rogers and Yau 1989). The resulting equation is then integrated over all drop sizes in the distribution given by (2) or (1) to yield the bulk evaporation rate in terms of change of mixing ratio q_r with time (Orville and Kopp 1977). The ventilation coefficient $VENT_r$ takes into account enhanced evaporation effects due to air flowing past drops as they fall at their respective terminal velocities, and is empirically-based (see Pruppacher and Klett 1978). For a stationary (relative to the air) population of drops, $VENT_r$ is unity.

One significant property of Eqn. 7 for the purposes of this study is the fact that the evaporation rate (QVD_{vr}) is directly proportional to the intercept parameter N_{0r} (for a fixed slope parameter λ_r and shape parameter α). Note, however, that λ_r is a function of N_{0r} when q_r and α are fixed, as they are in the following example for the purposes of illustration, so that the ventilation factor leads to departure from direct proportionality. Fig. 2.4 shows evaporation rates as a function of N_{0r} for the exponential case, normalized by the rate calculated with $N_{0r} = 8.0 \times 10^6$ m^{-4}. Other parameters fixed for the purposes of the rate calculations are $q_r = 0.001$ kg kg^{-1}, a temperature of 288.15 K (15 °C), an air pressure of 850 hPa, yielding an air density of ~1.03 kg m^{-3}. (The saturation ratio S and the thermodynamic function AB_w drop out due to the normalization, but the above parameters of T, p, and ρ still need to be set since they impact the relative importance of the two terms in the $VENT_r$ calculation in Eqn. 7). As can be seen, larger (smaller) values of N_{0r} lead to larger (smaller) rates of evaporation for the same q_r. Recall that a large intercept parameter is associated with greater numbers of smaller drops (for the same mixing ratio), which evaporate more efficiently due to greater surface area-to-volume ratio than that of larger drops, which

are associated with smaller values of the intercept parameter (e.g. see the discussion in Snook and Xue 2006; 2008). Thus, an *a priori* specification of N_{0r} in a single moment scheme will significantly and universally affect the evaporation rate, all other things being equal.

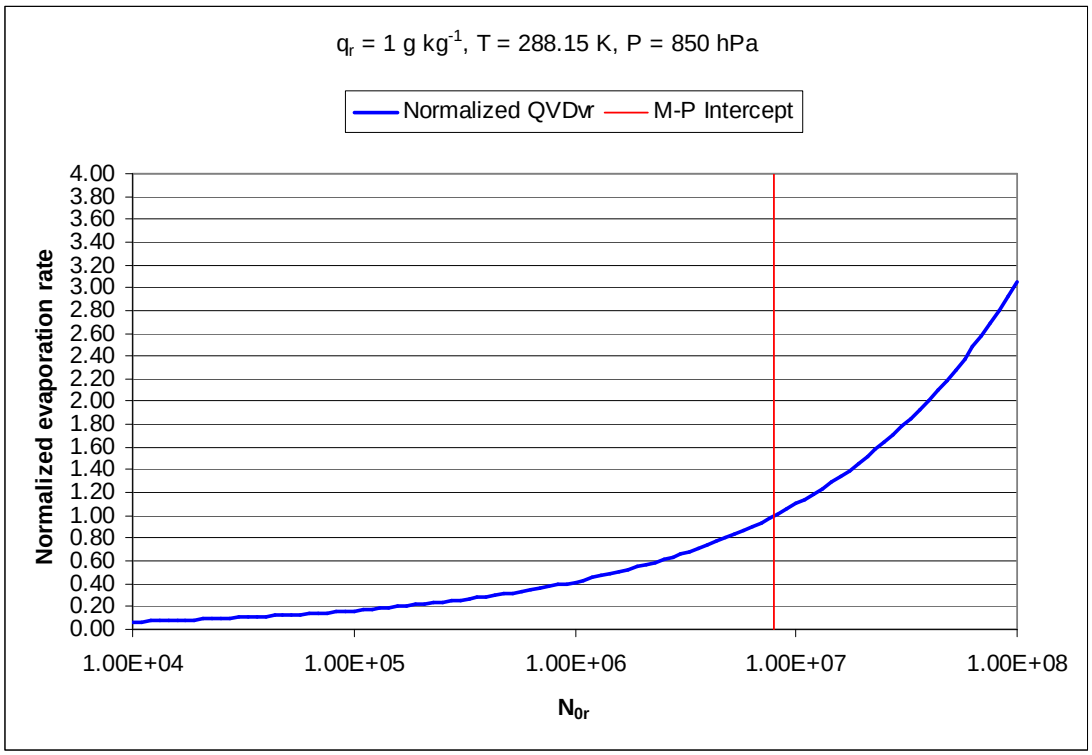

Fig. 2.4. Normalized instantaneous evaporation rates for rain as a function of N_{0r} for the exponential case (α = 0), and a fixed q_r = 1 g kg^{-1}. The values of QVD_{vr} are normalized with respect to that found with the M-P value of N_{0r} = 8.0 x 10^6 m^{-4} (denoted by the vertical red line).

In a DM scheme, in which N_{0r} and λ_r are allowed to vary independently, the shape parameter α in the general gamma distribution case still needs to be specified (or diagnosed). As well, α affects the calculation of the ventilation coefficient (Eqn. 6). It should be noted at this point that the physical meaning of N_0 in Eqn. 2 for nonzero α is different than for the case where α = 0 (i.e. as in the exponential distribution), and, in fact, the units of N_0 for the gamma distribution are dependent on

α as $[L]^{-4-\mu}$, where [L] is a length unit (Ulbrich 1983). With this in mind, to isolate the impact of α on evaporation rates, it makes sense to fix the moment-based quantities N_{tr} and q_r and allow α to vary, for purposes of illustration. To demonstrate this impact, evaporation rates were calculated using Eqn. 5-7 for a fixed q_r = 0.001 kg kg^{-1} and the same thermodynamic conditions as the previous example, and varying values of α, normalized relative to the value of evaporation rate with α = 0 and N_{0r} = 8.0 x 10^6 m^{-4}.

The intercept parameter was initially set at 4 different values for the case of α = 0. The resulting curves (Fig. 2.5) with corresponding fixed values of N_{tr}, are shown in Fig. 2.5. It can be seen that increasing α while holding N_{tr} and q_r fixed serves to increase the evaporation rate. Physically, this is due to the narrowing of the distribution and the simultaneous overall increase of total surface area of the drops in the distribution (Cohen and McCaul 2006), which leads to enhanced evaporation as the number concentration of smaller and mid-sized drops increases (though the number concentration of the smallest drops, i.e., as D approaches 0 also decreases, these drops contain little mass to evaporate). Also clearly seen in Fig. 2.5 is the impact of changing the initial value (i.e. for α = 0) of N_{0r}. As N_{0r} increases (decreases), the evaporation rate increases (decreases). For example, for α = 0, a factor of 12.5 increase in N_{0r} from 8.0 x 10^6 to 1.0 x 10^8 m^{-4} leads to a factor of 3 increase in instantaneous evaporation rate.

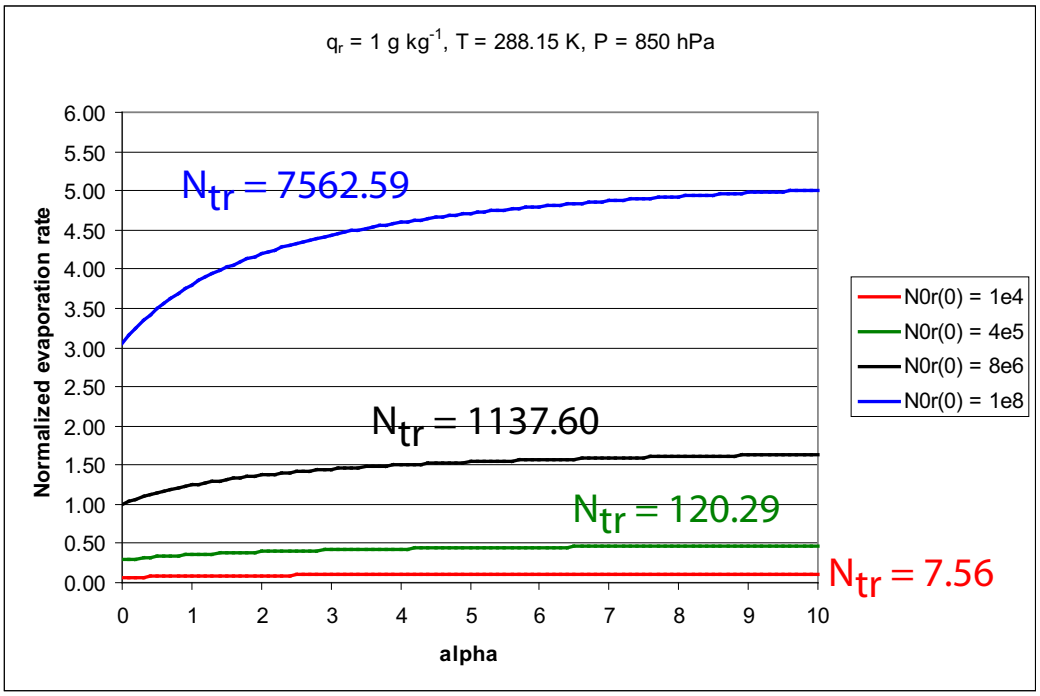

Fig. 2.5. Normalized instantaneous evaporation rates for rain as a function of α for a fixed value of q_r = 1 kg kg^{-1} and the indicated fixed N_{tr}. Initial values of N_{0r} for each curve are shown in the legend (units of m^{-4}).

2.3.3.3 Hail melting and collection of rain by hail

Melting of hail is also treated similarly in the MY05b and LIN schemes. The basic equation for the melting process is given by (MY05b Eq. 53),

$$QML_{xr} = \frac{2\pi}{L_f \rho} N_{0x} \left(K_a T_c - L_v \psi \rho \Delta q_s \right) \mathrm{VENT}_x + \frac{C_w T_c}{L_f} \left(QCL_{cx} + QCL_{rh} \right). \quad (10)$$

(10) is derived by considering the heat and mass balance of a melting hailstone falling at its terminal velocity that may also be collecting liquid water in the form of cloud droplets and rain drops. The calculation of $VENT_h$ in the above equation is similar to that for rain, and the dependence of the first term on the LHS to N_{0h} is similar in form to that for the evaporation of rain, and so the effect of N_{0h} and α is expected to be

similar. The first term on the LHS physically represents the processes of conduction of heat between the surface of the hailstone and the air, and the latent cooling due to evaporation of the melting water in a subsaturated environment (e.g., MY05b, LF0). The second term on the right hand side (RHS) represents the sensible heating by collected cloud and rainwater, and can significantly enhance the melting rates. Both MY05b and LFO parameterize the melting equation in nearly the same way, but differences arise in how the collected cloud and rain water are treated. Also, in both MY05b and LFO, the collection term for rain and cloud water is handled by considering whether the hail is undergoing wet or dry growth (see MY05b and LFO for discussion). In LFO, however, the collection of cloud and rain is a production term for hail only in the case of T < 273 K, and contributes to heating of the ambient air through the release of latent heat of fusion only in this temperature regime. For MY05b, in contrast, no such temperature dependence is applied to QCL_{rh}, both in its effect on increasing the bulk hail mass, and on the latent heating effect applied to the ambient air. Sensitivity tests indicate that this has the effect of partially offsetting the much larger melting rates (and associated ambient cooling) that result due to allowing the hail field to collect and retain rainwater at temperatures above freezing, since, as Eqn. (10) above indicates, the melting rate is directly proportional to the collection rate. Due to this large cancellation of two terms in the thermodynamic equation, the overall effect is similar to that of the LIN scheme.

2.3.3.4 Summary

In summary, in the convective situations studied in this paper, the dominant processes responsible for temperature changes in the downdrafts and associated cold

pools of convective storms are evaporation of cloud and rain, melting of hail, and collection of rain by hail. Both the bulk evaporation of rain and melting of hail are significantly affected by the PSD of each. In particular, in SM schemes that fix N_{0r}, the choice of this parameter significantly affects the bulk evaporation rate. Larger values of N_{0r} will lead to global increases in evaporation rate within a simulation, all other things being equal. The ventilation coefficient provides for enhanced evaporation of falling drops and is of a larger magnitude for distributions biased toward larger drops, and thus serves to partially counteract the dependence of evaporation/melting on increasing N_{0r}. Similar arguments apply to melting of hail, although that process is complicated by the interaction of the hail field with the rain field, much of which may be produced by the melting of the hail itself.

The rate of change of temperature due to these processes can be written as,

$$\frac{\partial T}{\partial t} = \frac{L_v}{c_p}\left(QVD_{vr} + QVD_{vc}\right) + \frac{L_f}{c_p}\left(-QML_{hr} + QCL_{rh}\right), \tag{11}$$

where negative values of QVD_{vr} and QVD_{vc} are associated with cooling, positive values of QML_{hr} are associated with cooling, and positive values of QCL_{rh} are associated with heating. L_v and L_f are the latent heats of vaporization and fusion, respectively, and c_p is the specific heat of dry air at constant pressure. In Chapter 5, the impacts of these processes on the development of simulated supercells of the 3 May 1999 Oklahoma tornado outbreak will be examined through the use of budget and trajectory analyses.

Chapter 3 Overview of the 3 May 1999 Oklahoma Tornado Outbreak

3.1 Introduction

During the afternoon of 3 May 1999, and extending into the overnight hours, one of the most significant tornado outbreaks in U.S. history occurred over parts of Oklahoma and Kansas. The outbreak was characterized by several discrete tornadic supercells that collectively produced over 70 tornadoes in Oklahoma, Kansas, and Texas (NWS website reference). Oklahoma was by far the worst hit of these states, and the remainder of this chapter will focus on the portion of the outbreak in Oklahoma. According to SDS02, 58 tornadoes alone touched down within the county warning area of the Norman, OK National Weather Service (NWS) office, of which 16 were rated F2 or greater on the Fujita scale of tornado intensity (Fujita 1971). Within the Norman, OK NWS county warning area (CWA), eight supercells were responsible for the tornado outbreak, and were given letter identifiers from A-I (omitting F) in chronological order of initiation (SDS02), a convention we will also follow throughout the dissertation. The most intense and deadliest of the tornadoes was rated F5, and heavily damaged the towns of Bridge Creek, Moore, Del City, Midwest City and adjacent areas of Oklahoma City (SDS02), and was responsible for the deaths of 36 people (Brooks and Doswell 2002). After SDS02, we will refer to this tornado as tornado "A9", that is, the ninth tornado documented to have been produced by storm A.

The remainder of this chapter provides a brief overview of the outbreak from a synoptic down to a tornado-scale perspective and sets the stage for the numerical modeling experiments in the following chapters. The layout of this chapter is as

follows: in section 2, a brief description of the synoptic-scale features is presented, and previous observational and numerical studies are summarized. In section 3, storm-scale aspects of the outbreak are discussed, with a particular focus on "storm A", the first storm to develop of the outbreak, and also the one that produced the F5 tornado mentioned previously (SDS02). (A real-data numerical modeling study of this storm and tornado is presented in Chapter 7).

3.2 Synoptic Overview

The upper-level synoptic-scale pattern on 3 May 1999 was dominated by a large negatively-tilted trough centered over the SW U.S. A shortwave trough was embedded in the base of the long-wave trough and progressed from AZ into western OK and KS during the afternoon and evening (Fig. 3.1). This shortwave was accompanied by a mid-to-upper tropospheric jet streak that overspread much of OK and KS during the afternoon hours and contributed to increasing deep-layer shear over this region. By mid to late afternoon, both low-level and deep-layer shear profiles were highly favorable for tornadic supercells over most of western and central OK. In addition, the combination of increasing low-level moisture, with surface dewpoints approaching 20 °C east of a diffuse dryline over SW OK, and deep synoptic-scale ascent resulting in mid-level adiabatic cooling, and modest surface heating underneath a broken cirrus cloud canopy lead to widespread CAPE values on the order of 3000-5000 J kg^{-1} from central OK southward through central TX by mid-afternoon (Thompson and Edwards 2000; Roebber et al. 2002, hereafter TE00 and RSR02, respectively). Feltz and Mecikalski (2002) document the rapid increase of CAPE from values on the order of 2000 J kg^{-1} to 4000-5000 J kg^{-1} from late-morning

to late afternoon, and the rapid decrease in CIN from values on the order of -200 to -300 J kg^{-1} to -50 J kg^{-1} or less from early to late afternoon as retrieved from the Atmospheric Emittance Radiance Interferometer (AERI) sites at Purcell, Lamont, and Vici, OK. The rapid decrease in CIN is particularly striking (see Fig. 6b of Feltz and Mecikalski 2002) and allowed for an atmosphere prime for convective initiation by mid-to-late afternoon over southwest and central OK.

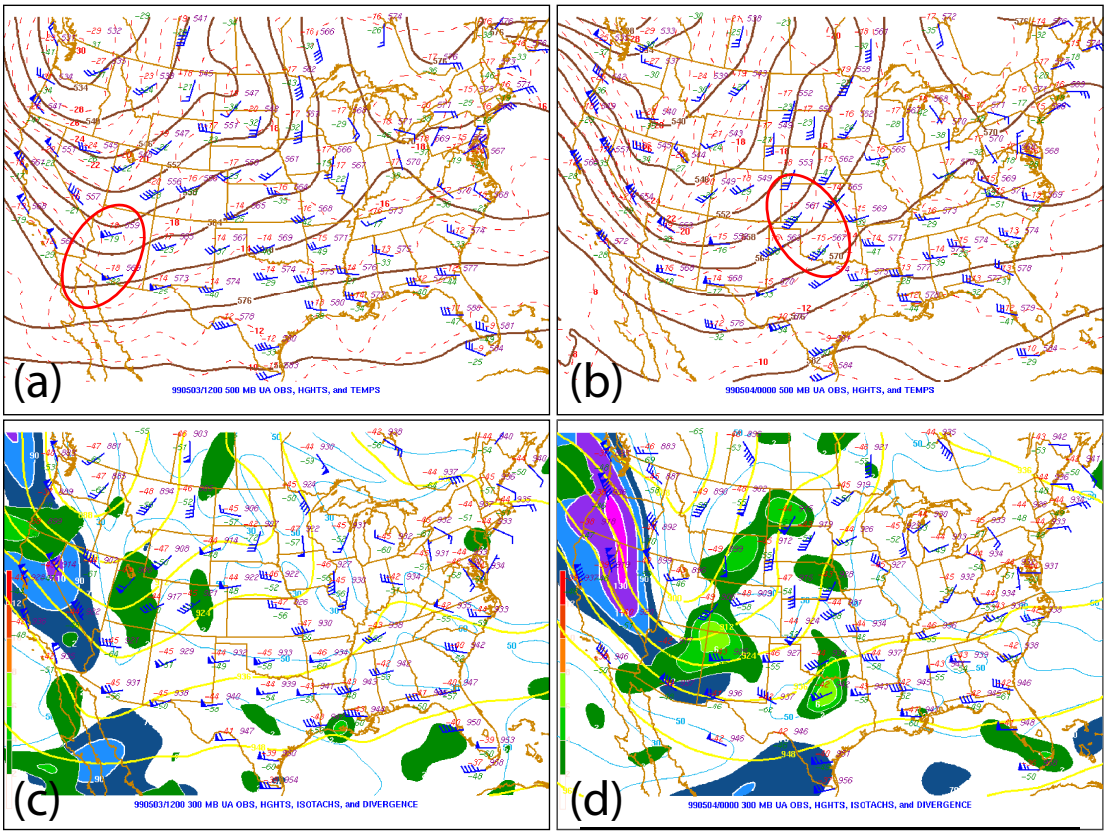

Fig. 3.1. Objectively-analyzed (using the previous 6-h Eta model forecast fields as a first guess) 500 hPa heights (60 dam interval, brown contours), with overlaid RAOB station observations for a) 1200 UTC 3 May 1999, and b) 0000 UTC 4 May 1999. The location of the shortwave trough that played a key role in the tornado outbreak is circled in red in both panels. Also shown are objectively-analyzed 300 hPa heights (120 dam interval, yellow contours), wind speed (blue-to-purple color fill, 20 kt increment, starting at 70 kts), and divergence (increments of 1 x 10^5 s^{-1}, green shading).

As described in RSR02, the mid-to-upper level jet streak was associated with an upper-tropospheric PV anomaly that provided forcing for synoptic-scale vertical ascent as it moved across OK and KS in the afternoon hours, and was visually marked by a broken cirrus canopy. They found in their high-resolution convection-resolving modeling study that 1) the cirrus canopy limited surface heating in the warm sector overall, while holes in the canopy provided regions of locally-enhanced instability, favorable for convective initiation, and 2) the synoptic-scale ascent associated with the PV anomaly that was responsible for the cirrus shield contributed to destabilization by adiabatic cooling of the mid-levels of the atmosphere. Sensitivity tests indicated that the artificial removal of the cirrus canopy from the model fields resulted in widespread convective development and many unfavorable storm interactions that limited the severity of the event by resulting in less long-lived model supercells (RSR02).

3.3 Storm-scale Overview

The outbreak began with the initiation of a single storm in SW OK between 2030-2045 UTC, which, after an initial split, rapidly developed into an intense right-moving supercell (TE00). This first storm of the outbreak (storm A) became tornadic about an hour after its genesis, producing several tornadoes between 2151 and 2321 UTC 3 May, before producing its most intense tornado, the F5 Bridge Creek—Oklahoma City (OKC) —Moore tornado A9, which lasted from 2326 UTC 3 May to 0048 UTC (SDS02). After the dissipation of this tornado in south central OKC, storm A rapidly weakened, but still produced 3 more tornadoes in southern and eastern Oklahoma County before dissipating northeast of OKC around 0100 UTC (SDS02).

Storm B produced its first tornado at 2236 UTC and later went on to produce the long-track F4-rated Mulhall, OK tornado (the 20th and final tornado from this storm), which dissipated at 0345 UTC. During this time, several other supercells rapidly developed and quickly became tornadic, each producing several tornadoes (SDS02). Fig. 3.2 shows an objective analysis of surface equivalent potential temperature (θ_e) at 0000 UTC 4 May 1999, during the early stages of the outbreak. The main storms A and B are indicated. Storm A was producing tornado A9 at the time of this analysis.

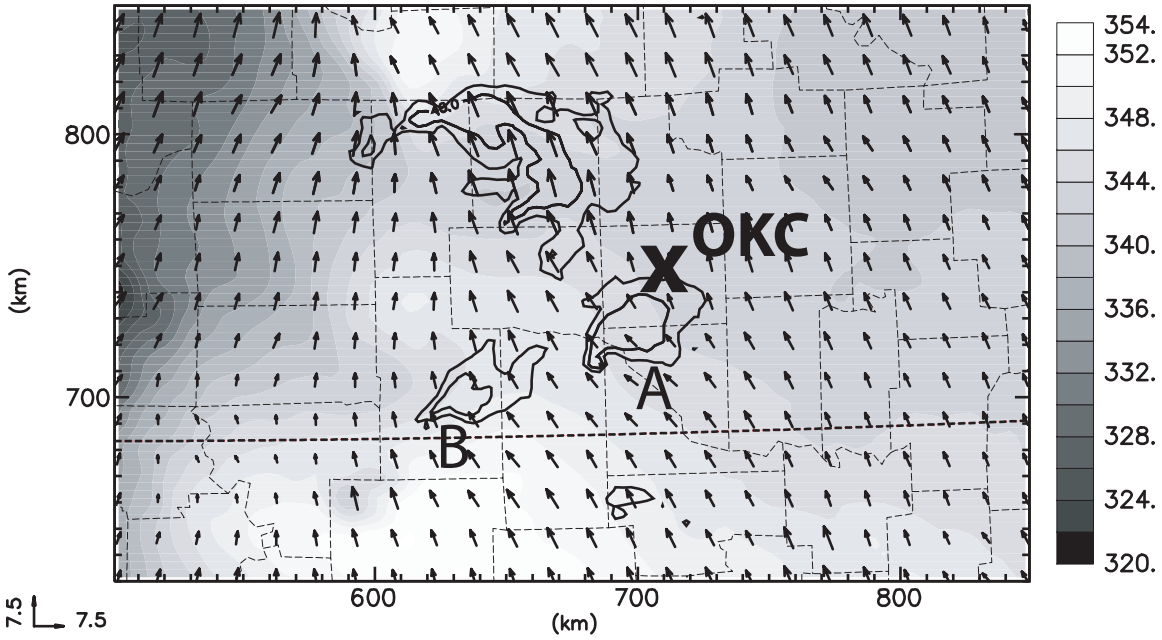

Fig. 3.2. Objective analyses of surface θ_e (grayscale), observed reflectivity (black contours, 20 dbZ increment), and horizontal wind vectors (every 15 km, scale in m s^{-1} indicated in lower left of figure) that include Oklahoma Mesonet data, at 0000 UTC 4 May 1999 centered over central Oklahoma. Oklahoma City is labeled OKC.

Even though the still insufficient observation density of the Oklahoma Mesonet precludes detailed analyses of storm cold pools, it can be seen nevertheless

that large and extensive cold pools are absent in the analysis. In addition M02 indicates that mobile mesonet observations in the hook echo region of storms A and B both indicated small (< 4 K) equivalent potential and virtual potential temperature (θ_e and θ_v) deficits through most of their observing times. These issues are of prime interest in this study and will be discussed in more detail in the following chapters.

Chapter 4 Preliminary Real-data Numerical Simulations of the 3 May 1999 Outbreak

4.1 Introduction and experiment design

In this short chapter, we briefly introduce the real-data simulations which provided an extracted sounding for the idealized simulations. The coarse-resolution (3 km grid spacing) real-data simulations were an initial attempt to produce realistic simulations of the tornado outbreak and to examine the impact of MP schemes on the evolution and interaction of the storms in the outbreak. It was found (Dawson et al. 2007) that, at such a grid resolution, cold pool strength and size were both consistently over-predicted, for each of the MP schemes examined. Thus, to examine the impact of microphysics in more detail, we turned to a systematic set of idealized simulations that use a single sounding to define the environment and do not include radiation or surface physics processes. These idealized experiments are the main focus of Chapter 5. Chapter 6 will address a new set of high-resolution real-data simulations. Because the sounding used by these idealized simulations was extracted from a real-data simulation, we briefly describe the early real-data experiments here. The real-data simulations used a 3-km horizontal grid spacing and were run with full physics, including surface and radiation physics and a 1.5 order TKE-based subgrid-scale turbulence closure (Xue et al. 2001). The grid dimensions were 1440×1440×20 km^3 (see Fig. 4.1). Vertical grid stretching was employed using 53 vertical levels starting with 20 m grid spacing at the low levels. Initial analysis background and the lateral boundary conditions came from the North American Regional Reanalysis (NARR, Mesinger et al. 2006) at 3 hour intervals. Fifteen-minute intermittent assimilation cycles were performed over a 1 hour period from 2100 to 2200 UTC, 3

May 1999, wherein radar data (reflectivity only) from the Oklahoma City WSR-88D radar (KTLX) were assimilated via the ADAS (ARPS Data Analysis System, Brewster 1996; Zhang et al. 1998; Brewster 2002; Hu et al. 2006) cloud analysis scheme at 15 min intervals. This captured some of the early stages of development of the two initial supercell thunderstorms, labeled A and B in Fig. 3.2, that formed in the afternoon. Storm A started to spawn tornadoes at 2141 UTC (1641 CDT). The ADAS analyses at 2100 and 2200 UTC also included conventional surface and upper air data plus the Oklahoma Mesonet data. A forecast was then launched from the 2200 UTC analysis and ran for 7 h. We tested a total of five MP schemes or their variations. They include two variations of the Lin scheme where N_{0r} was set to the default Marshal-Palmer value of 8.0 x 10^6 m^{-4} (LINA) or to a reduced value of 4.0 x 10^5 m^{-4} (LINB). The other three forecasts used the SM, DM and TM versions of MY scheme, respectively (Table 4.1). All forecasts are otherwise identical. The experiment naming convention throughout the chapter and the rest of the dissertation will follow the template *[dx][scheme]*, where *[dx]* denotes the horizontal grid spacing and *[scheme]* denotes the MP scheme/configuration as given in Table 4.1. For example, experiment *3kmMY2* has a 3-km grid spacing and uses the MY2 scheme. Table 4.2 indicates the values of the intercept parameter for each of the precipitating categories for each of the SM schemes, where applicable. The parameters in Table 4.2 also apply to the idealized simulations, to be discussed in Chapter 5.

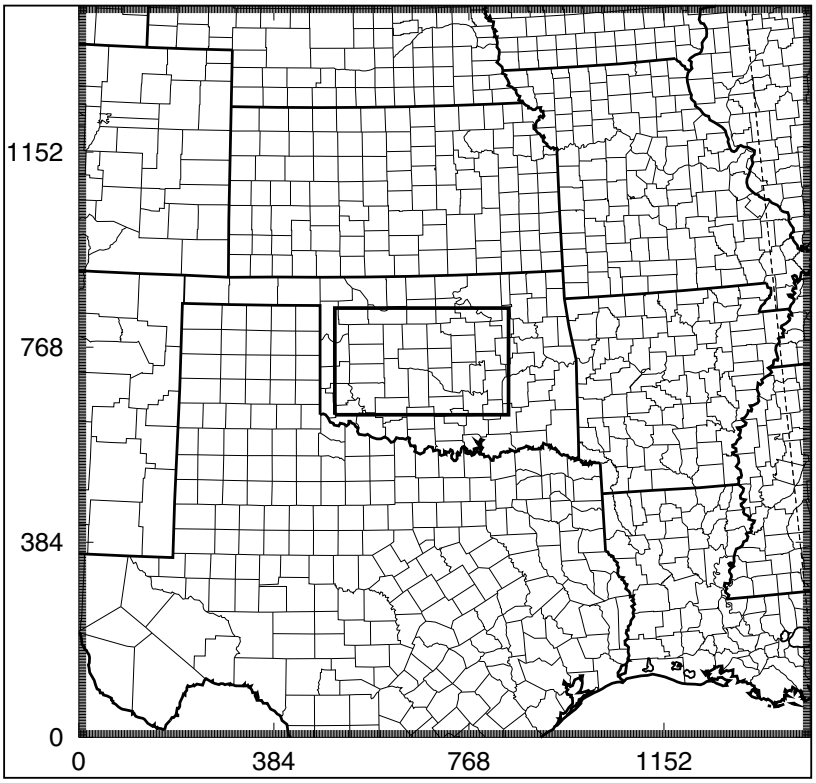

Fig. 4.1. The 3 km model domain. The location of the subdomain shown in Fig. 4.2 is indicated by the bold rectangle.

Table 4.1. List of 3 km real data experiments using different microphysics schemes or variations.

Microphysics scheme/configuration	**Description**
LINA	Based on Lin et al. (1983) and Tao and Simpson (1993)
LINB	LIN scheme with N_{0r} reduced from default value of 8.0×10^6 m^{-4} to 4.0×10^5 m^{-4}
MY1	Single-moment version of the MY scheme (q predicted)
MY2	Double-moment version of the MY scheme (q and N_t predicted)
MY2DA	As in MY2 but with diagnostic relations for α
MY3	Triple-moment version of the MY scheme (q, N_t and Z predicted)

Table 4.2. Intercept parameter values for precipitating categories used in the experiments with single-moment microphysics schemes. Here, MD stands for a monodisperse distribution, and $f(T)$ refers to the temperature-dependent N_0 used for cloud ice (see MY05b).

Scheme	***LINA***	***LINB***	***MY1***
N_{0r} ($\times 10^6$ m^{-4})	8.0	0.4	8.0
N_{0i} ($\times 10^6$ m^{-4})	MD	MD	f(T)
N_{0s}($\times 10^6$ m^{-4})	3.0	3.0	3.0
N_{0g}($\times 10^6$ m^{-4})	NA	NA	0.4
N_{0h}($\times 10^6$ m^{-4})	0.04	0.04	0.04

4.2 Results

Figure 4.2 shows surface θ_e and reflectivity for each of the five real-data simulations at 2 h, valid at 0000 UTC 4 May, together with the corresponding ADAS analysis. Compared with the analysis, all simulations over-predict cold pool strength and area coverage, and this is particularly true in terms of moisture (not shown). However, significant differences exist among the simulations, with *3kmLINB* showing the weakest and smallest cold pools, and *3kmMY1* showing the strongest. *3kmMY2* and *3kmMY3* have the most realistic reflectivity structure and intensity overall, particularly in the hook echo and forward flank regions, although the size of the forward flank regions is somewhat over-predicted. Vertical cross-sections (not shown) through the simulated storm downdrafts indicate that in all cases, the dry,

low-θ_e air in the cold pools comes primarily from the mid-troposphere and is brought downward by the large downdrafts.

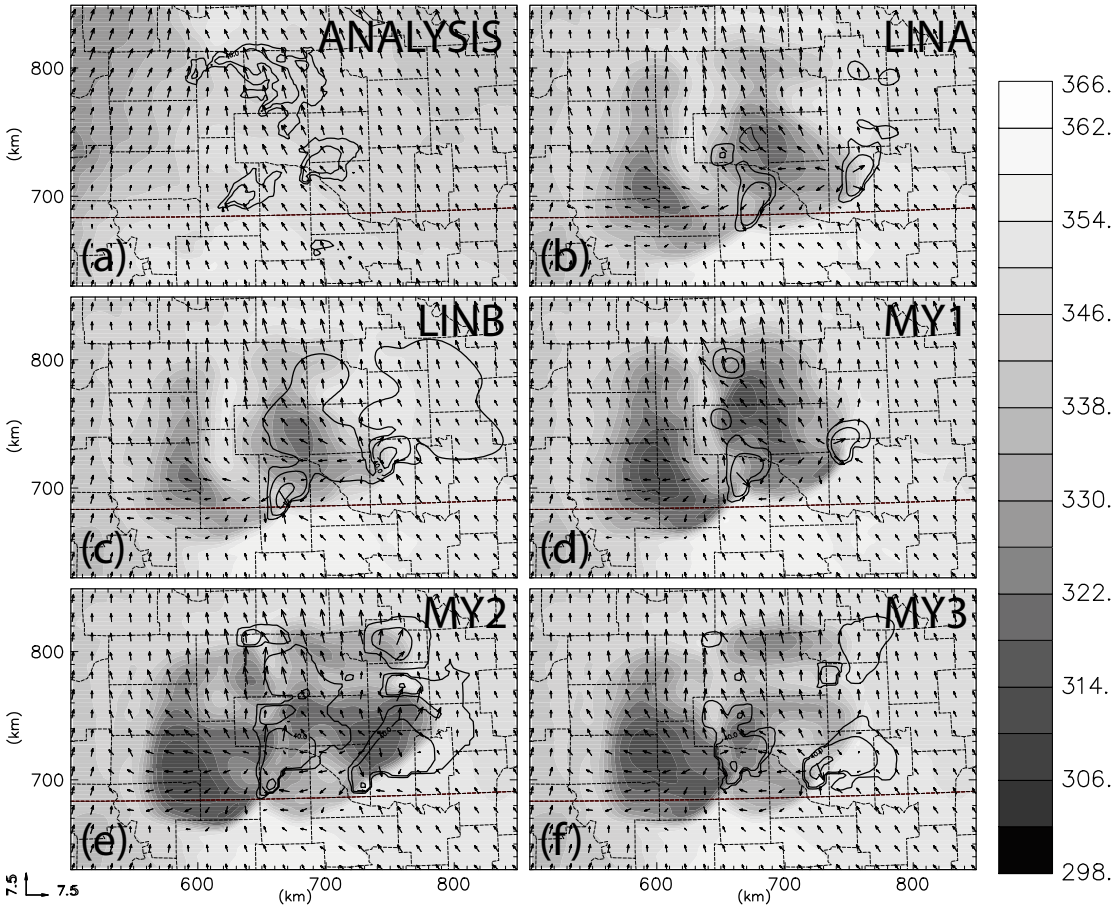

Fig. 4.2. Surface equivalent potential temperature (shaded), reflectivity (contours, 20 dbZ intervals), and wind vectors (plotted every 5 grid points) for a) 0000Z ADAS analysis with overlaid base reflectivity from KTLX radar, b) 3kmLINA, c) 3kmLINB, d) 3kmMY1, e) 3kmMY2, and f) 3kmMY3 runs. All fields are from the 2-h forecast valid 0000 UTC for each run, initialized at 2200 UTC. Only a portion of the full 3-km domain centered over central OK is shown.

The fact that even the multi-moment MP schemes produce overly intense cold pools leads us to suspect that other factors, such as the relatively coarse resolution, might have played a role. For example, at 3-km resolution, the downdraft size may be exaggerated and the resolution does not allow for adequate turbulence activity that

can cause significant mixing between downdraft air and its surroundings. For this reason, we seek to perform more experiments at much higher resolutions. To have more flexibility with the experiments that focus on the examination of the effects of resolution as well as MP schemes, we turn in the following chapter to simpler idealized experiments that utilize a single sounding to define the environment. Chapter 6 will return to the real data case with a complete set of experiments at sufficiently high resolutions.

Chapter 5 Idealized Storm-scale Numerical Simulations of 3 May 1999 Outbreak

5.1 Introduction

In this chapter, we report on high-resolution (3-km or smaller horizontal grid spacing) real-data and idealized simulations of supercell storms in the 3 May 1999 Oklahoma City tornado outbreak, with an emphasis on comparing idealized simulations using MM-MP with those using SM-MP with different values of the rain intercept parameter N_{0r}. Since other studies have examined the sensitivity of simulated supercell storms to parameters in a SM scheme, we will instead focus on the results obtained with the MM schemes and the advantages and disadvantages over using the more common SM approach. Specifically, we show that certain important advantages that MM schemes have over their SM counterparts with regard to their treatment of evaporation and melting effects on the predicted DSDs of rain and hail help to control the cold bias seen in many simulated convective storm downdrafts and associated cold pools. A budget analysis of the thermodynamically-active microphysical processes (primarily melting/freezing, evaporation/condensation, and collection between liquid and ice categories) and an examination of trajectories within the low-level downdrafts will be performed.

Two BMP schemes are examined, one based on the popular Lin et al. (1983) ice MP scheme, with modifications by Tao and Simpson (1993). This scheme, hereafter referred to as LIN, is the default ice MP scheme in the Advanced Regional Prediction System (ARPS, Xue et al. 2000; 2003), the numerical model used in this investigation. The LIN scheme is a SM 3-class ice scheme that predicts the mixing ratios of cloud water, rain water, ice crystals, snow aggregates, and graupel/hail (q_c,

q_r, q_i, q_s, q_g, q_h, respectively), while holding the intercept parameter for each precipitating species -- rain, snow, and graupel/hail -- fixed. The cloud and ice species are assumed to have negligible terminal velocities and are described as monodispersed.

The other BMP used is the MM-MY scheme described in MY05a,b. As discussed in Chapter 2, the MY scheme has recently been incorporated into the ARPS model. The scheme predicts up to three moments of the DSD for each of the five classes of precipitating hydrometeors (rain, ice crystals, snow, graupel, and hail), and two moments for cloud water, which is assumed to have negligible terminal velocity. The cloud water DSD is specified as a gamma distribution with two specified shape parameters (MY05b). Note that the MY scheme contains separate categories for graupel and hail, in contrast to the LIN scheme which combines hail and graupel into a single category. The three predicted moments in MY are $M_x(0)$, $M_x(3)$, and $M_x(6)$, proportional to the total number concentration N_{tx}, the mixing ratio q_x, and the radar reflectivity factor Z_x, respectively. With the full triple-moment (TM) formulation, all three parameters in the gamma distribution in (2) vary independently, while for the DM and SM versions, one or both of these parameters must be fixed or diagnosed, as in the case of the diagnostic-α version of the DM scheme. Throughout this chapter, we will refer to this scheme with the abbreviations MY1, MY2, MY2DA, and MY3 to signify the number of moments predicted. Here MY2DA refers to the diagnostic-α scheme, as described in MY05a,b. For further details on these schemes, see the discussion in Chapter 2.

This chapter is organized as follows. Section 5.2 describes the methodology of the idealized experiments, section 5.3 discusses the results of the 500-m grid-spacing experiments, including budget and trajectory analyses. Section 5.4 discusses the 250 m grid-spacing experiments. Further discussion of the results and broader implications are found in section 5.5, and section 5.6 summarizes the chapter and discusses ongoing and future work.

5.2 Experiment design

Idealized experiments allow us to focus on the effects of the MP schemes and allow for a large set of experiments at high resolutions before retuning to more realistic settings. Bryan et al. (2003) suggests that resolutions much higher than 1 km may be necessary to properly resolve convection. We conduct a series of simulations at 1 km, 500 m, and 250 m horizontal grid-spacings, and included 4^{th}-order computational mixing whose coefficients are 0.0005, 0.0015, and 0.002 s^{-1}, respectively, for the three resolutions. The vertical grid setup is the same as the real-data experiments discussed in Chapter 4.

The same MP configurations as in the real-data simulations in Chapter 4 were used, namely, LINA, LINB, MY1, MY2, and MY3. The MY2 scheme with diagnostic α (MY2DA) was also tested. The sounding used was extracted from the 1-h forecast (valid at 2300 UTC) of *3kmLINA* at a location that was determined in reference to the Oklahoma surface Mesonet observations to be more representative of the unstable inflow region of the storms during the early stages of their tornado-producing phase. The observed Norman, Oklahoma (OUN) sounding at 0000 UTC 4

May 1999 is believed to represent more of the environment after the storms reached maturity.

This extracted sounding has a similar wind profile to the observed OUN sounding, but the temperature and moisture profiles are significantly different (see Fig. 5.1). Figure 5.2 shows the vertical profile of θ_e for the OUN and extracted soundings. The vertical gradient in θ_e above the boundary layer is similar in both soundings, as is the minimum value, but the height of the minimum θ_e is higher in the extracted sounding. The θ_e values in the boundary layer differ significantly, indicating higher temperatures and moisture content in the extracted sounding. As the observed storms matured and moved further east and north toward the Oklahoma City area, they encountered slightly lower surface temperatures and dewpoint temperatures, corresponding to an increased cap and lower low-level θ_e as seen on the observed sounding. The large CAPE difference between the two soundings is due to the cooler surface temperatures in the observed sounding as well as the fact that the observed sounding was truncated in the upper levels so that a full CAPE calculation is not possible. With the strong cap and the absence of any mesoscale or synoptic scale forcing in the idealized simulations, the observed sounding was found to be unable to sustain storms in the model. This is another reason that we chose to use the extracted sounding.

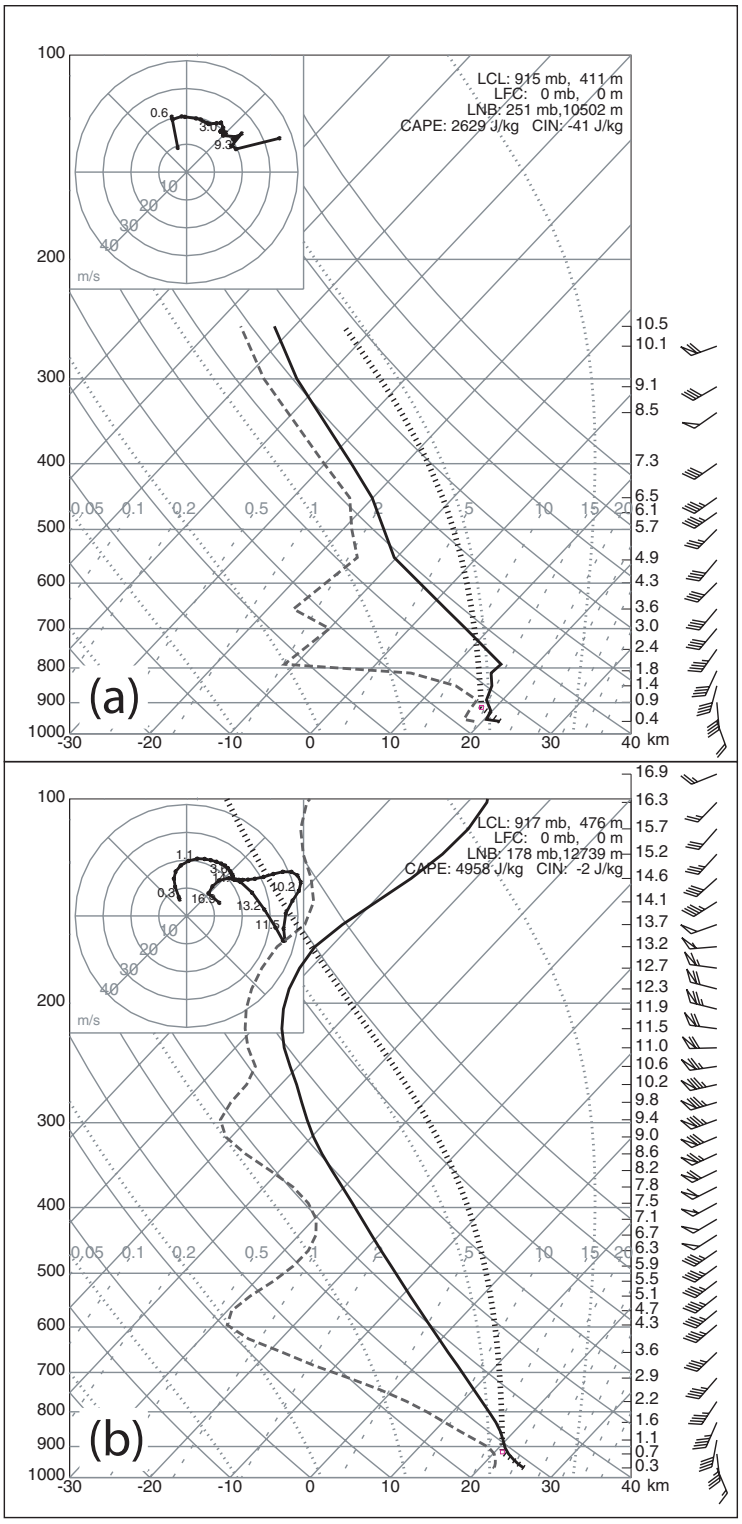

Fig. 5.1. (a) Observed OUN sounding at 0000 UTC 4 May 1999, and (b) model extracted sounding at 2300 UTC (1-hr forecast) from the 3-km LINA experiment in the inflow region of the simulated supercell storms.

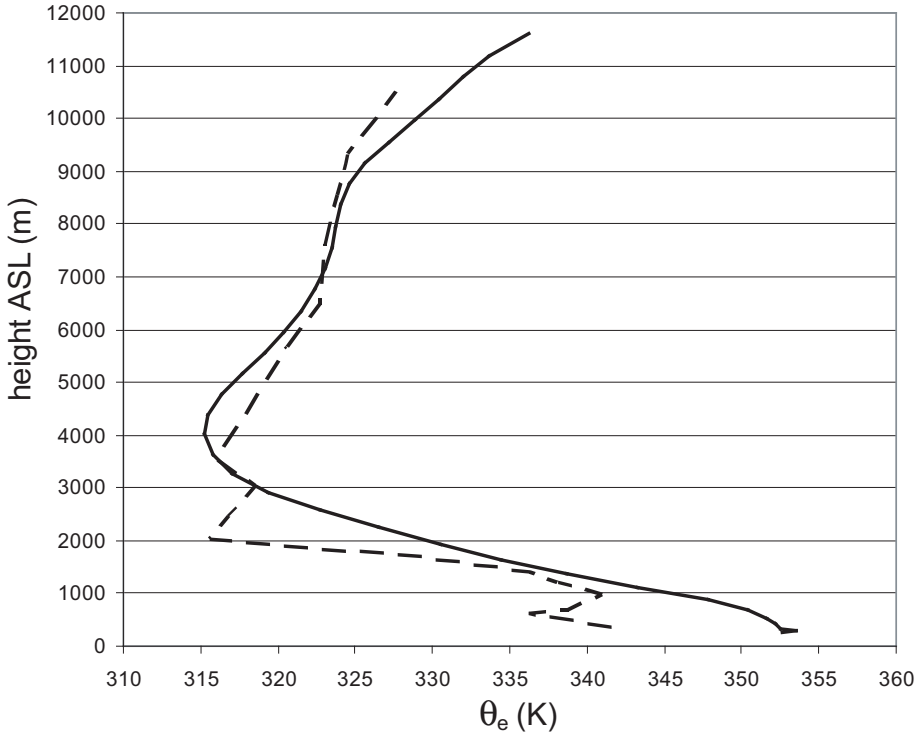

Fig. 5.2. Vertical profile of θ_e for the extracted (solid), and observed 0000 UTC Norman (OUN, dashed) soundings.

For both the 1-km and 500-m simulations, a grid of 128x175x20 km^3 was used. Convection was initiated with an ellipsoidal thermal bubble of maximum potential temperature perturbation of 4 K with a horizontal radius of 10 km and vertical radius of 1.5 km, centered 1.5 km above ground, and 35 and 25 km from the west and south edge of the domain, respectively. The simulations were run out to 2 h. For the 250-m simulations, a smaller 64x64x20 km^3 grid was used, and the initial thermal bubble has the same dimensions and location relative to the southern and western boundaries. In addition, for the 250-m simulations only, the environmental sounding was modified to remove the mean storm motion to keep the storm within the smaller domain. Finally, the 250-m simulations were performed only for the MY

suite of MP schemes. The idealized simulations did not contain radiation forcing or surface fluxes. While the absence of surface friction may affect the cold pool propagation somewhat, its inclusion tends to modify the environmental wind profile over time, which is undesirable for the purposes of these simulations.

5.3 500-m simulations

5.3.1 Cold pool structure

Even with the extracted forecast sounding, the initial storm in the single sounding experiments at 1 km horizontal resolution decayed in less than 1 h; a sustained storm could not be maintained. Within this initial period, LINA and MY1 exhibited more rapid cold pool development than the MY2 and MY3 schemes (not shown). At 500 m resolution, most experiments produced a storm that lasted through most of the 2-h simulation (Fig. 5.3). Compared to the 3-km real-data experiments, the differences in cold pool strength between the SM and MM runs at these higher resolutions are greater, as can be seen from the 1-h surface temperature, dewpoint, and θ_e perturbation fields, plotted in Figs. 5.4, 5.5, and 5.6, respectively. The cold pool structures in the DM and TM runs are similar and are much smaller and weaker than those in the SM cases of *500mLINA and 500mMY1*. The SM runs (*500mLINA*, *500mLINB*, and *500mMY1*) also vary significantly amongst themselves in terms of the cold pool strength and size, with *500mLINB* having the weakest (in terms of θ_e) and smallest cold pool, consistent with the reduced N_{0r} value used. *500mLINB* is overall similar in cold pool size and strength to the MM runs. These results are also consistent with previous studies on the impact of varying N_{0r}, or N_{0h} (Gilmore et al.

2004; Snook and Xue 2006; 2008), or alternatively D_{nh} (van den Heever and Cotton 2004).

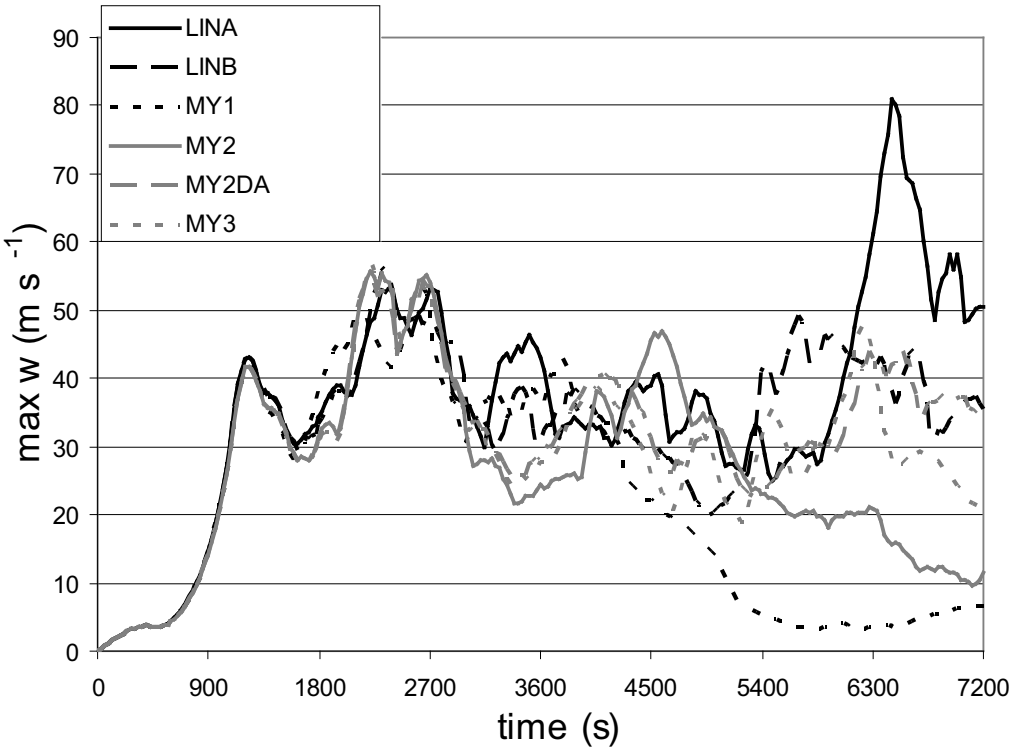

Fig. 5.3. Domain-maximum vertical velocity vs. time for the 500-m simulations.

Interestingly, the supercell storms in the SM runs, with the exception of *500mLINB* are generally characterized by a prominent cold pool in the forward-flank downdraft (FFD) region at the surface, whereas the DM and TM schemes produce a much weaker or even non-existent cold pool in that region, a region where the FFD is defined in the classic supercell conceptual model (see, e.g., Doswell and Burgess 1993). This latter result compares favorably with available surface mesonet observations in the forward flanks of the two most prominent supercells on 3 May 1999 (Fig. 5.7); the observations show temperature deficits of at most 2 – 3 K and dewpoint temperatures that actually increase slightly. This is consistent with the

slightly-subsaturated boundary layer inflow air at the lower levels being driven toward its wet-bulb temperature by evaporation of falling rain. The MM simulations appear to reproduce these conditions in the forward flank, while the SM *500mLINA* and *500mMY1* simulations have temperature and dewpoint deficits consistent with drier, lower-θ_e air from higher levels reaching the surface in the downdrafts.

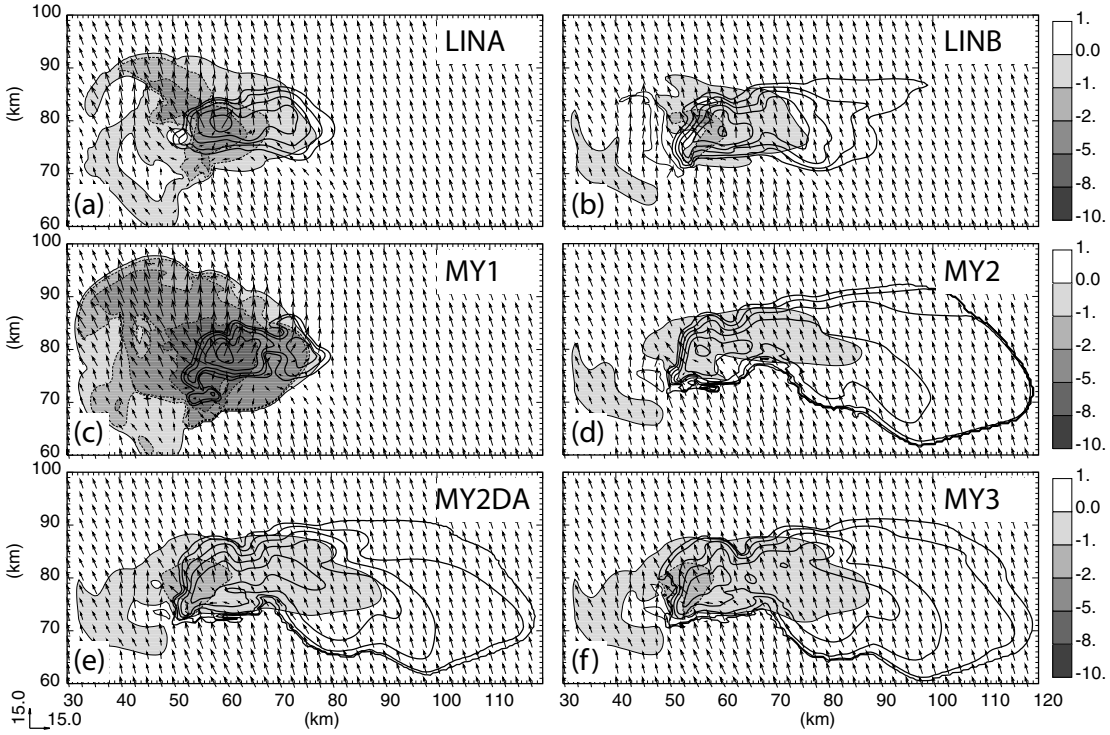

Fig. 5.4. Surface temperature perturbation (grayscale filled contours), reflectivity (heavy contours, 10 dbZ increment), and horizontal wind vectors (plotted every 2.5 km, 1 step = 15 m s^{-1}) for the 500-m simulations at 3600 s: a) 500mLINA, b) 500mLINB, c) 500mMY1, d) 500mMY2, e) 500mMY2DA, and f) 500mMY3. Vectors in this and all subsequent figures, unless otherwise noted, are ground-relative.

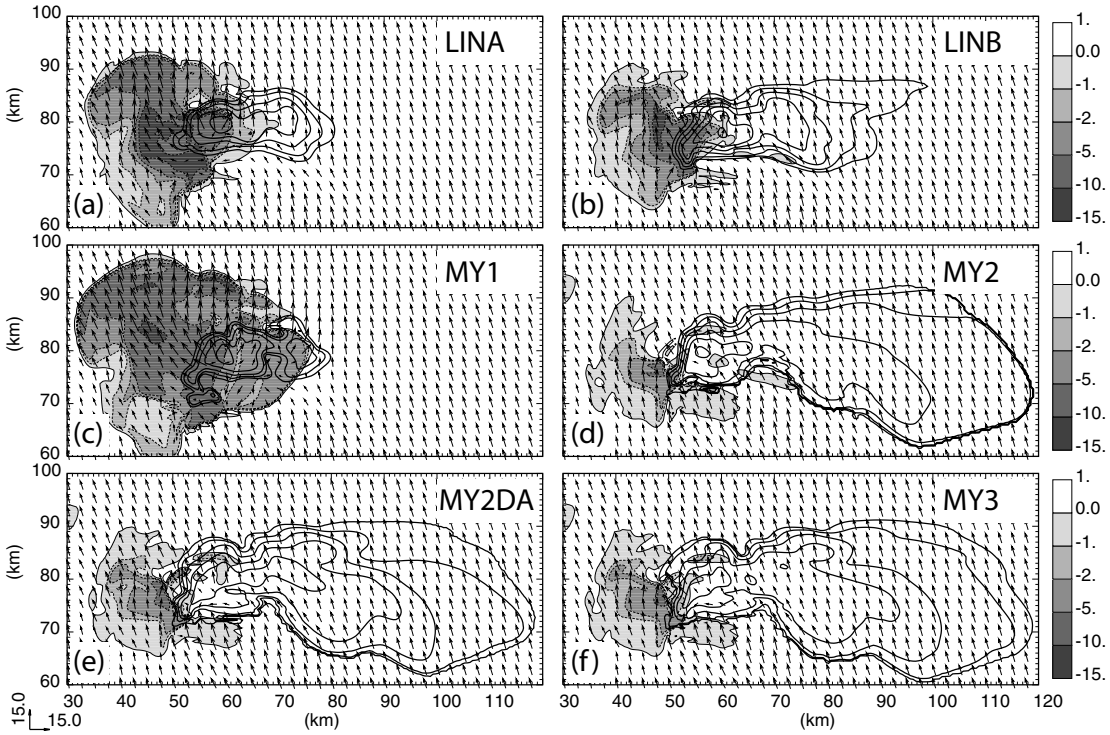

Fig. 5.5. As in Fig. 5.4 except for surface dewpoint temperature perturbation.

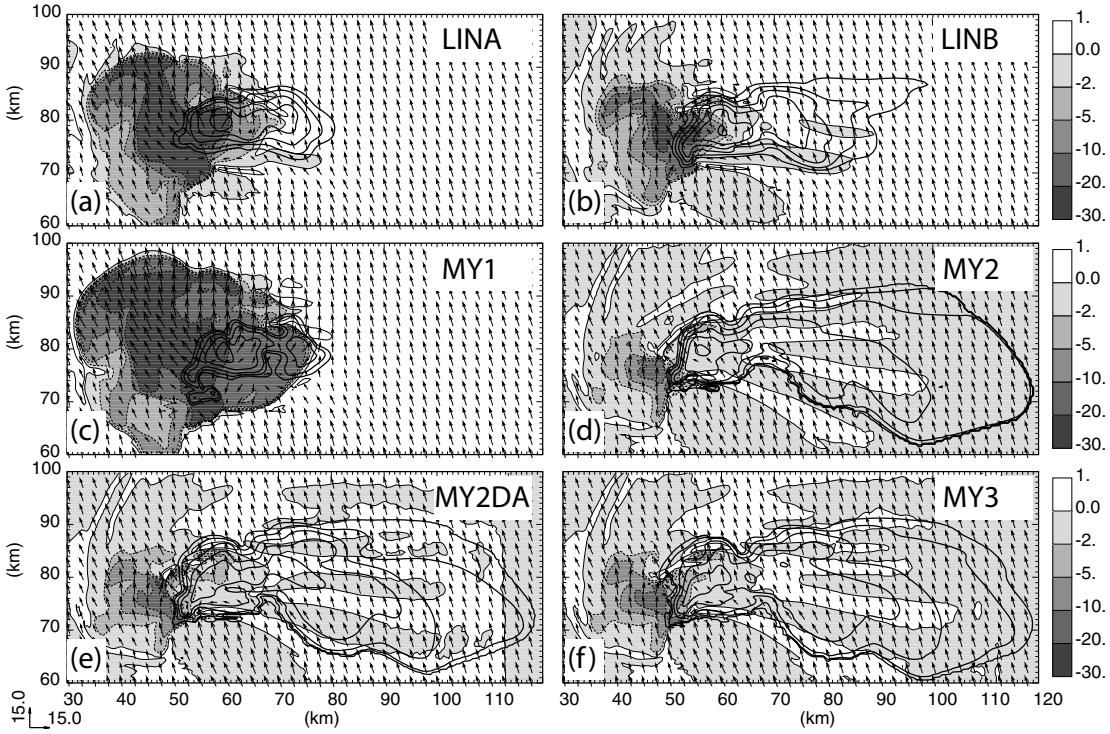

Fig. 5.6. As in Fig. 5.4 except for surface equivalent potential temperature perturbation.

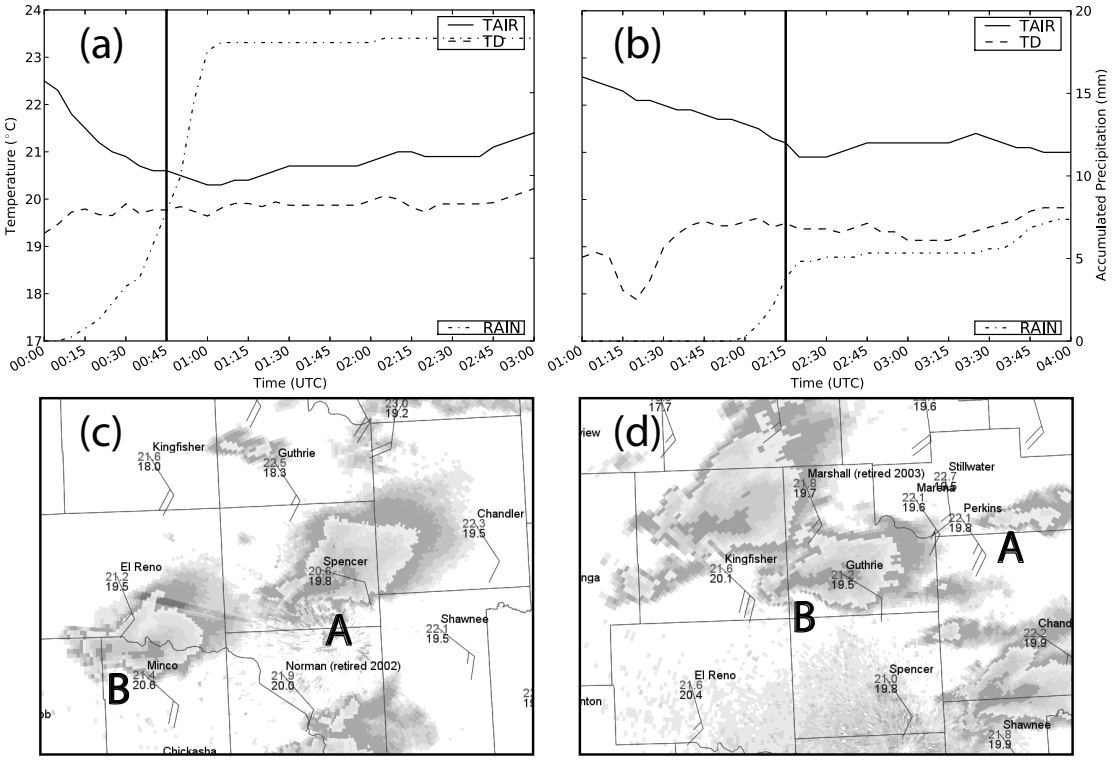

Fig. 5.7. a) Time series from 7:00 p.m. CDT 3 May 1999 (0000 UTC 4 May 1999) to 10:00 p.m. CDT 3 May 1999 (0300 UTC 4 May 1999) for the Spencer mesonet station during the passage of the forward flank Temperature and dewpoint traces (°C) are solid and dashed lines, respectively, and the accumulated precipitation (mm) is a dot-dash line. The thick vertical black bar marks the time of the image in panel (c). b) Similar to (a) but for the Guthrie mesonet station from 8:00 p.m. CDT (0100 UTC) to 11:00 p.m. CDT (0400 UTC). Corresponding base reflectivity (0.5° tilt) images from the KTLX radar and surrounding mesonet station observations (temperature in gray, dewpoint in black, and wind barbs, with full barb equal to 5 m s^{-1}, and half barb 2.5 m s^{-1}) are in panels c) and d). Also labeled in panels c) and d) are the main supercell storms A and B.

5.3.2 Reflectivity structure

In terms of the reflectivity structure in the forward flank region, those in the DM and TM simulations also compare better to the observations in both shape and orientation (compare Fig. 5.7c,d with Fig. 5.4). In addition, the spatial east-west gradient of the reflectivity field in the forward flank is more realistic with the MY2DA and MY3 schemes than with MY2. This is believed to be related to the

excessive hydrometeor size-sorting associated with the MY2 scheme when $\alpha_x = 0$, as discussed by MY05a. To confirm this, we repeated experiment *500mMY2* in which the size-sorting process was turned off by setting the fall speed for total number concentration N_{tx} equal to that of mixing ratio q_x for all categories; in this case, a smaller forward flank region with a weaker reflectivity gradient was obtained (not shown).

5.3.3 Spatial structure of selected microphysical fields

To better determine the main microphysical processes responsible for cooling in the downdraft regions, instantaneous rates of all processes that contribute to either heating or cooling in each MP scheme are analyzed. As will be discussed in the budget analysis section, it is found that melting of hail and evaporation of rain are the most significant contributors to cooling in the downdraft regions, which is consistent with a previous numerical study of microburst-producing storms by Straka and Anderson (1993). Figure 5.9 shows the rain water mixing ratio (q_r), instantaneous evaporation rate, and negative vertical velocity w contours (downdrafts) at 500 m AGL and 1 h of the 500-m simulations. Figure 5.10 shows the same fields but through the vertical cross-sections indicated in Fig. 5.8. Figures 5.11 and 5.12 are similar, but show the corresponding fields for hail, with hail melting rate shown in the place of rain evaporation rate and horizontal cross sections are at 1.5 km AGL. It can be seen that significant differences exist between the instantaneous rates associated with different MP schemes, and in particular between those of SM and MM schemes.

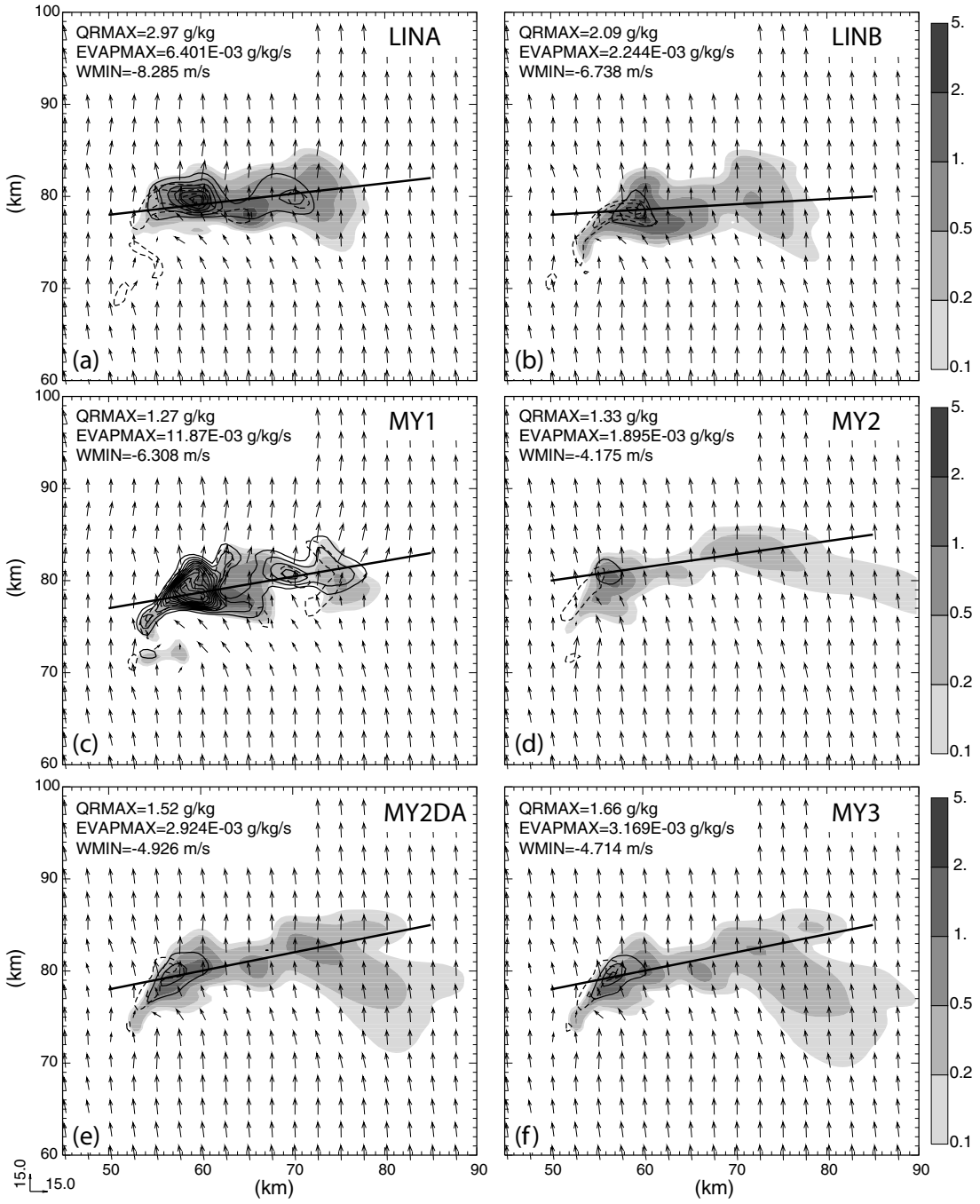

Fig. 5.8. Rain mixing ratio (grayscale filled contours, g kg^{-1}), instantaneous evaporation rate (black contours, 1.0×10^{-3} g kg^{-1} s^{-1} increment), negative vertical velocity (dashed contours, 2 m s^{-1} increment, starting at -2 m s^{-1}) and wind vectors at 500 m AGL at 1 hr for a) 500mLINA, b) 500mLINB, c) 500mMY1, d) 500mMY2, e) 500mMY2DA, f) 500mMY3. Maximum values of q_r and rain evaporation rate and minimum values of vertical velocity are indicated for each panel. Also shown are the locations of the vertical cross sections shown in Fig. 5.9.

The SM schemes show larger magnitudes and greater vertical depths in both evaporation and melting rates, and overall stronger downdrafts as compared to the DM or TM schemes, except that *500mLINB* shows the smallest rain evaporation rates. The hail melting rates of the SM schemes, however, have similar vertical structures, both having significant melting reaching all the way to the surface. In contrast, the MM schemes all show elevated regions of hail melting, with little of it found below 500 m AGL. In addition, the SM schemes tend to produce pronounced FFDs that reach the surface, whereas the MM schemes feature *elevated* FFDs, FFDs that do not reach the ground. Romine et al. (2008) found similar results in their study of the 8 May 2003 Moore, OK supercell, but attributed it at least partially to the relatively weak FFD being unable to penetrate the capping inversion present in the environment of the storm. In the present study, however, no capping inversion is present, and thus it appears that the differences are mainly related to the different MP schemes used. Instantaneous fields at other times indicate similar structure (not shown).

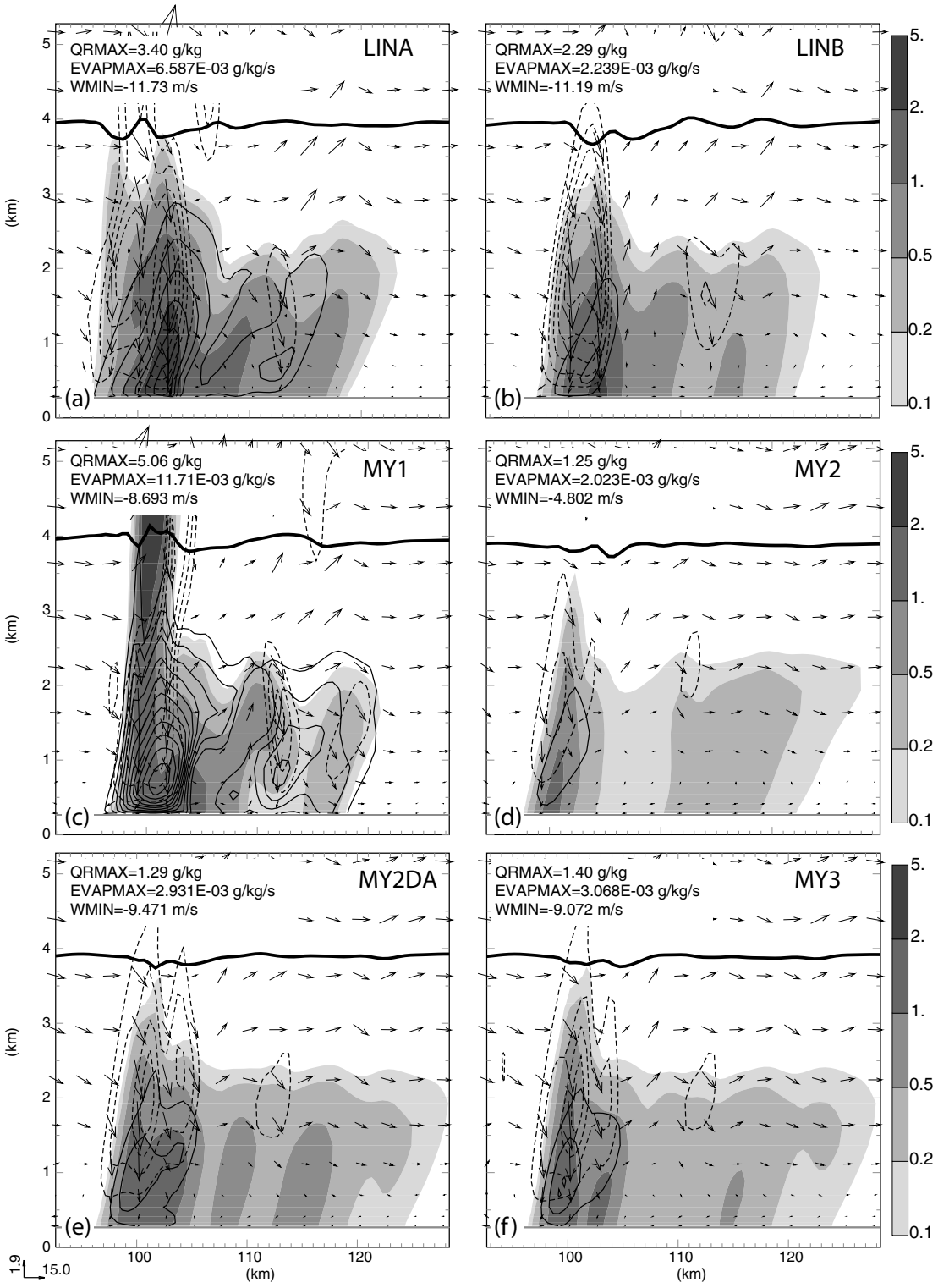

Fig. 5.9. As in Fig. 5.8 but for the vertical cross sections depicted in Fig. 5.8. The 0°C isotherm is also shown in thick black lines.

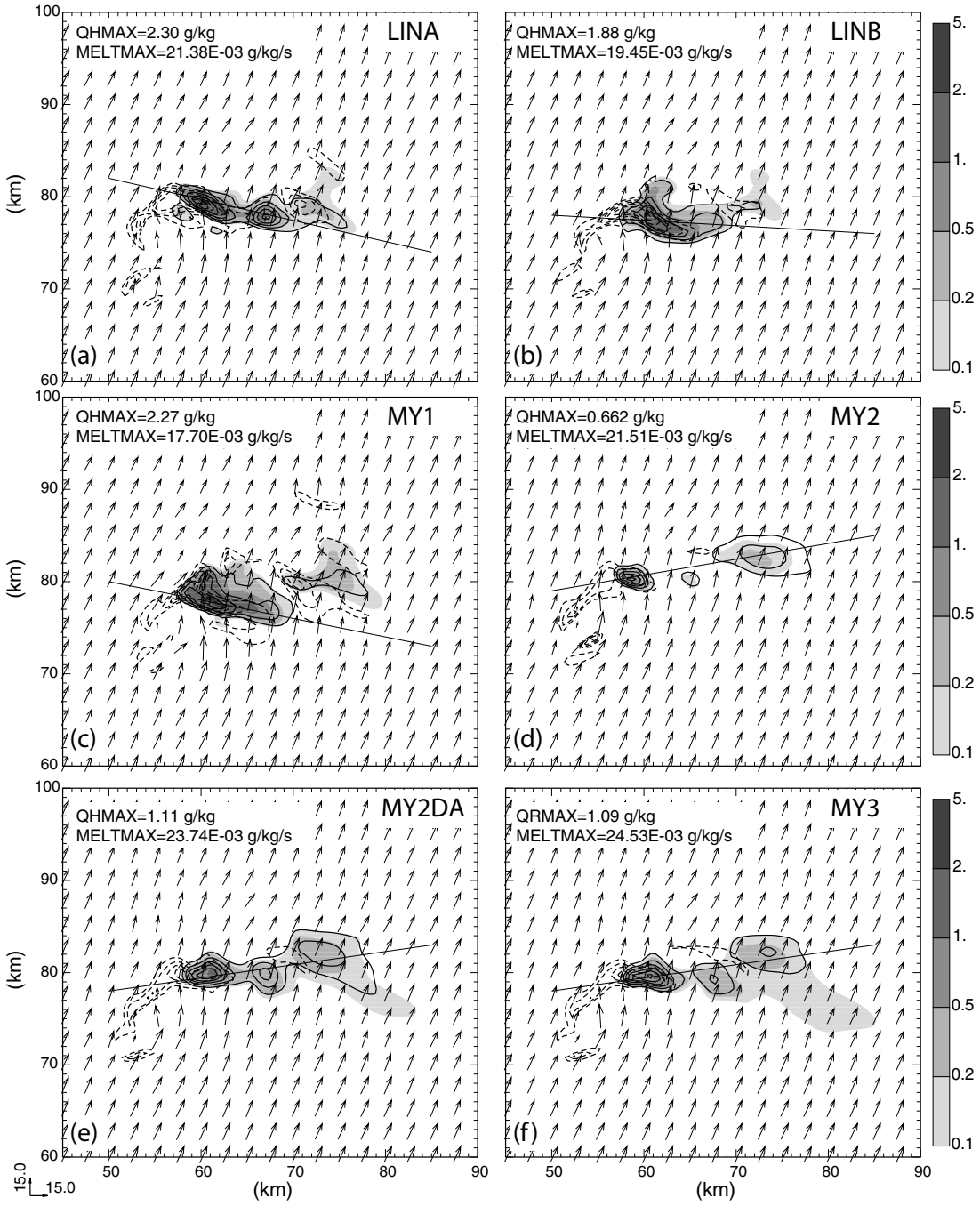

Fig. 5.10. As in Fig. 5.8 but for hail mixing ratio (grayscale filled contours, g kg^{-1}), and instantaneous melting rate (black contours, 4.0×10^{-3} g kg^{-1} s^{-1} increment) at 1.5 km AGL. Locations of the vertical cross-sections in Fig. 5.11 are also shown.

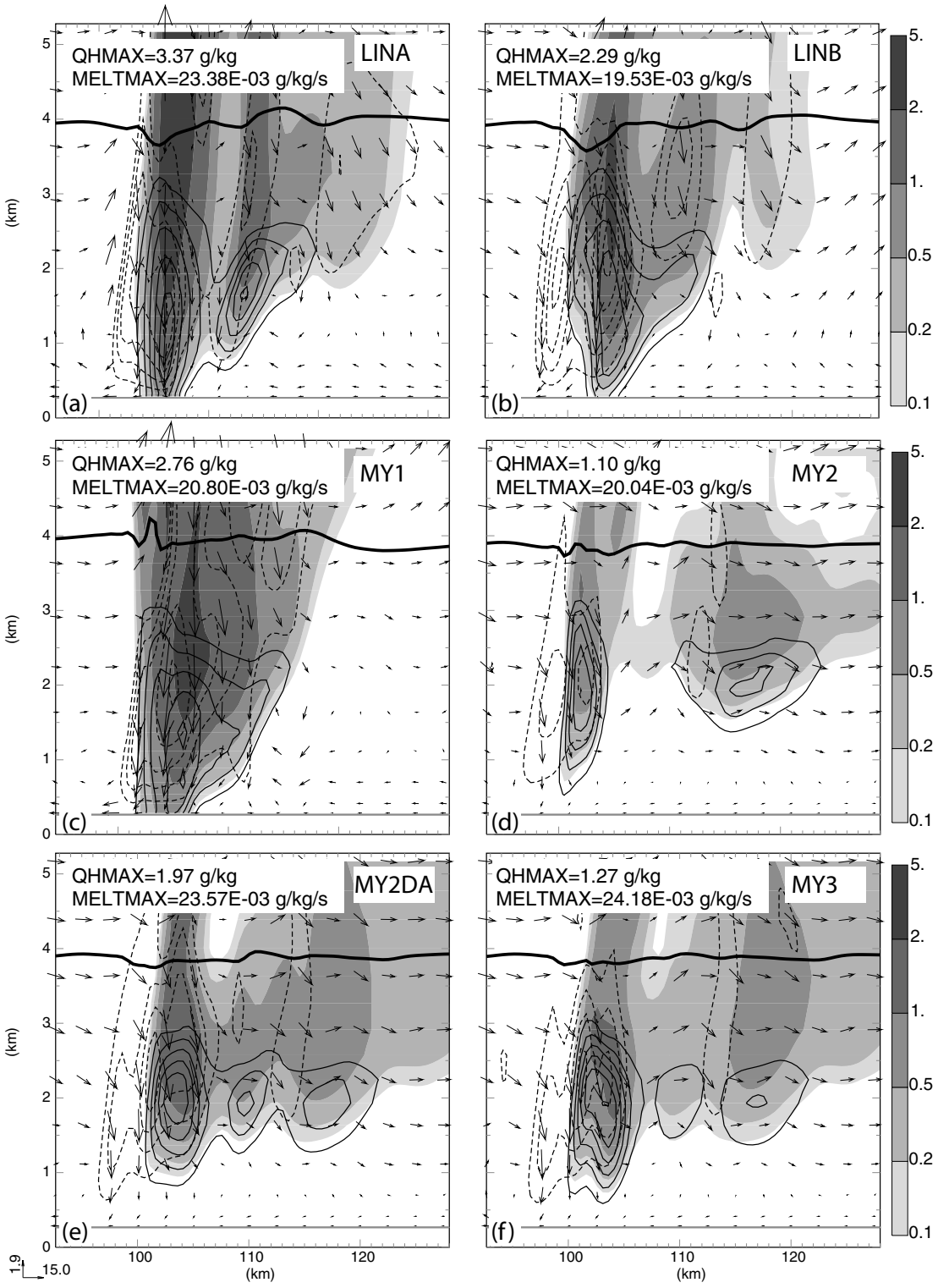

Fig. 5.11. As in Fig. 5.10 but for the vertical cross-sections depicted in Fig. 5.10. The 0°C isotherm is also shown (bold black line).

5.3.4 Budget analysis

A greater understanding of the differences in the roles of the various microphysical processes within the low-level downdraft in different simulations can be obtained by performing detailed budget analyses of the microphysical source terms related to temperature change. At any point, the time rate of change of temperature due to phase changes of water can be written as

$$\left.\frac{\partial T}{\partial t}\right|_{mp} = S_{mp}, \tag{12}$$

where the subscript *mp* denotes microphysical phase changes, and S_{mp} includes all source and sink terms involving phase changes of water. The processes include evaporation and condensation of cloud water; evaporation of rain; melting and freezing of ice crystals, snow, graupel, and hail; and collection (freezing) of cloud and rain by each of the above ice categories. Most of the processes are common to the schemes examined in this study. However, since the LIN scheme does not contain a separate graupel category, the associated processes are not active. In addition, neither the LIN nor MY scheme allows for condensation of vapor onto rain.

To determine the most important processes and how they differ among the simulations, the instantaneous rates of these processes were output at 30 s intervals for each of the simulations for two 30-min intervals: 1800-3600 s, and 3600-5400 s. Total cooling/heating is calculated for each of the processes by integrating the thermal energy change within each grid cell that is below 4 km AGL and has vertical velocity less than – 0.5 m s^{-1} (defined as the downdraft region) and over each of the 30 minute period using a 30-s time step, i.e., $\Delta E_{mp} = \sum_{i,j,k,t} (\rho C_p \Delta T_{mp} \Delta x \Delta y \Delta z)$, where ρ

is air density and Δx, Δy and Δz are the local grid spacing in *x*, *y* and *z* directions, respectively.

The bulk heating/cooling budgets for the processes are shown in Fig. 5.12 for the 500-m simulations, in units of gigajoules (GJ). In general, the MM simulations are very similar in magnitude of total cooling, while the SM simulations differ from each other and from the MM simulations. The difference in total downdraft cooling between *500mLINA* and *500mLINB* is significant and directly attributable to the smaller fixed N_{0r} value used, which has a first-order effect on decreasing the rain evaporation rate. Of all the runs, *500mMY1* has the greatest magnitude of cooling, including that due to evaporation of rain. Even though the same intercept parameters were used in *500mMY1* and *500mLINA* for all precipitating species, other differences in the schemes, such as in the treatment of the cloud category and the fall speed relation for the rain category are possible reasons for the differences in total cooling. The reason for the large differences between the MM runs (collectively) and the SM runs is less clear, since N_{0x} is allowed to vary in time and space for a given species *x*. Vertical profiles of horizontally and time-averaged values (using the same criteria as in the budget analysis for the downdraft region) of mixing ratio, number concentration, mean-mass diameter, and shape parameter for rain (Fig. 5.13) and hail (Fig. 5.14) were computed for the 500-m runs. Only grid points with non-zero hydrometeor content were included in the averaging. These plots suggest that two main differences between the MM and SM runs contribute to the smaller magnitudes of cooling in the low-level downdrafts in the MM cases: 1) the generally smaller mass contents of rain and hail in the downdraft, and 2) the overall larger mean-mass

diameters of the particles in the MM runs. Indeed, average number concentrations of rain are 1-2 orders of magnitude smaller in the MM runs than in the SM runs, while the mixing ratios are only a factor of 2 or less lower through most of the depth of the low-level downdrafts. This is reflected in the D_{mr} profiles (Fig. 5.13c), which indicate significantly larger average raindrop diameters in the MM runs over most of the depth of the low-level downdraft. For hail, all simulations show a tendency for the mixing ratio to decrease towards the surface, with the SM runs maintaining significantly higher mixing ratios through most of the depth, particularly in the low levels, where they are approximately a factor of 10 larger than the MM runs. Below about 1 km, the average number concentration of hail in the MM runs decreases rapidly, along with the mixing ratio, which reflects the loss of the small end of the spectrum of hail to melting, while the fewer, larger hailstones survive by virtue of their increased fall speed. In the SM runs, in contrast, the number concentration of hail remains relatively high, being monotonically-related to the mixing ratio. Size-sorting in the MM schemes is at least partially responsible for the differences. The larger mixing ratios and number concentrations of both rain and hail in the low-levels leads to greater cooling by evaporation and melting in the SM runs over the MM runs.

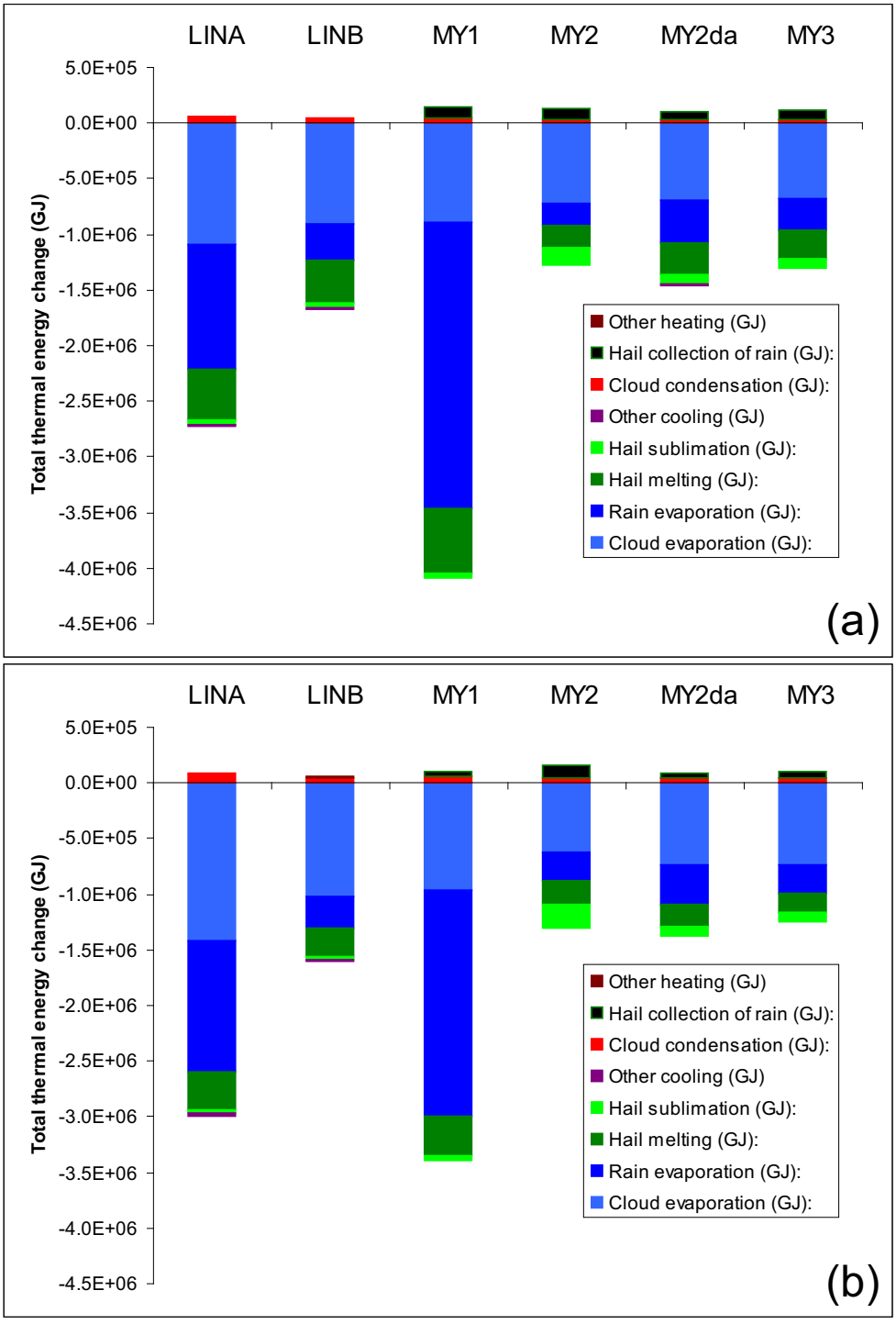

Fig. 5.12. Bulk thermal energy change ($c_p \Delta T$) from microphysical processes in the low-level downdraft (defined as all grid boxes below 4 km AGL with $w < 0.5$ m s^{-1}) between a) 1800 s and 3600 s and b) 3600 s and 5400s for each of the 500-m simulations.

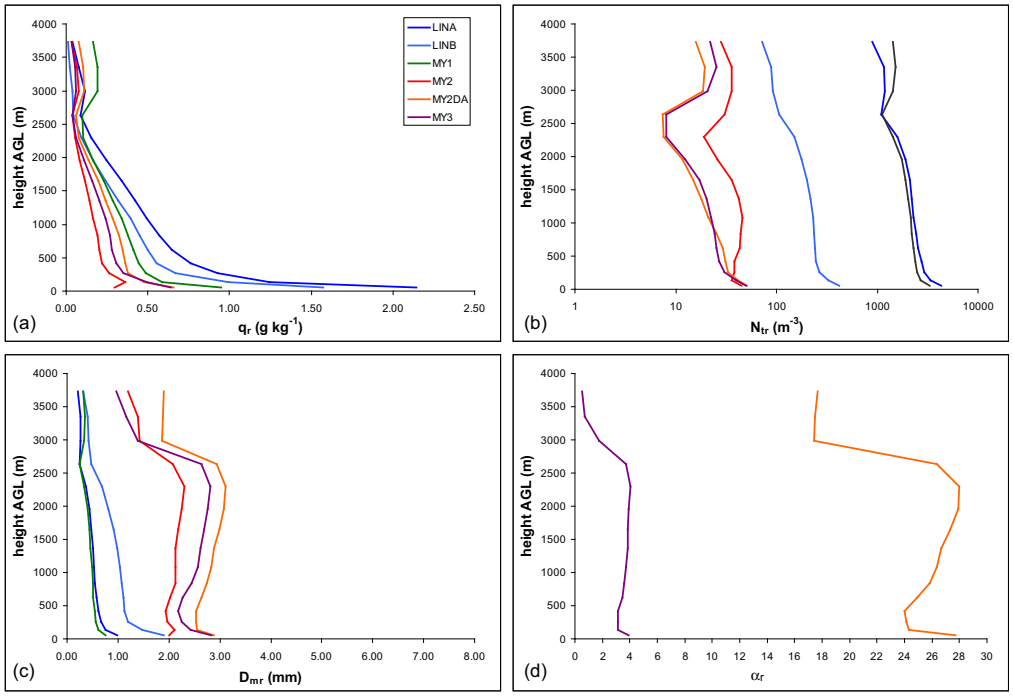

Fig. 5.13. Vertical profiles of horizontally and time-averaged rain DSD parameters in the low-level downdrafts of the 500-m simulations: a) mixing ratio q_r, b) total number concentration N_{tr}, c) mean-mass diameter D_{mr}, and d) shape parameter α_r.

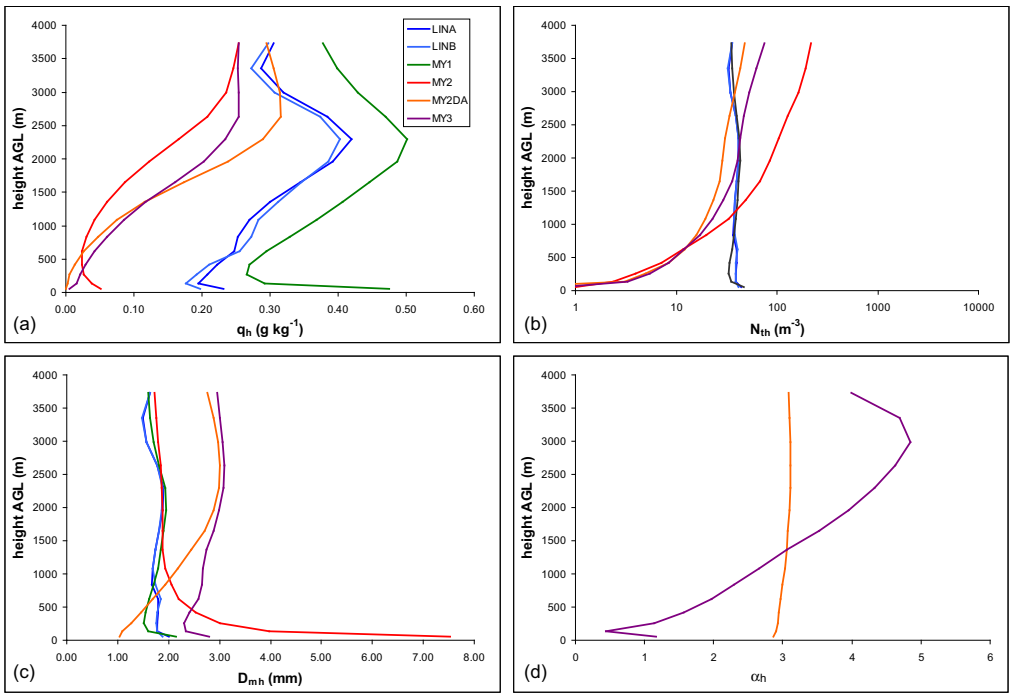

Fig. 5.14. As in Fig. 5.13 but for hail.

5.3.5 Trajectory analysis.

To investigate the source of the air that contributes to the development of the surface cold pool within these simulations, trajectory analyses are performed. We examine trajectories terminating just above the surface in the cold pool. We examine groups of 9 trajectories that terminate near the minimum θ_e at the surface near the reflectivity core after 45 min of simulation time for each run (see Fig. 5.15). The relatively early time is chosen to minimize nonlinear differences in the development of the broad features of each storm, when comparing the trajectories. For each group of trajectories, averaging is performed across each of the trajectories at a given point in time, for each time, to yield a single "ensemble average" trajectory. For a parcel that is undergoing saturated pseudoadiabatic or unsaturated adiabatic descent and does not mix with its environment, θ_e is conserved. The approach to the trajectory analysis we use here is similar to that of Gilmore and Wicker (1998), although they examined θ_w, which is conserved under the same conditions as θ_e used here. For this study, we use the definition of θ_e found in Bolton (1980). In principle, assuming conservation of θ_e, the source level of the air entering the surface cold pool via the convective downdrafts can be determined by comparing with the vertical profile of θ_e in the environmental sounding.

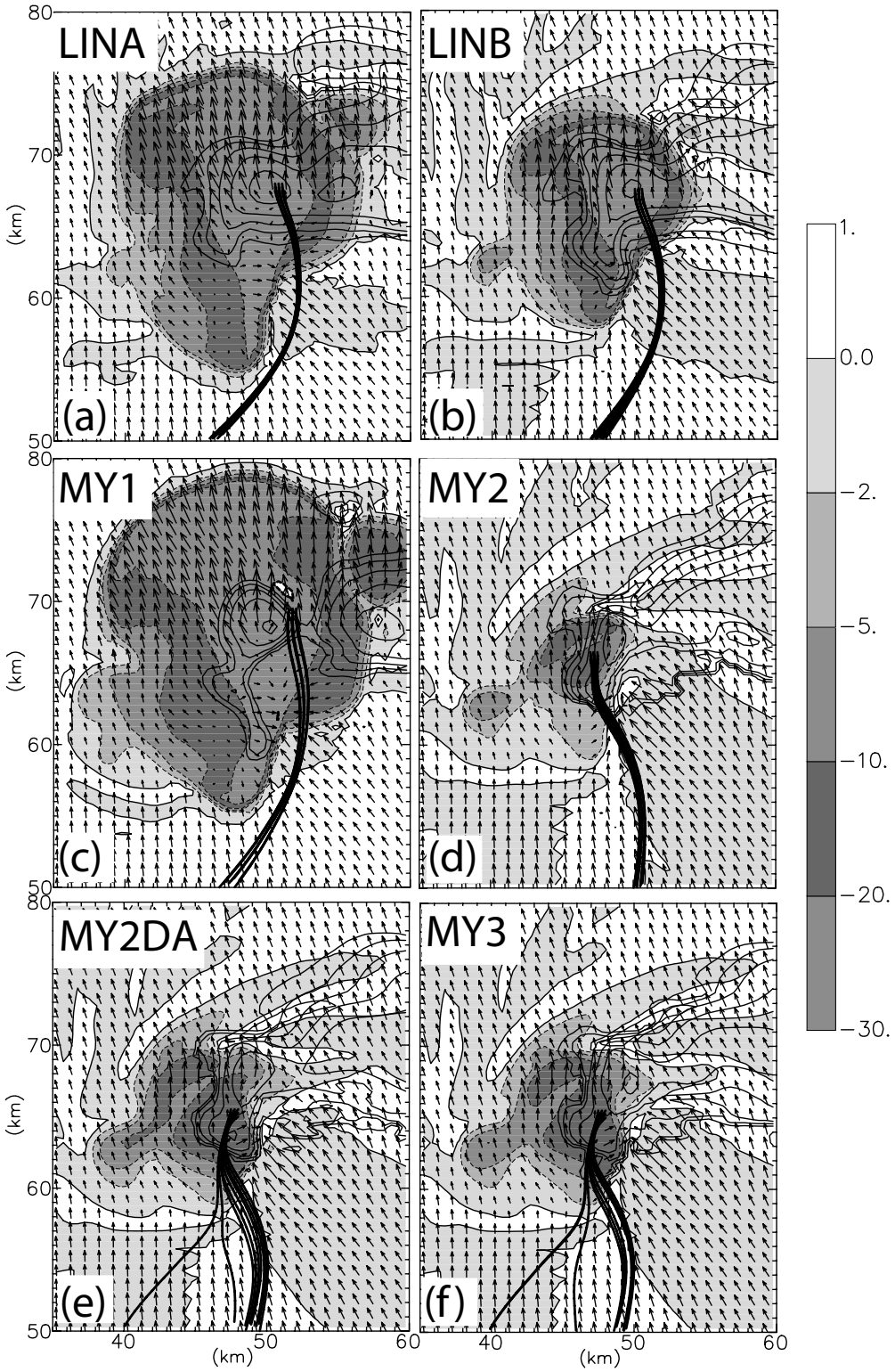

Fig. 5.15. Surface θ_e' (grayscale), reflectivity (black contours, 10 dBZ increment), wind vectors every 1 km (1 unit = 7.5 m s-1), and trajectories terminating in and near region of minimum θ_e' near the precipitation core at 45 min for a) 500mLINA, b) 500mLINB, c) 500mMY1, d) 500mMY2, e) 500mMY2DA, f) 500mMY3.

By examining trajectories in this manner, it becomes possible to determine the relative importance of melting and evaporation within the downdrafts that reach the surface for the different MP schemes, while simultaneously testing the hypothesis that cold pools with lower θ_e are formed from air that has descended from mid-levels, where the lowest values of θ_e are found. Figure 5.17 shows the average height vs. time for the trajectory group terminating near the minimum surface θ_e for each of the simulations. It can be seen that the trajectories in the SM runs tend to come from higher up, roughly between 2 and 3 km AGL, above the boundary layer, within the region of low θ_e (c.f. Fig. 5.2), while those in the MM runs all originate lower down, at about 1 km AGL, within or near the top of the boundary layer. This is true even though θ_e is not actually conserved along the trajectories. Diabatic processes such as turbulent mixing and melting of hail can both lead to non-conservation of θ_e. Examination of θ_e along the trajectories in each run (not shown) indicates a general trend of decreasing θ_e by several degrees, likely due to both of the aforementioned processes. Thus, θ_e is still useful as a qualitative proxy for initial parcel height.

Figure 5.18 shows time series of instantaneous MP process rates (trajectory ensemble average). The SM runs all (except for rain evaporation in LINB) show significantly greater magnitudes of evaporation of rain and melting of hail than the MM runs. For example, the peak average cooling rates along the ensemble trajectory for rain evaporation are 16.3, 6.0, and 33.7 J kg^{-1} s^{-1} for LINA, LINB, and MY1, respectively, while they are 4.0, 7.7, and 6.9 J kg^{-1} s^{-1} for MY2, MY2DA, and MY3, respectively.

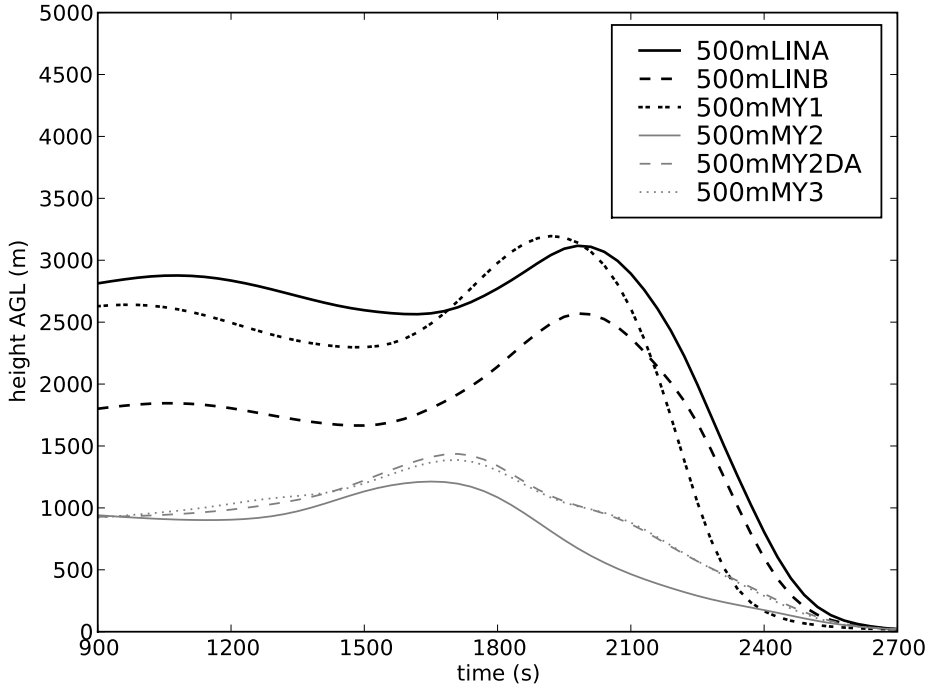

Fig. 5.16. Average height vs. time for each of the trajectory groups shown in Fig. 5.15 for each of the 500 m runs.

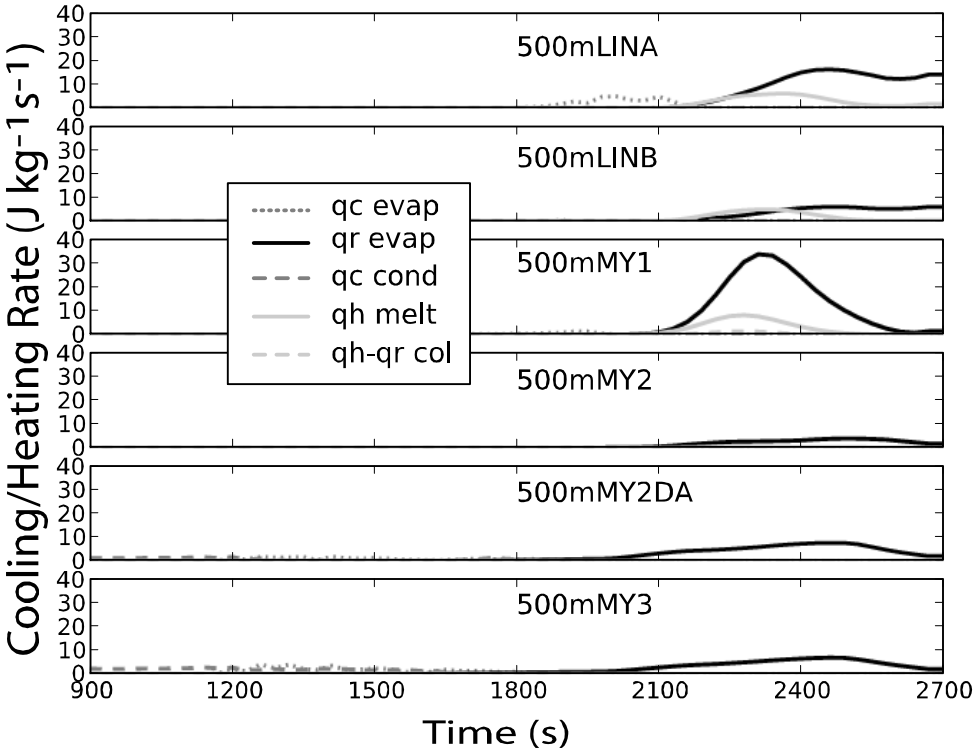

Fig. 5.17. Instantaneous heating/cooling rates vs. time for each of the runs averaged along the trajectory groups shown in Fig. 5.15.

5.4 250-m Simulations

The results of the 250-m experiments are generally similar to those of 500-m, though a few important differences are to be noted. Figure 5.19 shows the domain maximum vertical velocity for the 250-m simulations. Maximum vertical velocities across the simulations range from approximately 30 m s^{-1} to 60 m s^{-1}, which are in general slightly higher than the corresponding values in the 500-m simulations (c. f. Fig. 5.3), which range roughly from 20 m s^{-1} to 50 m s^{-1}, except in *500mLINA* near the end, where the updraft intensifies rapidly to values above 80 m s^{-1}. Also, the variation in maximum updraft magnitude is decreased in the 250-m simulations, with all of the simulated storms maintaining a relatively stable updraft throughout the 2-h period. Qualitatively, the structures of the simulated storms and their associated cold pools at the 250-m grid spacing are very similar to their respective 500-m counterparts (Fig. 5.19), suggesting that further refinement of the horizontal grid spacing beyond 500 m brings out little additional *qualitative* difference in storm-scale structure and behavior, at least inasmuch as the impact of the MP parameterization on reflectivity and cold pool structure are concerned. A budget analysis was carried out on the 250-m simulations using the same criteria as for the 500-m simulations, and the results are shown in Fig. 5.20. It can be readily seen that the downdraft microphysical processes in the 250-m simulations in terms of bulk thermal energy changes are very similar to the 500 m simulations.

For these reasons and the sake of brevity, we will not discuss the 250-m simulations further here. Nevertheless, other differences between the 250-m and 500-m runs, such as the differences in the maximum updraft intensities noted above, can be significant and are likely tied to the actual amount of turbulent energy being

resolved versus that parameterized on the subgrid scale. This topic can be pursued in future work but is beyond the scope of the current study.

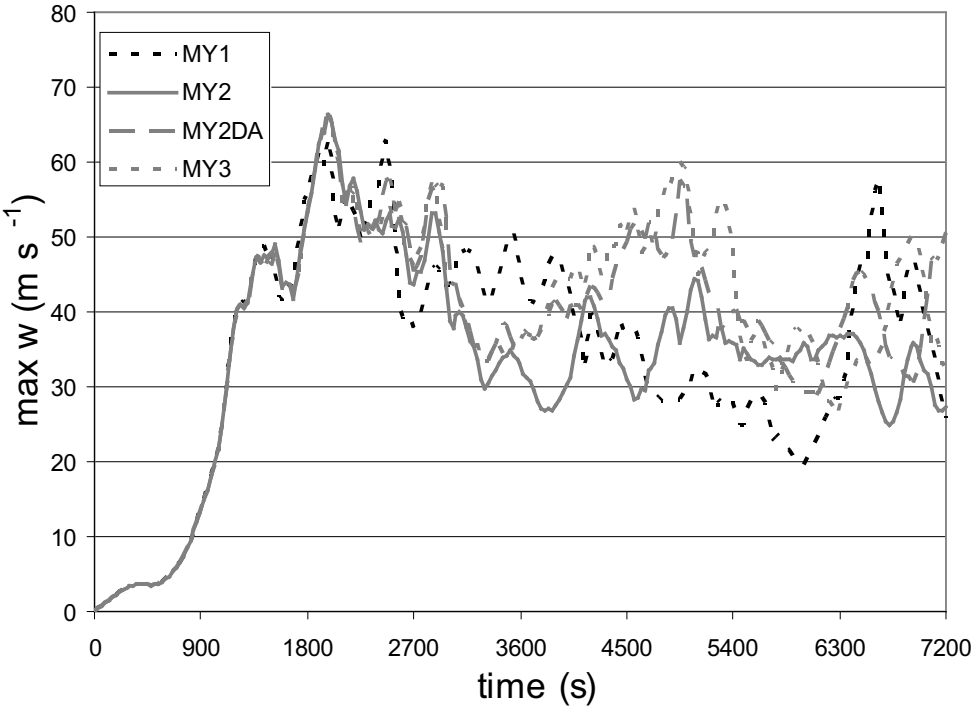

Fig. 5.18. As in Fig. 5.3 except for the 250-m simulations.

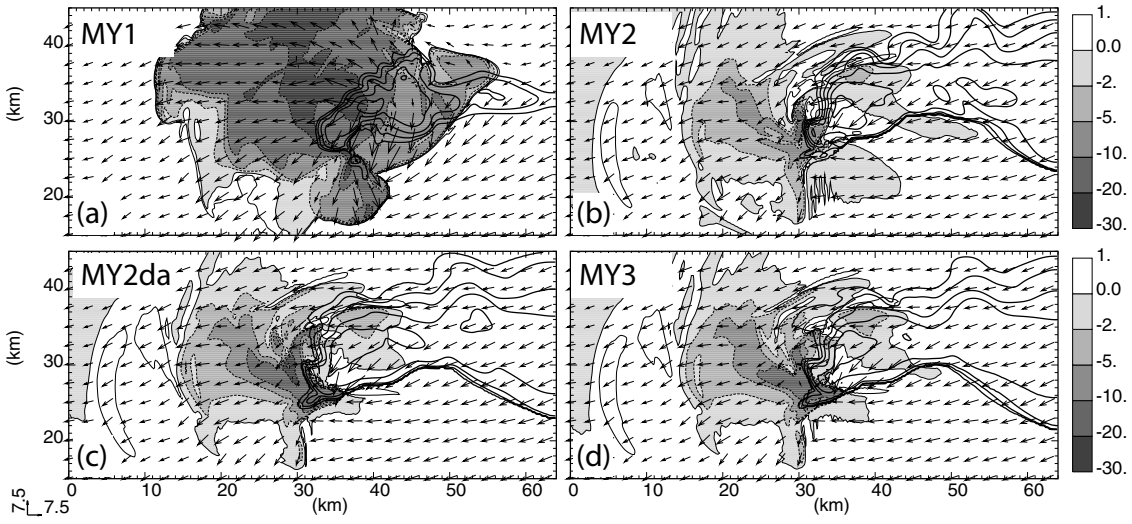

Fig. 5.19. Surface equivalent potential temperature perturbation (grayscale filled contours), reflectivity (black contours, 10 dbZ increment), and horizontal wind vectors (plotted every 2.5 km, 1 step = 7.5 m s^{-1}) for the 250-m simulations at 3600 s: a) 250mMY1, b) *250mMY2*, c) *250mMY2DA*, and d) *250mMY3*. Wind vectors are storm-relative.

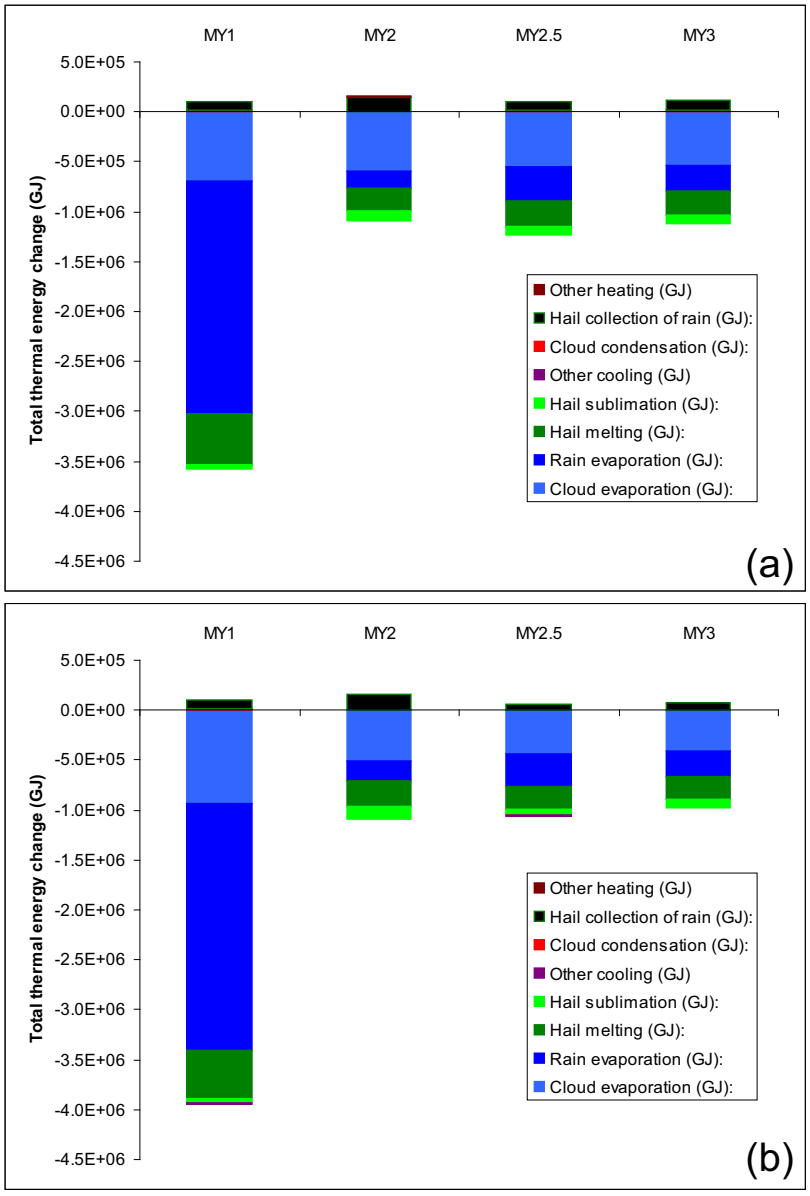

Fig. 5.20. As in Fig. 5.12 but for the 250-m simulations.

5.5 Further Discussion

The results of this study indicate that a significant improvement in various features of the simulated supercell storm occurs when moving from SM to DM microphysics. In the context of this study, a most interesting result is the dramatic reduction in cold pool intensity and size between the SM (when typical values for the

intercept parameters are used) and DM (and higher) simulations, which is consistent with the findings of MY06b, who also found significant improvements in simulated supercell features when moving from SM to DM. The examination of instantaneous fields and the budget and trajectory analyses indicates that both melting of hail and evaporation of rain are reduced in the MM simulations. In addition, far greater variability is seen among the SM runs than among the MM runs. This can be attributed to the different values of fixed-N_{0r} used between *500mLINA* and *500mLINB*, and the differences between the LIN and MY schemes in general. The overall lack of variability in the MM runs may partially be attributed to the fact that all are different versions of the same BMP, but nevertheless indicates that, beyond DM, at least as far as cold pool thermodynamic properties are concerned, relatively small qualitative differences are seen (also consistent with MY06b). We now further discuss the reasons for the large differences between SM and MM.

First, we discuss the well-known sensitivity of evaporation and melting to changes in the intercept parameter N_0. Considering only rain evaporation, for simplicity (arguments for hail melting are qualitatively similar), we note that the parameterization of bulk evaporation of rain used in the MY scheme is given by Eq. (7) in MY05b. Noteworthy is the fact that, neglecting the ventilation term, the bulk rain evaporation rate is directly proportional to the intercept parameter N_{0r}. All other things being equal, a reduction in N_{0r} will produce a corresponding reduction in evaporation rate. The ventilation term, however, helps to counteract this tendency somewhat by accounting for enhanced evaporation of larger drops due to better ventilation. However, as pointed out by Cohen and McCaul (2006), these drops also

fall faster and thus have less residence time in the air, which is parameterized in bulk schemes by a larger mass-weighted terminal fall speed for the drop population.

The dependence of evaporation rate on N_{0r} explains the strong sensitivity to cold pool intensity and size seen in previous studies with SM schemes that varied the value of N_{0x} for rain and/or hail. However, as has been found by observational studies and previous numerical simulations with DM-MP, N_{0r} can vary in time and space, even within the same convective system, such as between the convective and stratiform regions of a squall line – the so-called "N_0-jump"(Waldvogel 1974; Ferrier et al. 1995; Morrison et al. 2008). Thus, a fixed global value of N_{0r} may lead to large errors, even over the course of a simulation or prediction of the same case. As previously discussed, a DM scheme allows N_{0x} to vary independently and presumably consistently with the dynamical and microphysical processes. For a given precipitation event, N_{0x} may be on average larger, smaller, vary greatly, or vary slightly. This inherent flexibility is a primary reason MM schemes are attractive, because they effectively remove some of the difficulty in choosing the "correct" parameters in a SM scheme for a given situation.

In the MY2 simulation, where the shape parameter α_x was fixed at 0 for all precipitating categories, corresponding to exponential distributions, it was shown that values of N_{tx} were significantly reduced in the downdrafts for both rain and hail for comparable or smaller mixing ratios than in the SM simulations, which is equivalent to shifting the DSD toward larger diameters, and correspondingly reducing N_{0x}, for a given mixing ratio q_x, which in turn leads to lower evaporation or melting rates. For the MY2DA and MY3 simulations, the physical meaning of N_{0x} changes, due to the

dependence on α_x, which is allowed to vary over a wide range of positive values. It can be shown that an increase in α_x given q_x and N_{tx} actually enhances evaporation because, while the DSD spectrum narrows and the numbers of both largest and smallest drops decrease, the number of drops in the middle part of the spectrum increases such that the total surface area of the drops increases (Cohen and McCaul 2006).

MY05a found that size-sorting is one reason for the larger values of D_{mx} (and thus smaller N_{0x} in the exponential MY2 case) at the low levels, due to the differential fall speeds of the number concentration and mixing ratio fields, with the latter falling faster than the former. Physically, this translates to larger raindrops and hailstones falling faster than smaller ones. The larger particles evaporate or melt less efficiently, leading to smaller magnitudes of evaporation and melting rates in the low-level downdrafts. In a SM scheme, however, a single fall speed is used for all particles in the distribution. For most SM schemes, including the ones used herein, that predict mixing ratios, the mass-weighted mean terminal fall speed is used. This leads to the unphysical behavior of the smallest particles falling too quickly, and the largest particles too slowly. Since more small particles are allowed to reach lower levels, this directly translates into larger, unphysical, evaporation rates in the low-levels (cf. Fig. 5.9).

In addition to the effect of size-sorting, for a SM scheme that fixes N_{0r}, evaporation of a population of raindrops necessarily yields an increase in slope. This leads to yet another unphysical behavioral characteristic of SM schemes that fix N_{0r}. An increase in slope λ_r for an exponential distribution, while reducing q_r and holding

N_{0r} constant, is physically equivalent to reducing the concentration of the largest drops from the distribution faster than the concentration of the drops at the small drop end of the spectrum, a result contradicting physical intuition and the results of detailed studies of evaporation within rainshafts (e.g., Tzivion et al. 1989; Li and Srivastava 2001). It can be seen that evaporation in the fixed-N_{0r} case actually shifts the entire population of drops towards smaller diameters, leaving a considerable number of small-to-medium-size drops contributing to high evaporation rates; in reality these drops are likely to be quickly depleted (except for perhaps the very smallest drops; see previous references). It is believed that these two unphysical effects together are primarily responsible for the large evaporation rates and the attendant strong downdrafts and cold pools seen in many past and contemporary simulations of convective storms using typical SM schemes. However, SM schemes that specify the mean-mass diameter D_{mx} or characteristic diameter D_{nx} (e.g., van den Heever and Cotton 2004) instead of N_{0x} would not suffer from this particular issue (the increase of slope during evaporation), while the issue of sensitivity to the choice of parameter values still remains. On the other hand, in the MM schemes used in this study, the slope (and thus D_{mr}) is assumed to remain constant during the process of evaporation (but not melting of hail, where D_{mh} decreases during the melting process). As such, evaporation would reduce both q_r and N_{tr} at the same relative rate, leading to a corresponding reduction in N_{0r} for the exponential DSD case. Physically, this translates to individual particles across the distribution being shifted down the spectrum towards smaller sizes as they evaporate, with the population as a whole maintaining the same mean mass. The smallest drops leave the distribution at the

small end by being converted to vapor, a process much more physically reasonable than the SM case. This DM closure assumption for the rate of decrease in N_{tr} is still not entirely correct, however, since it implies that the mean-mass drop diameter does not change due to evaporation, and thus overestimates the rate of decrease in N_t (Seifert 2008). Nevertheless, it is a distinct improvement over the fixed-N_{0r} assumption used in most SM schemes.

To test the above hypotheses regarding the effects of size-sorting and the differences between the treatments of pure evaporation in the SM and MM cases, we performed idealized 1D simulations of a distribution of rain drops falling in sub-saturated air, using all four versions of the MY scheme. To cleanly isolate these effects, the simulations were made as simple as possible, while still being physically reasonable. The following restrictions were applied: only the processes of rain evaporation and sedimentation were modeled and no collision or breakup was allowed (the reader is referred to Feingold et al. (1991) for a discussion on the importance of these effects on evaporation). The atmosphere was assumed quiescent and isentropic with a base state potential temperature of 300 K, a surface pressure of 1000 hPa, and a constant relative humidity of 0.6. No feedback from the evaporation of the falling rain to the atmosphere was allowed to either the temperature or moisture fields. Physically, this is equivalent to assuming that the rain is falling into a region where air is continually being replaced by sub-saturated air at a particular potential temperature. Since the convective downdrafts in this study were sub-saturated and were characterized by entrainment of dry mid-level environmental air, this is a reasonable assumption for the purposes of these tests. At the top boundary, rainwater

with an exponential distribution and a mixing ratio of 1 g kg^{-1} was specified as the boundary condition for the falling rain field, with a constant intercept parameter of 8.0×10^6 m^{-4} -- that of the well-known Marshall-Palmer distribution (Marshall and Palmer 1948). The initial rain mixing ratio was zero inside the domain. The vertical grid spacing was a uniform 100 m over a depth of 5 km, and a time step of 5 s was used.

The results of the tests are summarized in Fig. 5.21. In addition to the four control simulations shown in Fig. 5.21a-d where both size-sorting and evaporation are active, results using the MY2, MY2DA, and MY3 schemes but with size-sorting turned off are also shown (Fig. 5.21e-g) The vertical profiles all reached a steady state after approximately 30-45 min and thus those at 45 min are shown. As expected, the MY1 scheme shows the most evaporation over the greatest depth, followed by the MY3, MY2DA, and MY2 schemes in order of decreasing evaporation. The removal of size-sorting leads to stronger and deeper evaporation, though not as great as the MY1 case.

As discussed previously, in the MM schemes, N_{0x} and λ_x vary independently as a result of (1) size-sorting, and (2) evaporation and melting, as well as from other processes not considered here (i.e. those which lead to overall smaller magnitudes of mixing ratios of rain and hail in the MM runs in the first place). In contrast, the SM schemes by nature impose *a priori* a single-valued functional relationship on N_{0x} and λ_x. It is worth emphasizing at this point that size-sorting cannot even be modeled without allowing independent variation of the distribution parameters (e.g., one cannot fix N_{0x} and still model size-sorting). The results of the 1D column

experiments using the MM schemes corroborate the argument that size-sorting on one hand, and the improved treatment of evaporation on the other, both lead to reduced evaporation of a falling rain shaft, and by extension, weaker, shallower downdrafts and weaker cold pools, relative to the SM schemes. Again, in the case of size-sorting, the SM schemes cannot model this process, and, in the case of evaporation, the MM schemes are free to specify a different relationship between N_{0x} and λ_x relative to other processes (in this case, by fixing λ_x instead of N_{0x}). It should be noted that in a more realistic scenario, the cooling by evaporation would tend to drive a downdraft, and thus, in the case of the 1D MY1 simulation (Fig. 5.21a), where most of the rain actually evaporates before reaching the ground, a strong convective downdraft would tend to lead to a downward displacement in the peak of the evaporation rate profile, as well as leading to more q_x at low levels. Similar arguments apply to the other schemes, but obviously dictated by the respective strengths of the diabatically-enhanced downdrafts. Finally, the results of the 1D simulations suggest that size-sorting has a significant impact on total evaporation in a falling rainshaft. However, sensitivity tests that turned off size-sorting in the full 3D model resulted in only slightly stronger and larger cold pools (not shown), suggesting that the combined impact of many other processes may dominate over this effect in more realistic cases. The relative importance of size-sorting versus the other processes considered here is still under investigation.

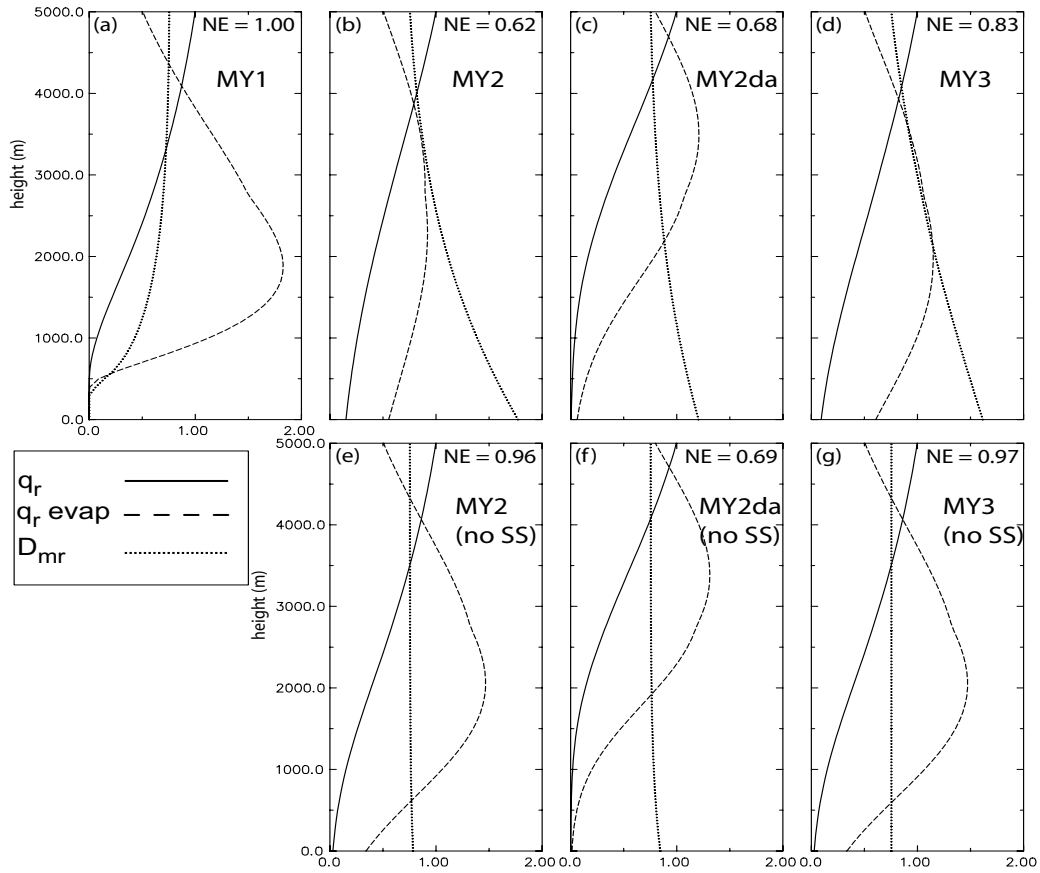

Fig. 5.21. Vertical profiles of rain mixing ratio q_r (kg kg^{-1}, solid), mean-mass diameter D_{mr} (m, dotted), and evaporation rate (kg kg^{-1}s^{-1}×1000, dashed) for the simple sedimentation-evaporation column model for a) MY1, b) MY2, c) MY2DA, d) MY3, e) MY2 with no size-sorting, f) MY2DA with no size sorting, and g) MY3 with no size sorting. Also shown in each panel is the normalized total evaporation (NE) over the previous 45 min relative to the MY1 scheme.

5.6 Conclusion

In this chapter, we have performed high-resolution idealized simulations of the 3 May 1999 OK tornadic supercell thunderstorms. The goal of this study was to test the impact of a new multi-moment (MM) microphysics scheme on the development and evolution of the storms, and in particular on the downdraft and cold pool properties. We found that the MM schemes, in general, performed better than their single-moment (SM) counterparts employing typical values of the intercept

parameters. The MM schemes showed clear and significant improvements in the cold pool and reflectivity structures of the storms compared to the observations. The MM schemes showed overall weaker and moister cold pools, which is consistent with available observations. In addition, the forward flank region was more developed and closer to the size and shape of the observed forward flank regions of the mature supercells on this day. This was attributed to the process of size-sorting of hydrometeors, which is reasonably handled in the MM schemes, but not in the SM schemes (MY05a).

We further demonstrated through budget and trajectory analyses that the MM schemes yield less water mass (both liquid and solid) in the low-level downdrafts and larger average particle sizes, both of which lead to significantly lower amounts of evaporation and melting and associated diabatic cooling. The vertical profiles of evaporation and melting are also altered in the MM schemes, with significantly less evaporation and melting near the surface, particularly in the forward flank region of the storm. Thus, while the forward flank downdraft reaches the surface at times in the SM simulations, it remains elevated above the surface in the MM simulations, which is more consistent with the observations. In addition, the source region of the air reaching the surface in the downdrafts is significantly lower in the troposphere in the MM simulations than in the SM ones, as is also reflected by the higher θ_e in the cold pools of the MM storms.

Through an examination of the parameterized processes of evaporation and melting in the bulk microphysics schemes used in this study, we show that the MM schemes have a few important advantages over the SM schemes in their treatment of

these processes, which are mostly related to how the drop size distributions (DSDs) are allowed to evolve in the MM schemes. In particular, a proper treatment of size-sorting of hydrometeors leads to more large particles at the low levels, and hence less evaporation and melting there. Also, the change in the DSD during evaporation or melting is handled in a more physical manner in the MM schemes by allowing N_{0x} to decrease during the evaporation process, while SM schemes hold it fixed. Results from a simplified column model highlighting sedimentation and evaporation confirm the role of the above processes. Taken together, the above two advantages with the MM schemes, and possibly other direct and indirect effects, lead to a much better representation of evaporation and melting in the low-level downdrafts of the simulated supercell storms examined in this study.

In the next chapter, we will discuss results of ongoing work: a new set of real-data simulations, similar to those briefly discussed in Chapter 4, but with the smaller grid-spacings used in the idealized simulations, to examine the robustness of the idealized results under more realistic settings. The storm environment is inhomogeneous and complete physical processes are included. The simulations are conducted at high resolutions (250 m and 100 m) to examine the impact of the MP scheme on tornadogenesis. This is the MM extension of the SM study by Snook and Xue (2008) that examined the microphysical effects on tornadogenesis. Finally, in the future, we wish to make a more rigorous comparison of the results of the MM simulations of the hydrometeor fields in the supercells with observations, such as by comparing with polarimetric radar retrievals of hydrometeor fields.

Chapter 6 Real-data Simulations of the 3 May 1999 Outbreak

6.1 Introduction

In Chapter 5, idealized simulations of the 3 May 1999 supercell storms were conducted. In that chapter, the impact of SM and MM microphysics on the downdraft, cold pool, and reflectivity properties of the storms was analyzed and reasons for the improvement in the simulation of each of these features when using the MM schemes were given. It was noted that the idealized results still needed to be tested in a more realistic real-data framework to determine the robustness of the results. To that end, in this chapter, we turn to an entirely new set of real-data experiments. While the purpose of Chapter 5 was to analyze in detail the microphysical processes involved in the downdraft and cold pool development, in this chapter, we analyze the impact of the microphysics parameterization, both SM and MM, on the numerical prediction of the most significant supercell storm in the outbreak, "storm A", and its associated F5 tornado that struck the towns of Bridge Creek, Moore, and Oklahoma City, Oklahoma. The ARPS model is run in terrain-following coordinates with telescoping nested grids using inhomogeneous initial and boundary conditions derived from 3DVAR analyses of the atmosphere in the afternoon and evening of 3 May 1999, as opposed to the idealized simulations, which used a single sounding specifying a homogeneous environment for the storm. In addition, the model is run in full physics mode, including surface and radiation physical parameterizations, as opposed to the simulations in Chapter 5, which neglected these processes and assumed flat, level terrain.

The layout of this chapter is as follows: in section 2 we provide an overview of the numerical experiment setup, which included nested grids at 3 km, 1 km, 250 m, and 100 m horizontal resolutions; in section 3 we discuss the results of the 3 km and 1 km grid simulations; in section 4 we present results of the 250 m simulations, with a particular emphasis on the RFD thermodynamics through comparison with the mobile mesonet observations, and on the tornadic circulations present in these runs and their relationship with the observed F5 tornado. The results of the 100-m experiments are qualitatively very similar to the 250-m results except that the tornadic vortices are more intense; they will therefore not be discussed in detail. Section 6 summarizes the chapter and discusses ongoing and future research plans, which include a full analysis of the results of the 100-m experiments.

6.2 Experiment Setup

For all experiments, we use the ARPS as the prediction model (Xue et al. 2000; Xue et al. 2001; Xue et al. 2003) within the data assimilation cycles and for the predictions, with the ARPS 3DVAR system (Gao et al. 2004) used for the data analyses. We use multiple-level one-way-nested grids with grid spacings of 3 km, 1 km, and 250 m, and 100 m during the forecast period (Fig. 6.1). Data assimilation is performed on the 3 and 1 km grids, assimilating different types of data on each. The purpose of the 3 km grid is to capture the mesoscale environment while the 1 km grid aims to resolve the storms themselves; these two grids will be referred to as the “outer grids” in this chapter. The 250 m and 100 m grids aim to simulate near tornado-scale features within the storms, without further data assimilation; these two grids are referred to as the “inner grids”.

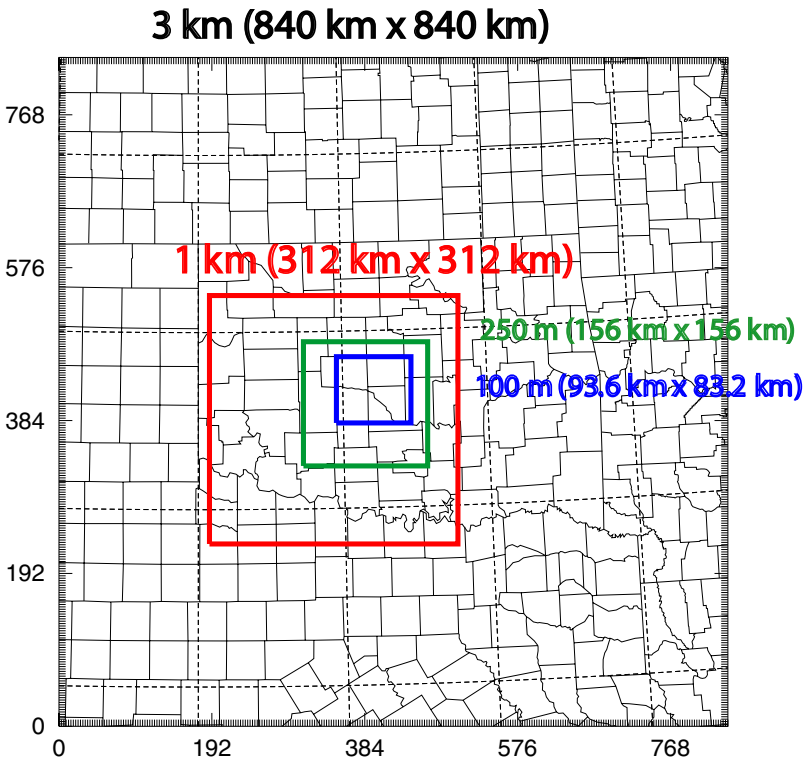

Fig. 6.1. Four multi-nested computational grids, at 3 km, 1 km, 250 m and 100 m horizontal resolutions, used by real-data experiments reported in this chapter. Also shown are county borders. The 100 m grid is roughly centered on Oklahoma City.

For a given grid, experiments are differentiated by the microphysics schemes/configurations employed. As in Dawson et al. (2009), and Chapter 5 of this dissertation (on which it is based), we will use the following naming convention for individual experiments in this study. The simulation naming convention throughout this chapter will follow the template *[dx][scheme]*, where *[dx]* is the horizontal grid spacing of the simulation and the units and *[scheme]* is the abbreviated microphysics scheme/configuration in capitals listed in Table 6.1. On the outer grids, a single set of control experiments, *3kmMY3* and *1kmMY3*, is performed using the 3-moment MY scheme (with the exception of sensitivity tests, to be discussed). On the inner grids,

several experiments using different microphysics schemes or configurations are performed. Experiment *1kmMY3* nested within *3kmMY3* therefore provides the control initial and boundary conditions for the inner grid experiments. Four experiments were run at 250 m resolution (Fig. 6.2), with MY1, MY2, MY2DA and MY3 schemes. The 100 m experiments was done using MY3 scheme only. The results of these experiments are compared with each other and with available observations.

Table 6.1. List of microphysics schemes and descriptions used for the 250-m experiments.

Microphysics scheme/configuration	**Description**
MY1A	Single-moment version of the MY scheme with N_{0r} = $8.0\text{x}10^{6}$ m^{-4}
MY1B	Single-moment version of the MY scheme with N_{0r} = $4.0\text{x}10^{5}$ m^{-4}
MY1	Single-moment version of the MY scheme (q predicted)
MY2	Double-moment version of the MY scheme (q and N_t predicted)
MY2DA	As in MY2 but with diagnostic relations for α
MY3	Triple-moment version of the MY scheme (q, N_t and Z predicted)

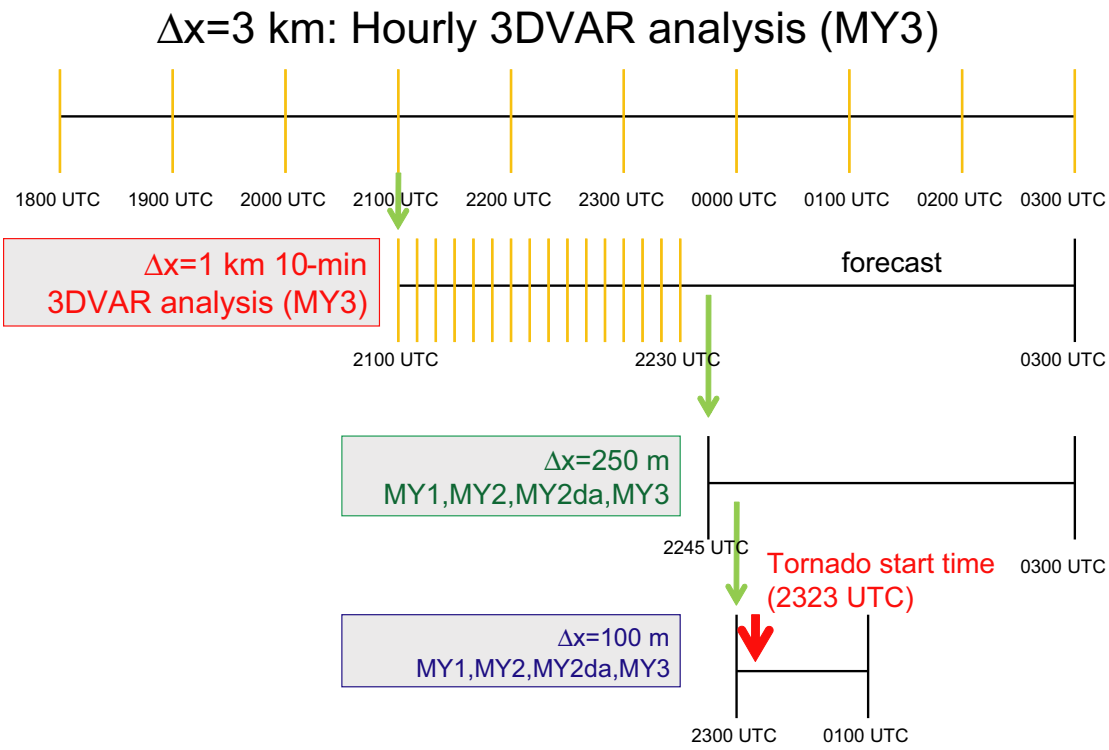

Fig. 6.2. Schematic of the real-data experiment design. Vertical orange bars represent analysis times, vertical black bars start and end times of forecasts, and horizontal bars represent forecast cycles.

6.3 Outer Grid Experiments

6.3.1 3 km grid

As shown in Fig. 6.2, we performed hourly data assimilation cycles from 1800 UTC to 0300 UTC on the 3 km grid. This time period covers from a couple of hours prior to the initiation of convection in OK to a couple of hours after the F5 tornado swept through the OKC area. The initial analysis background at 1800 UTC was taken from the 32-km North American Regional Reanalysis (NARR), interpolated to the 3 km grid; the 3-houly NARR analyses also provided the boundary conditions for the 3 km grid. When available, the following conventional data were assimilated using the ARPS 3DVAR each hour: upper-air soundings (RAOB), wind profiles from the

National Profiler Demonstration Network (NPDN), Surface Aviation Observations (SAO), Oklahoma Mesonet observations (OKMESO), and buoy observations (BUOY). In addition, visible and infrared satellite images from GOES 8 were assimilated through the ARPS Complex Cloud Analysis (CCA) system (Zhang et al. 1998), in order to analyze the extensive cirrus canopy that was present over much of the southern Plains during the event. Radar data was not used on the 3 km grid, but was used on the 1 km grid, to be discussed in the next section. The 3-moment version of the MY microphysics scheme (MY3) was used.

Since the main purpose of the 3 km grid was to provide a reasonably accurate set of boundary conditions and a 'spun-up' analysis background for the 1 km grid, we will only briefly describe the results here. On the 3 km grid, no convection forms in the domain over the entire 9-h assimilation period. Both visible and infrared satellite data were included in the cloud analysis at each hour during the assimilation period, and the presence of high-level cirrus clouds might have helped suppress convection on this grid. The presence of “spurious” convection inherited from the 3 km grid can actually be a detriment for high-resolution simulations in this case. RSR02 found in their numerical study of this same outbreak, the artificial removal of the cirrus canopy (by making them completely transparent to visible radiation) resulted in “over-convecting”; too many storms initiated in the warm sector and led to many detrimental storm interactions. Future studies can examine this sensitivity in more detail to determine why the real atmosphere was able to produce the isolated supercells even with an extensive cirrus canopy limiting heating and instability but the 3-km model failed to. We do note here that our 3-km experiment is not a free

simulation, but one with hourly analysis-prediction cycles. No convective-scale observations, from, e.g., radars, were assimilated. Our primary goal is for it to provide a proper definition of the storm environment that influences the one-way nested grids through boundary conditions. We leave the job of capturing the convective storms to the nested higher-resolution grids.

6.3.2 1 km grid

The main purpose of the 1 km grid was to capture the individual storms through storm-scale analysis and forecasting, in particular, storms A and B on the day of May 3rd, as defined by RSR02. Intermittent assimilation cycles assimilating level II reflectivity and radial velocity data from the Twin Lakes WSR-88D radar (KTLX) at 10-min intervals were performed on the 1 km grid (Fig. 6.2). In addition, Oklahoma mesonet observations were also assimilated at these same intervals. Other sources of data, such as standard SAO surface observations, NPDN data, and GOES 8 visible and infrared satellite imagery were also assimilated whenever available. The assimilation window spans a 90-min period from 2100 UTC to 2230 UTC 3 May 1999 (c.f. Fig. 6.2) when both storms A and B were in their developing stages. The radar data help establish and initialize these storms within the numerical model. Our goal here is to study the storm evolution and their sensitivity to microphysics after they are established through data assimilation.

Our overall radar data assimilation strategy is similar to and inspired by the studies of Hu et al. (2006a; b). For each analysis time, we chose the volume scan nearest in time to the regular 10-minute intervals. However, no temporal interpolation of radar data was performed. The reflectivity data was brought in

through the CCA, after first being mapped to the ARPS grid, and the temperature and moisture profiles in areas of reflectivity greater than 40 dBZ were adjusted using the diluted moist-adiabat option (Brewster 2003). Precipitation hydrometeor fields were diagnosed from the radar reflectivity according to the Kessler reflectivity equation (K69) for rain, and the formulae of Rogers and Yau (1989) for snow and hail. This is the "KRY" method used in Hu et al. (2006). A sensitivity test using the "SMO" scheme discussed in that paper resulted in qualitatively very similar evolution of the predicted storms (not shown). Another sensitivity test (not shown) in which the hydrometeor fields were not updated during the CCA also resulted in similar forecasted evolution of the storms, but with a slightly inferior prediction of the track of storm A.

The CCA in ARPS was designed for the SM-LIN microphysics scheme and only adjusts the mixing ratios of the hydrometeors (cloud, rain, ice, snow, and hail), based on pre-specified intercept parameter values within regions containing observed reflectivity above a certain threshold. The TM mode of the MY scheme requires initial values of the total number concentration and radar reflectivity factor in addition to the mixing ratios for the precipitating categories. Thus, at each radar analysis time, within the cloud analysis region, these fields were diagnosed based on assumed exponential size distributions with fixed values of the intercept parameter. Outside the cloud analysis regions, these fields were left at their background values (i.e. no removal of cloud and precipitation fields outside of observed reflectivity regions was performed). This method ensures only that the microphysics scheme has initial values of all three moments that are consistent with each other at each grid point. In

any case, as previously mentioned, the updating of hydrometeor fields has a comparatively smaller impact on the subsequent forecast than the in-cloud temperature and water vapor adjustment.

Since the MY scheme contains separate categories for graupel and hail, the graupel fields were not updated by the cloud analysis, and were left at their background values. Since the graupel field only contributes a small amount to the total reflectivity compared to the rain and hail fields (see, e.g. MY06a, their Fig. 11), the error that results from neglecting the updating of this category in the CCA is likely small. Nevertheless, future work should refine the CCA for use with MM schemes, including allowing for gamma distributions and the additional graupel category.

The radial velocity data were assimilated via 3DVAR and a weak 2D divergence constraint was imposed in the 3DVAR cost function (see Hu et al. 2006). To determine the impact of assimilating the radial velocity data, an additional sensitivity test was performed (*1kmMY3noRV*) which excluded the radial velocity data. Fig. 6.3 shows the low-level (2 km ASL or approximately 1.7 km AGL) vorticity and reflectivity fields in a region focused on storm A at the final analysis time of 2230 UTC for the background (10-min forecast from 2220 UTC) and analysis, for both *1kmMY3noRV* (left) and *1kmMY3* (the control, right). It should be pointed out that the background field in *1kmMY3* carries over information of assimilated radial velocity data, propagated forward by the model, of the previous analysis cycles. The mesocyclone circulation indicated by positive vorticity values on the order of 2-4 x 10^{-3} s^{-1} on the southwest flank of the storm is present in *1kmMY3*

but not in *1kmMY3noRV*, indicating the value of assimilating the radial velocity observations.

Fig. 6.4 shows the forecast surface 30-dBZ reflectivity contours (dashed) for *1kmMY3* at 30-min intervals starting at 2300 UTC (30-min into the forecast cycle), as compared to the corresponding contours observed at the lowest elevation of KTLX radar (solid). The overall track and evolution of the forecasted storm followed that of the observed storm rather well; both the forecasted and observed storm moved east-northeast through central OK, with the development of a prominent hook echo associated with the development and intensification of the long-track tornado as the storm matured. The forecast storm initially moved somewhat faster than the observed storm, resulting in an ENE displacement error of approximately 15-20 km. The precise reason(s) for this speed and displacement error is unknown, but may be related to the adjustment in the early part of the forecast cycle, during which the storm's updraft and mesocyclone were organizing. There is also indication that the forecast mid-level winds were somewhat too strong (not shown). The cold pool in the forecast storm was also stronger than that objectively analyzed from available surface observational data (including OK mesonet data, see Fig. 6.5). This may be partly due to the insufficient observation density required to capture storm-scale cold pools in the analysis (Fig. 6.5a). The sensitivity of cold pool strength and size to microphysics will be discussed further in the following section.

The subsequent forecast of the track and evolution of storm A in *1kmMY3noRV* (not shown) was noticeably inferior to that in *1kmMY3*: the track was too far to the NW and the storm displayed a tendency to develop additional

convection on its outflow, growing upscale into a quasi-linear convective mode by the end of the forecast period (0300 UTC). A final note regarding the forecast of storm A in *1kmMY3*: the storm maintained its intensity throughout the forecast period (2230 – 0300 UTC), while the actual storm dissipated by 0200 UTC (c.f. Fig. 5.7).

While the assimilation strategy used here is not as sophisticated as in Hu et al (2006a; b) (for example, no tilt-by-tilt temporal interpolation to the analysis times was performed on the radar data), we nevertheless consider it sufficient for the purposes of this study, which was mainly to provide a reasonable set of initial conditions from which to launch a storm scale forecast. Future work is planned to focus more on the data assimilation strategy, including finding the optimal frequency and duration of the radar data assimilation, as in Hu et al. (2007). However, several preliminary sensitivity tests that we have performed did not lead to significantly better results than the control experiment presented here. In the result of this chapter, we focus on presenting and analyzing the results of 250 m simulations, which are nested within the 1 km control simulation, starting from its 15 minute forecast.

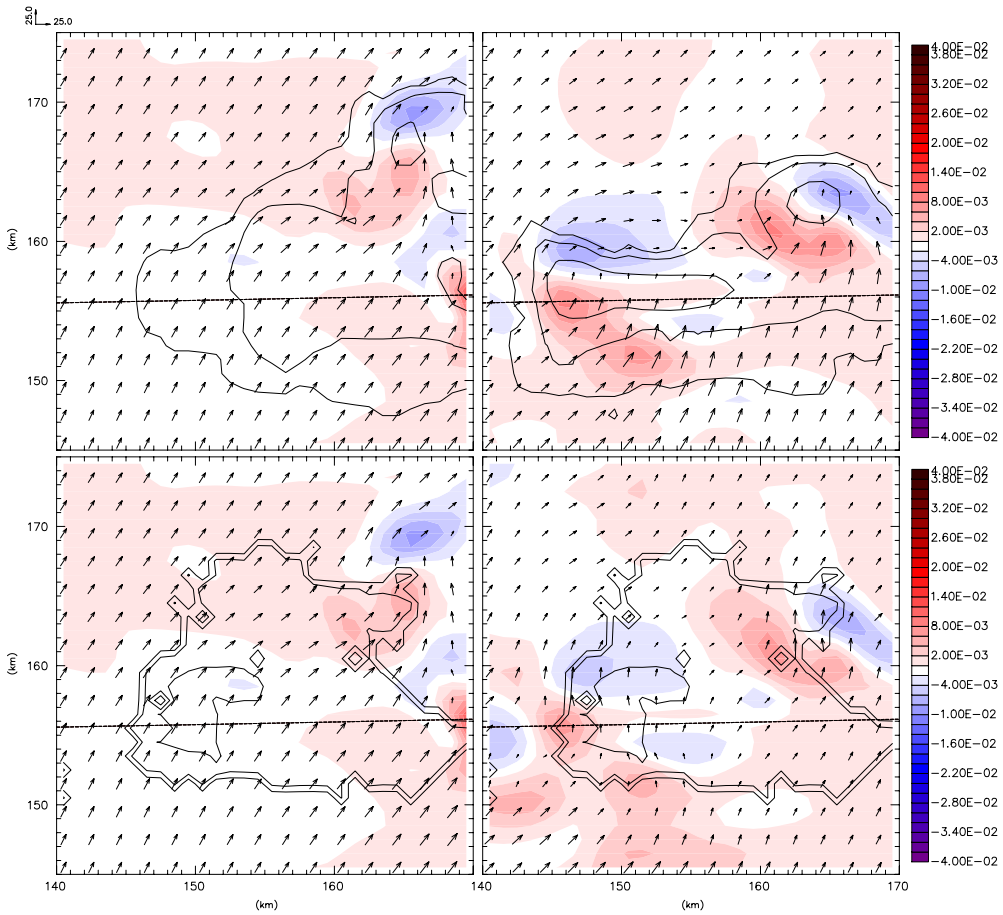

Fig. 6.3. Vertical vorticity (color-shaded), reflectivity (black contours, 20 dbZ increment), and wind vectors (every 2.5 km, scale shown at upper left) at 2 km ASL for the background (top row) and analysis (bottom row) at 2230 UTC 3 May 1999 for (left) *1kmMY3* sensitivity run without radial velocity analysis, and (right) *1kmMY3* which includes radial velocity.

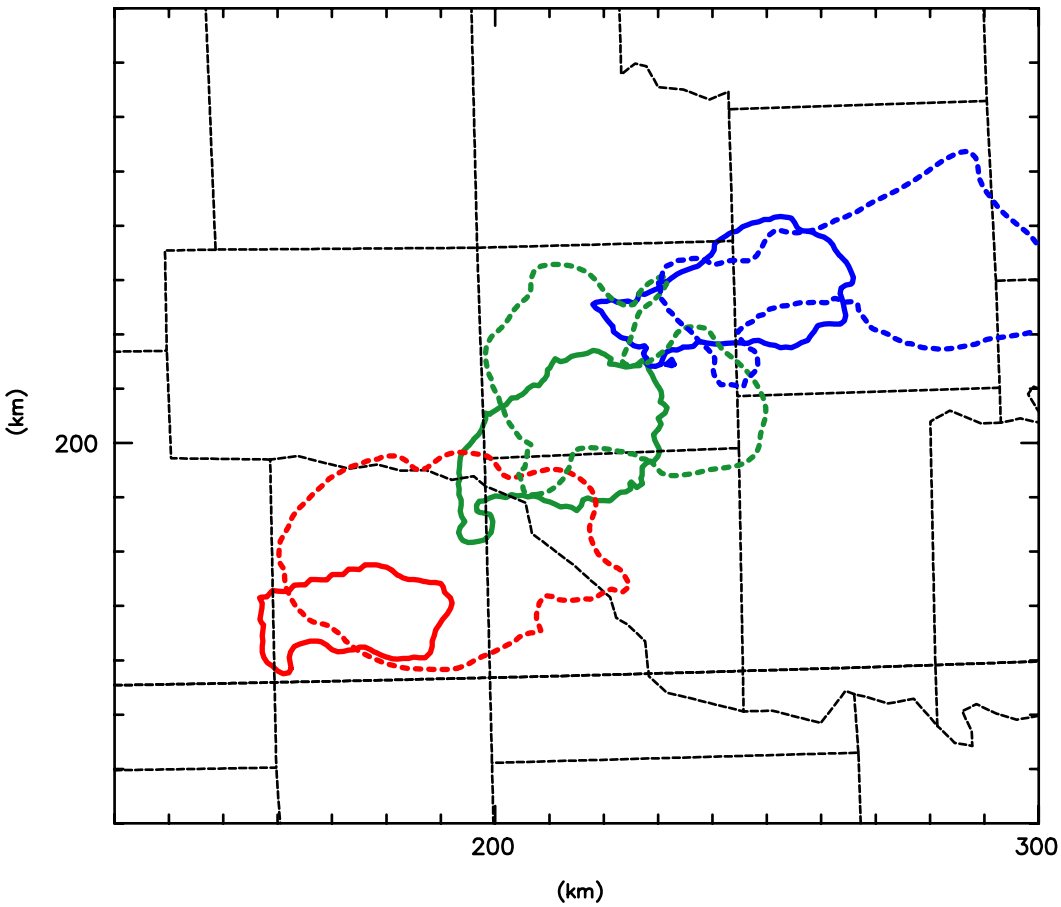

Fig. 6.4. Observed (solid) and forecast (dashed) 30 dbZ reflectivity contour for storm A in *1kmMY3* at 2300 UTC (red), 0000 UTC (green), and 0100 UTC (blue).

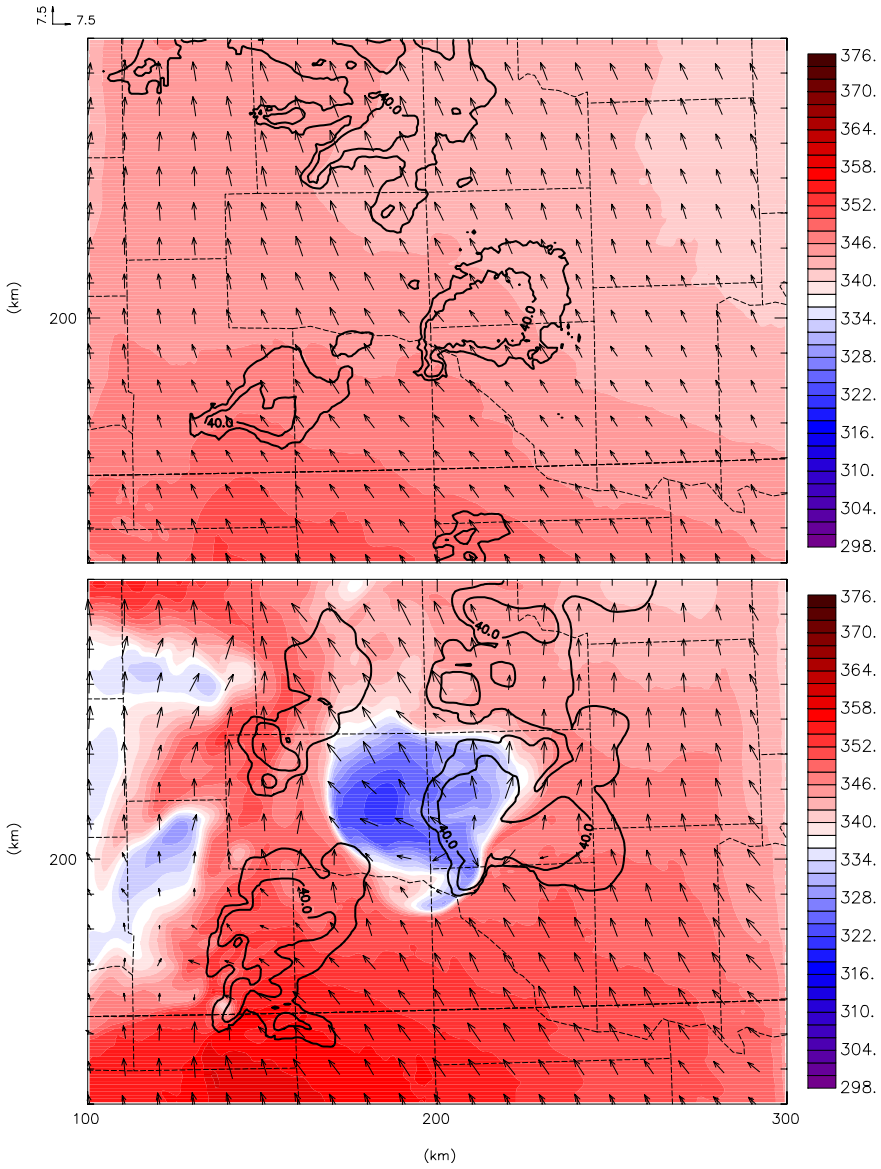

Fig. 6.5. a) 0000 UTC 4 May 1999 3DVAR objective analysis of surface equivalent potential temperature (color filled), observed base reflectivity from KTLX (black contours; 20 dbZ increment), and wind vectors. b) As in a) but for the 1.5 h forecast from experiment *1kmMY3* valid at 0000 UTC 4 May 1999.

6.4 250 m Experiments

The initial and boundary conditions of the 250-m grid experiments were interpolated directly from the 15-min forecast of *1kmMY3*, valid at 2245 UTC. This time was approximately 40 min prior to the genesis of the F5 tornado. The purpose

of the experiments on the 250-m grid was to explore the impact of varying the microphysics scheme on the forecast track of storm A and associated tornadic circulations. In particular, we are interested in the differences in RFD thermodynamic properties across the schemes and their relationship to simulated tornadogenesis. The same microphysics schemes as in the idealized simulations of Chapter 5 were employed, with the exception that the LIN scheme was not used, and two variations of the MY1 scheme, MY1A and MY1B were explored, which are analogous to the experiments LINA and LINB in Chapter 5 (see Table 6.1). That is, MY1A used the default M-P value of 8.0 x 10^6 m^{-4} for N_{0r}, while MY1B used the reduced value of 4.0 x 10^5 m^{-4}.

The layout of this section is as follows. First, qualitative comparisons of the surface cold pools and reflectivity structure across the experiments are made, and compared and contrasted with the results of the idealized simulations in Chapter 5. A budget analysis similar to that in Chapter 5 is also performed. Then, we discuss the presence of tornado-strength vortices in the simulations, and compare the tracks and intensities with the observed tornado "A9". Finally a discussion of preliminary results of an analysis of the near-tornado RFD dynamics and thermodynamics is given.

6.4.1 Comparison of surface cold pools and reflectivity structure

Given the direct impact on the cold pool and reflectivity structures of microphysics schemes, we first examine the simulated surface cold pools and reflectivity structures in the 250-m experiments. Fig. 6.6 shows the 1.5-h forecast surface temperature, wind vectors and reflectivity in a small region centered on the

storm at 0030 UTC, for experiments using different microphysics schemes. The corresponding single time 3DVAR surface analysis that included OK mesonet data (but not radar data) is shown in panel (a). The dewpoint temperature and equivalent potential temperature are shown in place of temperature in Fig. 6.7 and Fig. 6.8, respectively. The time shown is representative of the surface features during the mature stages of these simulations. Fig. 6.6 indicates that the surface temperature in the inflow region of the forecast storms compares well with the analysis (Fig. 6.6a). However, the inflow surface dewpoint temperature is too high by 2-3 K in all forecasts (Fig. 6.7), compared with the analysis. Extracted soundings (not shown) in the inflow regions indicate that this leads to a saturated boundary layer. This would in turn be expected to suppress evaporative cooling of rain falling into the boundary layer, but as will be discussed in a later section, many of the low-level downdrafts are at least partially dynamically forced, leading to subsaturated conditions in the downdrafts and allowing evaporation of rain and cloud to occur. Depending on the depth of the downdrafts, the relative humidity of the inflow may not be relevant to evaporation in the core or forward flank downdraft region, but probably impacts the shallower downdrafts in the hook echo region that contain at least partially re-circulated inflow air. In any case, the observed 0000 UTC 4 May 1999 OUN sounding (c.f. Fig. 5.1a) does indicate very high boundary layer relative humidity. In addition to the suppression of evaporation, the extra moisture in the storm inflow results in greater thermodynamic instability, which would be expected to increase the storm's strength and possibly longevity. Thus, in the future, sensitivity tests that

reduce the surface moisture will be performed to assess the impact on the storm forecasts.

There is clearly a large amount of variability amongst the schemes; in general, the MM runs and the SM run with reduced N_{0r} (*250mMY1B*) show weakest cold pools, in terms of both temperature and moisture deficit. This is consistent with the results of the idealized simulations in Chapter 5. However, the extent of the cold pool is generally significantly larger across all the simulations than in the idealized counterparts. Also, the variability amongst the runs is greater than in the idealized experiments, which may be expected considering the larger number of physical processes active in the real-data experiments, and due to the inhomogeneous mesoscale environment, leading to a higher degree of nonlinearity in the predicted characteristics of the storms. However, further work is clearly needed to better explain these differences. For example, *250mMY2DA* bucks the trend of the other MM runs by displaying a cold pool of comparable size to, but less intense than, that in *250mMY1A*, and also displays a larger region of very warm air near and behind the hook echo (compare Fig. 6.6b,e). These "warm RFD pockets" will be discussed further in section 6.4.4. A closer examination of the evolution of the storm in *250mMY2DA* indicate that at earlier times (not shown), a large cold downdraft developed and produced surging outflow, similar to the SM runs. As the forecast proceeds, however, the cold pool in *250mMY2DA* becomes generally weaker and more like that in *250mMY2* and *250mMY3*, in that the hook echo region becomes dominated by relatively low θ_e perturbations.

Of note is the lack of an appreciable cold pool in the surface analysis. As discussed previously, this is at least partly due to the relatively coarse horizontal resolution of the OK mesonet observations, which have about one station per county, insufficient to capture storm-scale details. The 3DVAR analysis procedure contains further spatial smoothing. The mobile mesonet observations of M02 on storms A and B provide some information about the temperature and moisture fluctuations at high spatial and temporal resolutions, but were limited to small areas near the tip of the hook echo (and tornado); they indicated temperature and moisture deficits on the order of a few degrees K only. A careful examination of mesonet time series data (c.f. Fig. 5.7) also provides information on the temperature and moisture fluctuations in the part of the storm that passes over a given fixed station, which also suggest relatively small temperature deficits in the forward flank region. Taken together, however, these observations are still insufficient to provide a complete three-dimensional storm-scale picture of the extent and strength of the cold pool, which would be needed for detailed verification of model forecasts. Nevertheless, the evidence is sufficient to rule out in the observed storm the kind of extensive, strong, cold pools produced by *250mMY1A*. In comparison, the cold pool of *250mMY3* is the weakest, and appears to be most realistic, with θ_e deficits on the order of 1 degree K. The cold pools produced by the two-moment schemes (*250mMY2* and *250mMY2DA*), while still appearing too strong, are much weaker than that of *250mMY1A*, which shows large areas of θ_e deficits of 20 degrees K or greater in the hook echo region. The former is much more consistent with the available observational information.

Finally, the reflectivity structure is generally improved in the MM runs, particularly in the forward flank region, with both the SM runs displaying forward flank precipitation regions that are too small compared to the observations (Fig. 6.6b,c). This result was also seen in the idealized simulations of Chapter 5, and was explained as being at least partially due to the presence of parameterized size-sorting in the MM runs, which is absent in the SM runs.

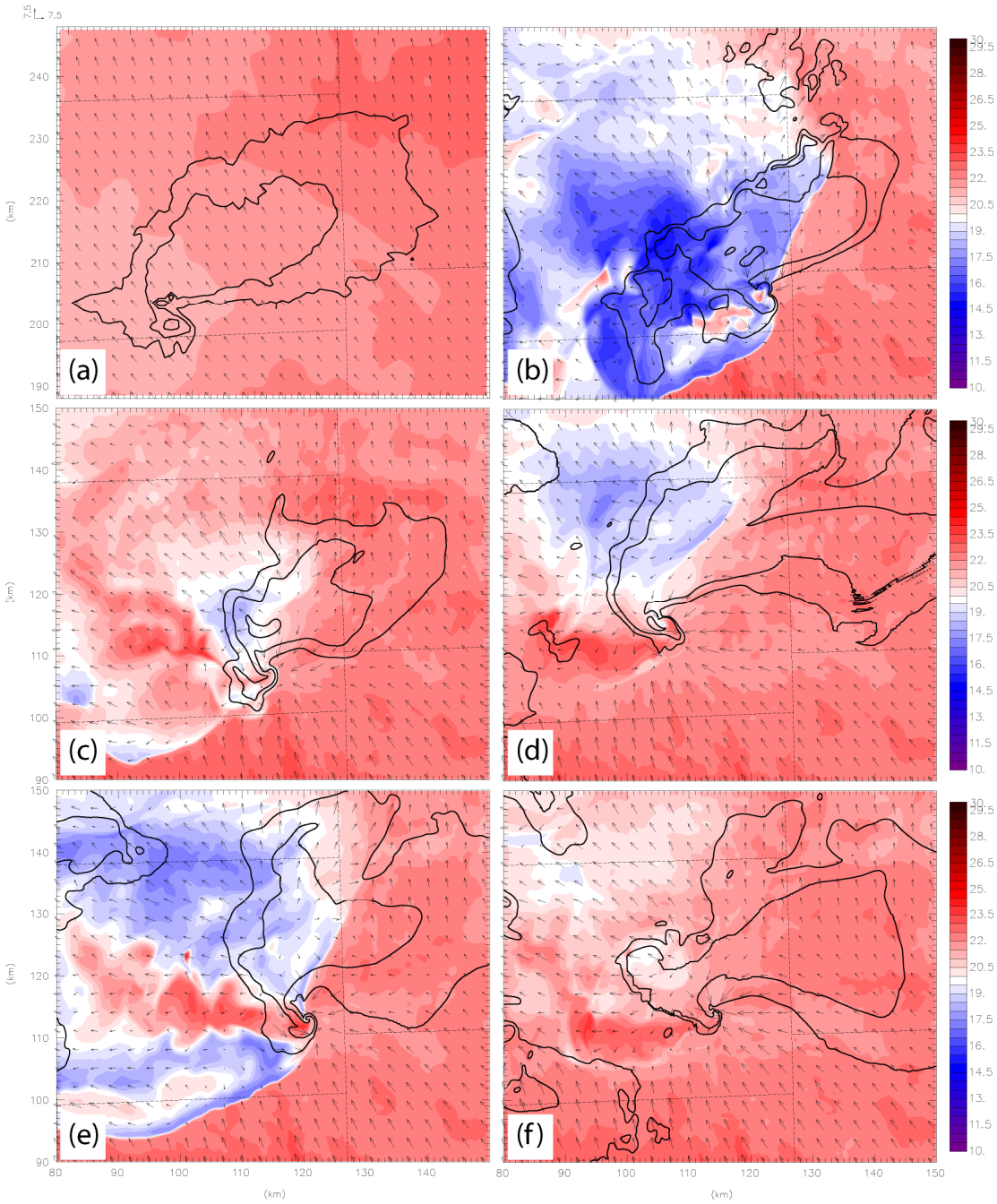

Fig. 6.6. Surface temperature (C°, color fill), radar reflectivity (black contours, 20 dbZ increment), and wind vectors (plotted every 3 km, scale at upper-left) for a) 3DVAR analysis at 0030 UTC (reflectivity is observed from KTLX), and the 1.5 h forecast valid at 0030 UTC for b) *250mMY1A*, c) *250mMY1B*, d) *250mMY2*, e) *250mMY2DA*, and f) *250mMY3*.

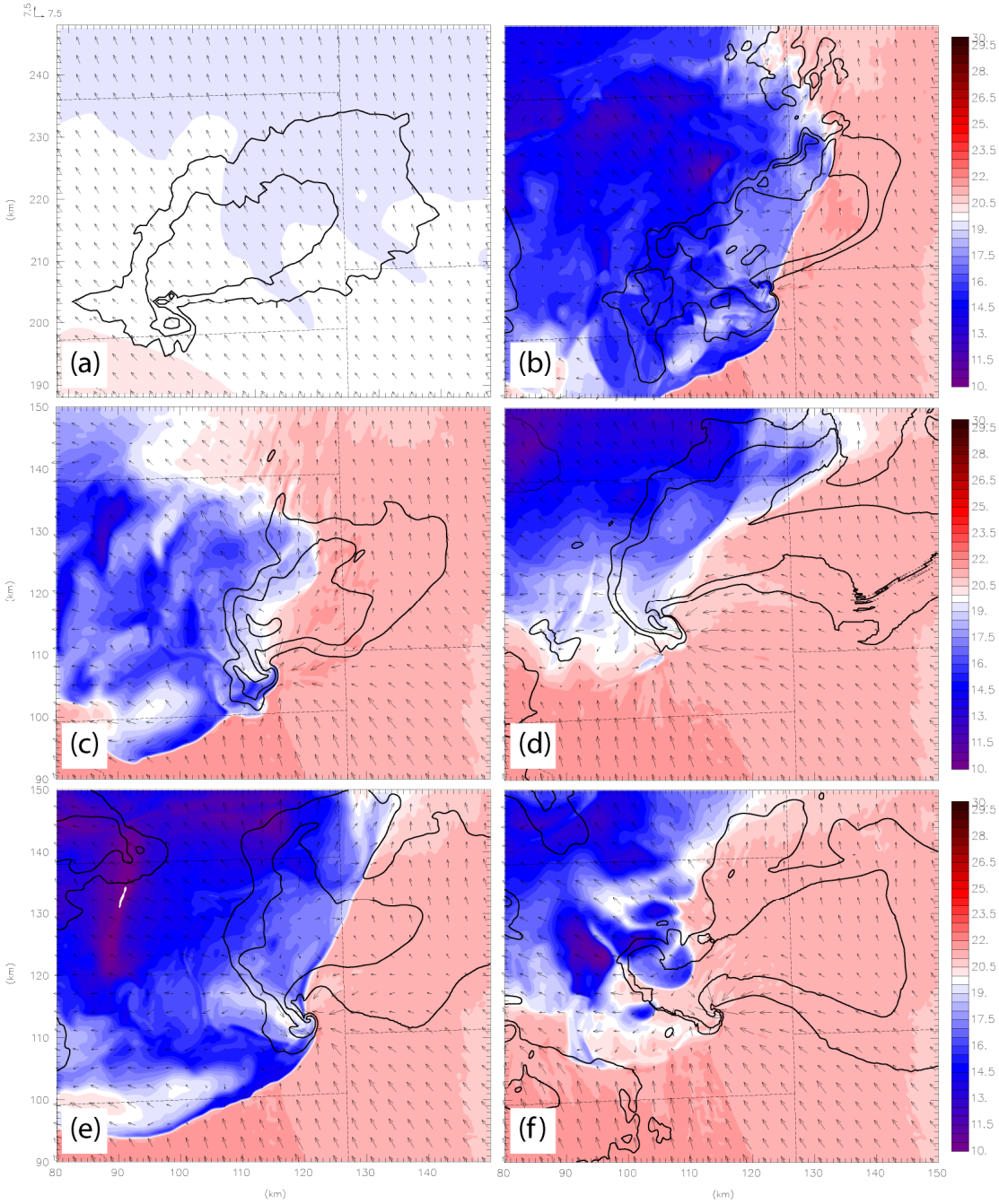

Fig. 6.7. As in Fig. 6.6 except that surface dewpoint temperature is plotted in place of temperature (color fill).

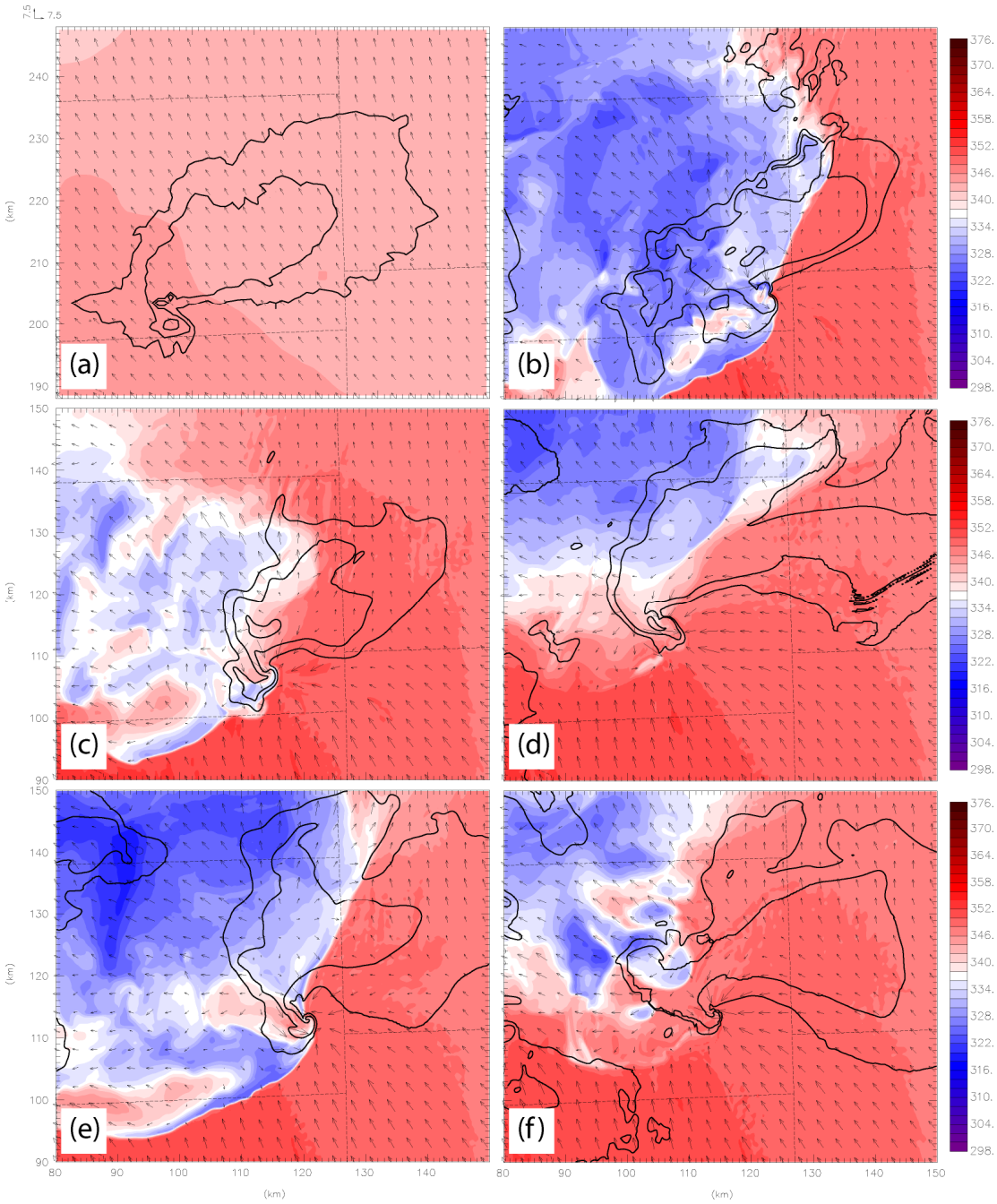

Fig. 6.8. As in Fig. 6.6 except that surface equivalent potential temperature is plotted in place of temperature (color fill).

6.4.2 Budget analysis

In this section, we present a microphysics budget analysis similar to that found in Chapter 5; the results are shown in Fig. 6.9. The same criteria for defining the low-level downdraft region are used here. For these 250-m real-data simulations, however, the budgeting calculations were confined to a 60 km by 60 km fixed squared box focused on storm A, which traverses from near the southwest corner of the box to the northeast during the budgeting period. The budgets were calculated over a 30-min time window from 0000-0030 UTC (from 4500 s to 6300 s forecast times). During this period, the modeled storm A was in a mature quasi-steady stage and was also experiencing minimal interference from another, spurious storm cell trailing it to the west, so the budget calculations are representative of the downdrafts of storm A in each of the simulations. We note that the 60 km by 60 km budget calculation box is similar in size as the computational domain of the 250-m idealized simulations (64 km on a side) reported in Chapter 5, but that in that case, the storm remain relatively centered in the domain due to the storm motion being subtracted from the base-state sounding.

In comparing these budgets with those of the idealized 250-m simulations in Chapter 5, several differences are evident. First, the total magnitude of cooling for each real-data simulation is several times larger than the idealized counterparts. One possible reason for this is that the storms in the real-data case were significantly more intense than in the idealized case, with maximum updraft velocities on the order of 80 m s^{-1} (not shown), as opposed to the 50-60 m s^{-1} displayed by the idealized storms at

250-m resolution (c.f. Fig. 5.18). This should have resulted in more active microphysical processes associated with updrafts and downdrafts, contributing to overall larger microphysical cooling (and heating) rates. This also may explain the larger extent of the surface outflow, particularly to the NW of the storm cores, in the real-data cases.

It is more instructive for our purposes to consider the relative magnitudes of cooling across the real-data simulations. Overall, the same trend in reduced evaporation of rain in the MM simulations is also seen in the real-data simulations. However, the real-data MM runs actually show larger magnitudes of melting hail than the SM runs, opposite to that seen in the idealized simulations. Much of the cooling from this melting, however, is offset by heating due to collection of rain, so that the total effect is comparable to that in the SM runs. However, the relative difference in magnitude of total cooling between the MY1A run and the MM runs are much less pronounced in the real-data case than in the idealized case. It can also be seen that the MY1B simulation has by far the smallest amounts of cooling in the downdrafts of all the simulations, which may be partially due to the relatively smaller size of the storm in this run as compared to the other runs, but also reflects the globally reduced N_{0r} in this run.

In general, our budget analysis still shows rain evaporative cooling and hail melting as the two largest sources of cooling in the downdraft regions, and they are primarily responsible for the large differences in the cold pool extent and intensity when different microphysics schemes are used. The largest difference between MY1A and MY3 is in rain evaporative cooling. The relatively smaller differences

among the schemes may be because the drop size distributions modeled by the MM schemes in this real data cases are closer to that of the SM scheme than in the idealized experiments. There are certainly nonlinear effects that affect the general storm morphology, which complicates the interpretation.

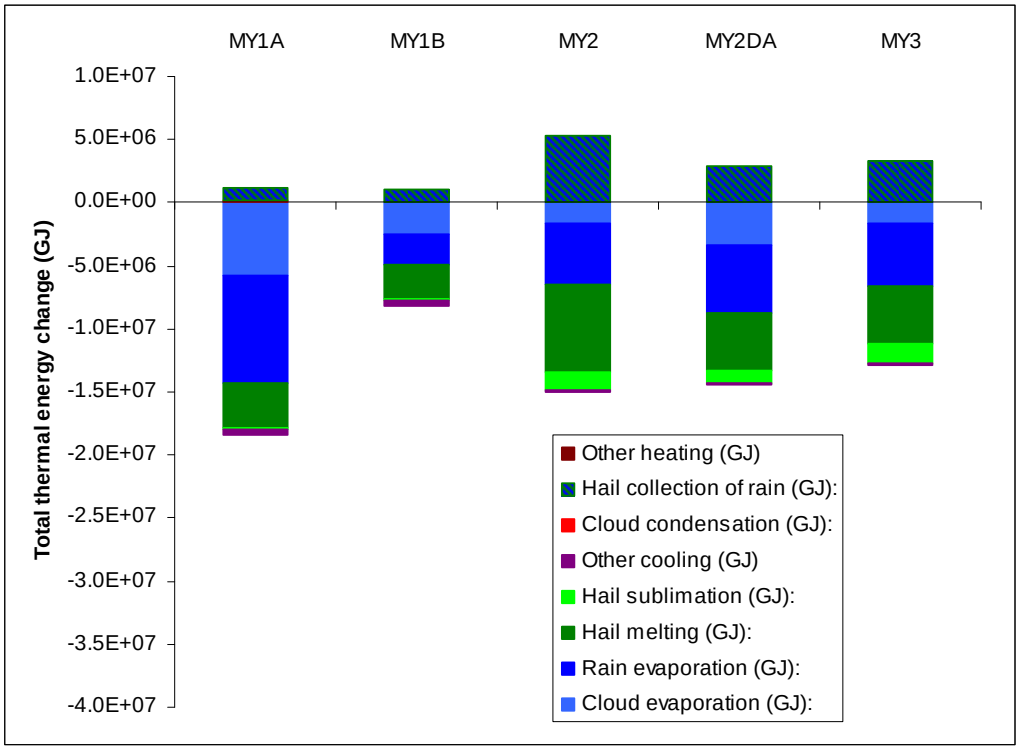

Fig. 6.9. Bulk thermal energy change ($c_p \Delta T$) from microphysical processes in the low-level downdraft (defined as all grid boxes below 4 km AGL with w < 0.5 m s^{-1}) between 4500 s and 6300 s for each of the 250-m (real-data) simulations.

6.4.3 Tornado-strength vortices

Although a horizontal grid-spacing of 250 m may be considered too coarse to resolve tornado-scale circulations well, nevertheless, intense low-level vortices developed in several of the forecast experiments, which can likely be at least identified with the tornadoes' parent circulations, even if the core structure of the actual tornado is not resolved (see, e.g., the discussion in Klemp and Rotunno 1983).

For the purposes of this study, we consider a vortex a tornado if it is clearly associated with the hook echo region of the simulated storm, exhibits a concentrated area of vertical vorticity at the surface, and has a maximum surface wind speed of 30 m s^{-1} or greater, which is close to the lower limit of the EF0 category (~29 m s^{-1}) on the enhanced Fujita scale (McDonald and Mehta 2006). This latter criterion is also similar to the 32 m s^{-1} wind speed threshold, which correspond to the lower limit of an F1 tornado on the original Fujita (1971) scale, as used by Wicker and Wilhelmson (1995). However, surface vortices that are weaker than the tornadoes as defined above (that is with surface wind speeds that never exceed 30 m s^{1}) are also present in the hook echo regions in the simulations. In the following discussions, we will refer to these vortices as "weak tornadoes", as they are in the F0 or weaker category. This distinction serves to distinguish well between many of the weak, short-lived vortices in these experiments, especially those that occur in *250mMY1A*.

Fig. 6.10 shows the time series of maximum surface vorticity and wind speed for each of the 250 m runs. Also shown in the figure are the start and end times of the observed F5 tornado A9, and the wind speed thresholds of the EF-scale as horizontal dotted lines. In all cases except *250mMY1A*, an intense vortex develops, with *250mMY3* showing the earliest development (around 4500 s), and *250mMY2* having the strongest vortex, with surface wind speeds briefly reaching above EF4 intensity. As can be seen, the forecast tornado in each case except for *250mMY3* developed significantly later than the observed tornado and continued past the time of the dissipation time of observed tornado in each case.

Fig. 6.11 shows the surface wind swaths for each of the 250 m runs. The wind swaths were computed from the maximum surface wind speed (computed at the 1-min data intervals) experienced at each surface grid point over the entire 8100 s model forecast, at 1-min intervals. The observed F5 tornado track is also shown in Fig. 6.11a for reference. Of all the runs, *250mMY3* shows a track that is most consistent with the length and position of the observed tornado, and even has it developing near the time of the observed tornado touchdown, around 2700 s (2330 UTC), though the track is shifted overall north approximately 5-10 km from the observed track. Evidence of cyclic behavior is seen in *250mMY2*, where an additional tornadic wind swath is seen toward the end of the track. In all cases, the tornado-strength vortex was still ongoing at the end of the forecast period, but due to computational resource reasons the forecast time was not extended beyond 8100 s (0100 UTC).

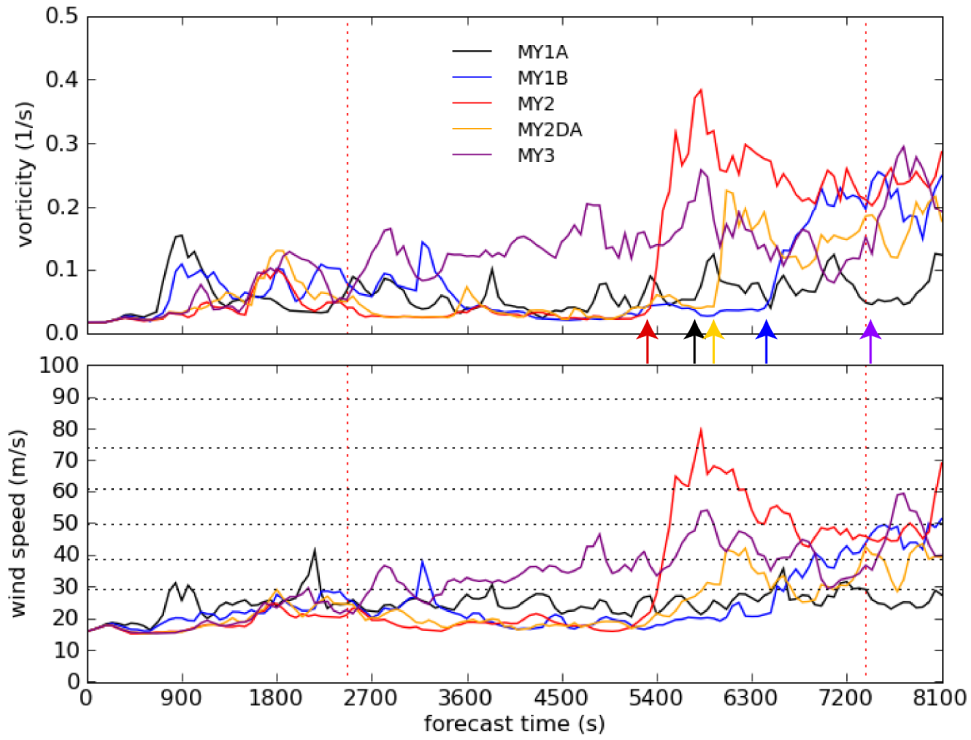

Fig. 6.10. Maximum surface a) vorticity and b) wind speed versus time, for the 250-m runs. The vertical dotted red lines delineate the start and end times of the observed F5 tornado (2326-0048 UTC). The horizontal dotted lines in b) indicate the thresholds of the EF-scale, from EF0 through EF5. Arrows in (a) denote the approximate tornadogenesis (or tornado intensification in *250mMY3*) times investigated in the trajectory analysis.

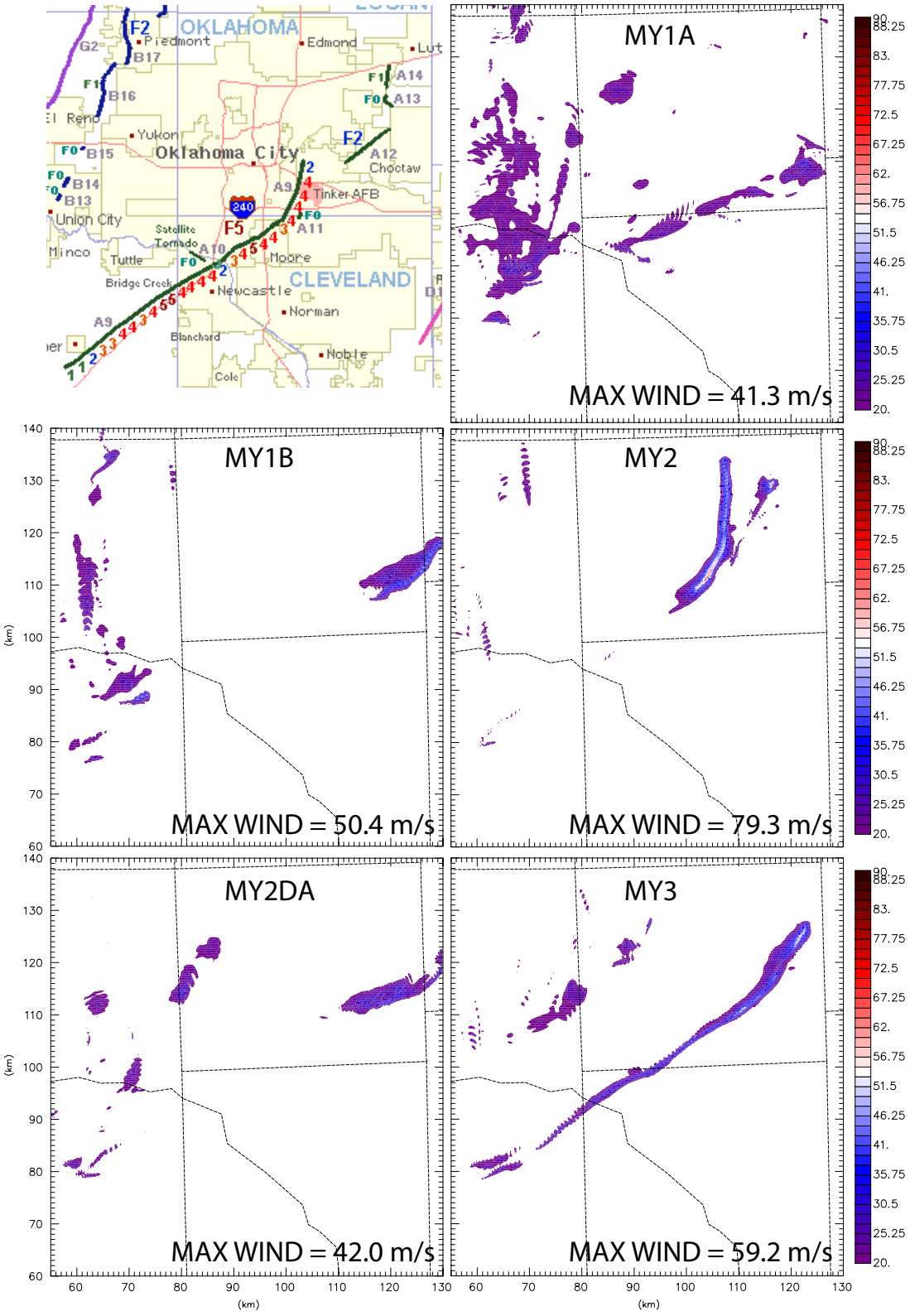

Fig. 6.11. Surface wind swaths for the 250 m runs.

As mentioned previously, observations of surface conditions in the RFD near tornadoes have consistently indicated a strong correlation between significant tornadoes and relatively warm surface air in the RFD (Markowski 2002, M02, MSR02). Idealized numerical simulations conducted by Markowski et al. (2003, hereafter MSR03) in which rain-induced downdrafts were imposed in varying environmental thermodynamic conditions leading to different amounts of evaporational cooling corroborated these observations. Simulated tornadoes were significantly weaker when the downdraft air was more negatively buoyant (i.e., when containing θ_v deficits 5-6 K or more near the tornado), as opposed to when the downdraft air contained smaller θ_v deficits (on the order of 2-3 K near the tornado). The downdrafts were more negatively buoyant when the imposed well-mixed boundary layer air was drier and deeper, due to enhanced evaporative cooling (MSR03).

In the current study, there is a distinct tendency for the tornado development, intensity, and longevity to be suppressed (enhanced) when the choice of microphysics scheme and/or their parameters lead to a stronger (weaker) cold pool, especially in the hook echo/RFD region of the storm (compare Fig. 6.8 with Fig. 6.11). These results are thus very consistent with the work of Markowski discussed above. It is of interest to examine in more detail the thermodynamic properties of the near-tornado surface air in the RFD, and the time history of this air, to determine the physical processes that are important in each case. We seek to accomplish this goal by examining the terms in the vertical momentum equation, with attention to the buoyancy and

perturbation pressure gradient terms, and by examining rain and hail DSD-related parameters in the hook echo/RFD region. These are discussed next.

6.4.4 Near-tornado RFD analysis

6.4.4.1 Warm RFD surges and trajectory analyses

Examination of animations[2] of the surface thermodynamic fields as shown in Figs. 6.6-6.8 indicates that in all experiments, in the ~15-20 min leading up to tornadogenesis (defined as when surface wind speed shown in Fig. 6.10 exceeds 30 m s^{-1}), relatively warm and moist divergent outflow in the RFD region forms behind the hook echo and surges eastward, and is caught up in the convergent cyclonic rotation near the tip of the hook echo that subsequently reaches at least weak tornadic intensity (using the criteria defined above). Interestingly, this occurs even in *250mMY1A*, *250mMY1B*, and *250mMY2DA*, in which relatively cold outflow is found to dominate the entire hook echo region prior to the development of these "warm RFD pockets". Only after the warm RFD surge reaches the convergent cyclonic flow at the tip of the hook echo, does tornadogenesis commence, suggesting an important causal link between the warm RFD surge and tornadogenesis. In *250mMY2* and *250mMY3*, the hook echo region is dominated by relatively warm air through most of the simulation period, and, accordingly, tornadogenesis occurs earlier, reaches a greater maximum intensity and lasts longer. Fig. 6.12 shows snapshots of this evolution of the warm RFD surge just before (5 min, left column) and just after (right column) the time of tornadogenesis (see arrows in Fig. 6.10) for each of the 250-m

[2] These and animations of other fields can be found in JavaScript form on the author's research web site at http://www.caps.ou.edu/~ddawson/03May1999/

experiments (in *250mMY3*, the tornado was in progress throughout this time, but the figure shows a period of significant intensification of the tornado, near the end of the simulation between 0050 and 0055 UTC).

To examine the source of the warm RFD air that enters the developing tornadoes, we calculate parcel trajectories that are initialized near the surface (at a height of 10 m AGL, roughly the height of the first scalar point above ground) in the RFD immediately west of the developing tornado. In each case, 9 trajectories are initialized, one at a chosen point, and 8 along a horizontal circle of 250 m radius centered at this point. The trajectories are integrated backward in time for 15 min to determine the parcel origins, and forward in time for 5 min to determine if they reach the tornado. The trajectories were integrated using temporally and spatially interpolated wind output at 1-min intervals, with a 5 s time step. These trajectories are plotted in Fig. 6.12 for each run, with the trajectories colored by height AGL. In *250mMY1A*, the trajectories that enter the developing tornado emanate from the cold pool (Fig. 6.12a,b) behind the gust front, whereas, in other runs (Fig. 6.12c-j), the trajectories mainly emanate from inside the forward flank reflectivity region to the northeast of the developing tornado, circulate around the northwest side of the low-level mesocyclone, and descend in a shallow layer (< 500 m) in the RFD before reaching the tornado at the surface.

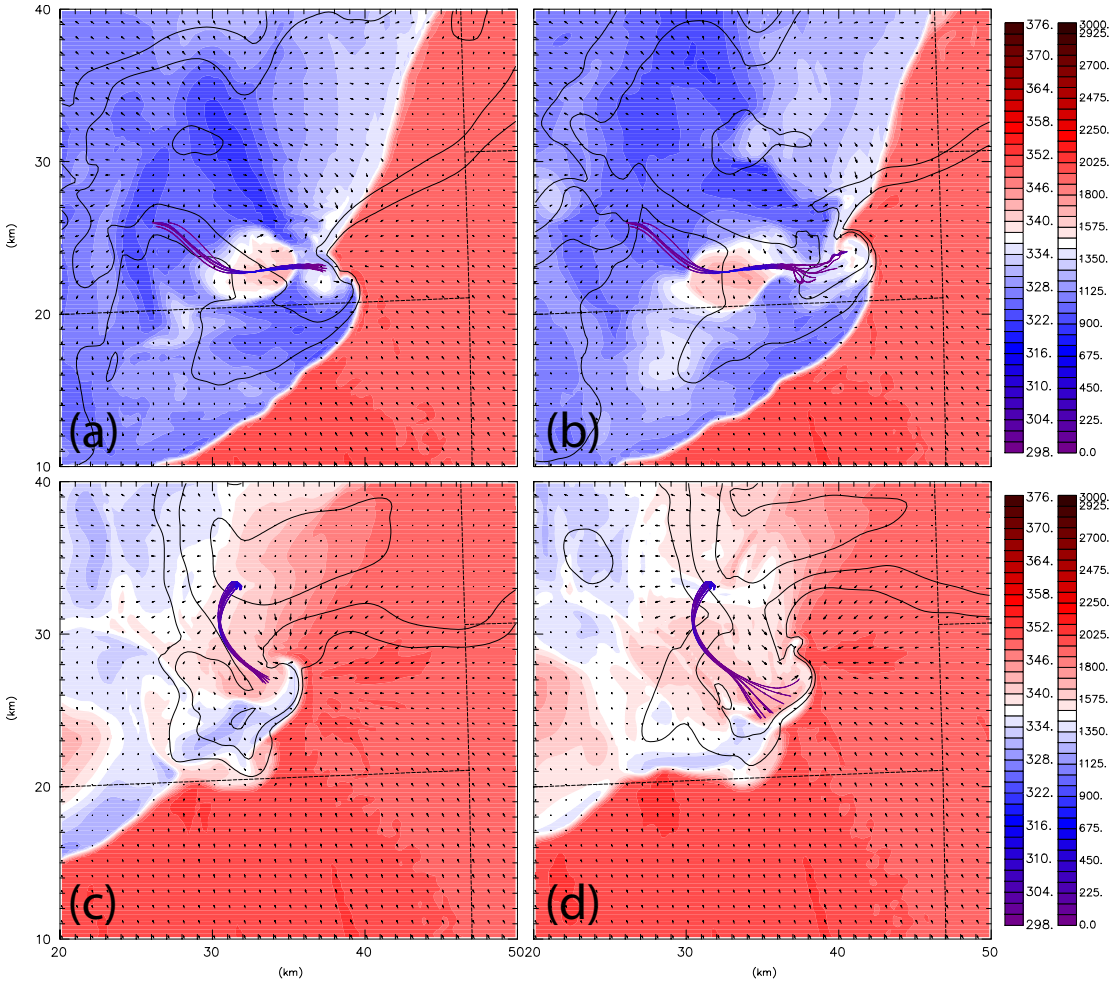

Fig. 6.12. Surface equivalent potential temperature (color fill), radar reflectivity (black contours, 20 dbZ increment), and wind vectors (plotted every 3 km, scale at upper-left) for a) *250mMY1A* at 0020 UTC, b) *250mMY1A* at 0025 UTC, c) *250mMY1B* at 0030 UTC, d) *250mMY1B* at 0035 UTC, e) *250mMY2* at 0015 UTC, f) *250mMY2* at 0020 UTC, g) *250mMY2DA* at 0020 UTC, h) *250mMY2DA* at 0025 UTC, i) *250mMY3* at 0050 UTC, j) *250mMY3* at 0055 UTC. In each panel, trajectories are (paths are ground relative) plotted up to the time of that panel and are colored by height AGL (colorbar at right). The left column times correspond to the initialization times of the trajectories, while the right column are 5 minutes later, when at least some of the trajectories in the RFD enter the developing tornado.

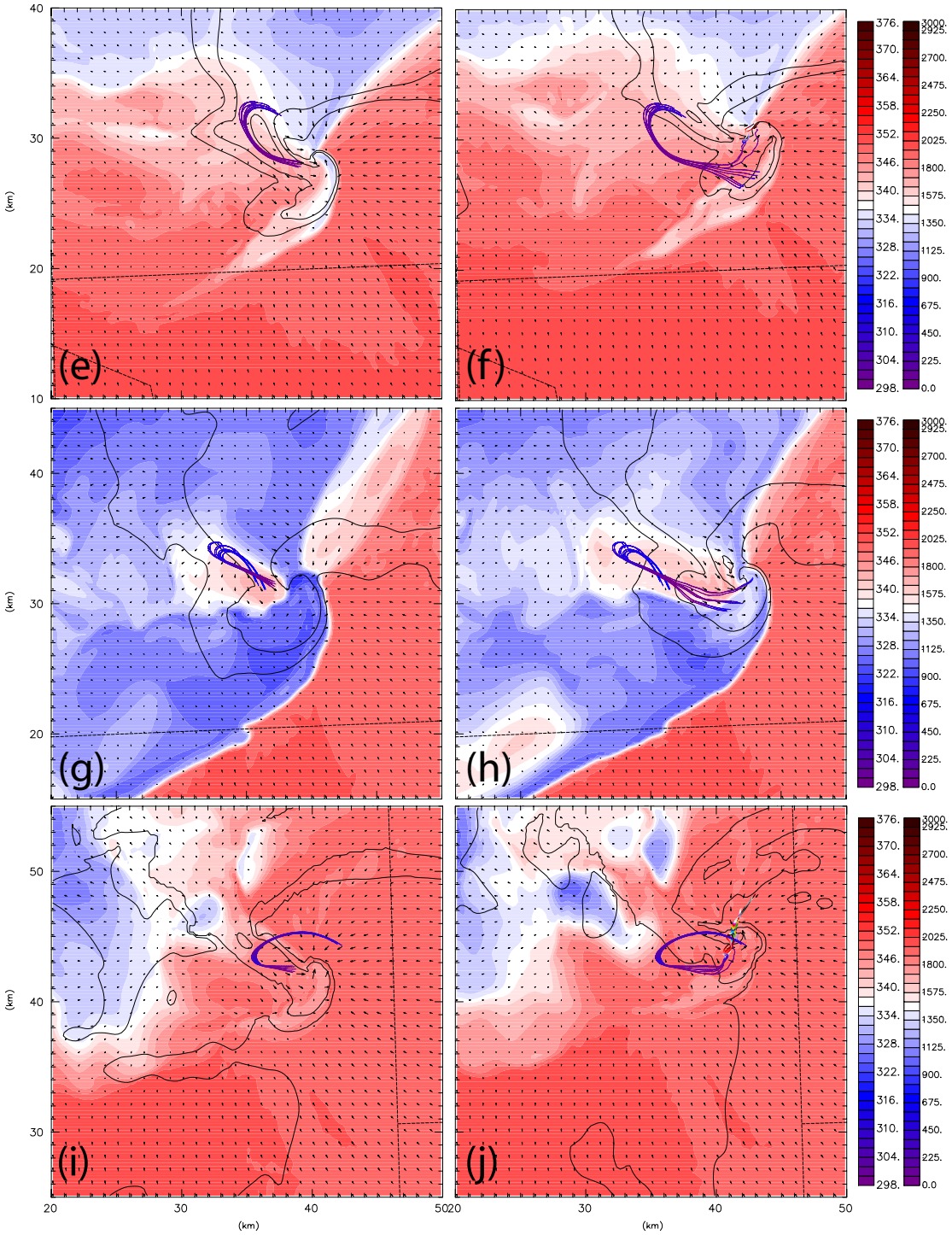

Fig. 6.12. Continued.

6.4.4.2 Analysis of vertical momentum equation and thermodynamics along trajectories

To examine forcing important for the development of the RFD surges, we consider the inviscid vertical momentum equation (neglecting frictional and turbulent effects):

$$\frac{\partial w}{\partial t} = -\mathbf{v} \cdot \nabla w - \frac{1}{\overline{\rho}} \frac{\partial p'}{\partial z} + B, \tag{13}$$

where w is the vertical velocity, $\mathbf{v}$ the 3D velocity vector, $\overline{\rho}$ is a "reference state" density, p' a perturbation pressure from the reference state in hydrostatic balance with $\overline{\rho}$, and B the total buoyancy that includes the effects of temperature, water vapor, liquid and solid water, and pressure perturbations.

Thus (13) is a form of the anelastic vertical equation of motion in height coordinates. Previous numerical studies of supercell dynamics have used anelastic or even simpler Boussinesq (which treats $\overline{\rho}$ as a constant) forms of the dynamic equations for diagnostic purposes, without loss of substance over using the fully compressible equations (see, e.g., Rotunno and Klemp 1982; Klemp and Rotunno 1983; Rotunno and Klemp 1985). The three terms on the RHS of (13) are, respectively, the 3D advection of vertical velocity, the vertical perturbation pressure gradient force (VPPGF), and the buoyancy force. The total buoyancy in turn can be written as:

$$B = -g\frac{\rho'}{\overline{\rho}} = g\left[\frac{\theta'}{\overline{\theta}} - \frac{c_v}{c_p}\frac{p'}{\overline{p}} + \frac{q_v'}{\left(\frac{R_d}{R_v} + \overline{q_v}\right)} - \frac{q_v' + q_{li}}{1 + \overline{q_v}}\right], \tag{14}$$

where the primed quantities represent departures from a reference state (denoted by the barred quantities) for density ρ, pressure p, water vapor mixing ratio q_v, and total liquid plus ice water mixing ratio q_{li}, c_v and c_p are the specific heats at constant volume and pressure for dry air, respectively, and R_d and R_v are the gas constants for dry air and water vapor, respectively. The terms within the brackets, from left to right, are the contributions to buoyancy from (potential) temperature, pressure, and water vapor perturbations, and liquid and solid water loading.

It remains to define the "reference state" or "base state". As pointed out by Doswell and Markowski (2004), any definition of a base state is necessarily arbitrary, and affects the relative partitioning of the VPPGF between that due to the buoyancy itself, and that due to dynamical contributions, which are a function of the flow field only. Unlike in Klemp and Rotunno (1983), for simplicity, we do not decompose p' into dynamic and buoyancy-induced components, which requires the solution and decomposition of a diagnostic elliptic pressure equation. Instead, we define a time-varying, horizontally inhomogeneous, hydrostatic base state by filtering the model potential temperature θ and water vapor specific humidity q_v using a 2D horizontal moving average filter with a width of 10 km in both directions. The 10 km chosen here is large enough for the filtered flow to be mostly hydrostatic; at the same time it is small enough so that the perturbations from this filtered state reflect the buoyancy effect relative to a parcel's immediate surroundings. Tests indicated that the perturbation fields were found to be relatively insensitive to reasonable variations in the filter width (± 5 km).

The filtered pressure field is then found by integrating the hydrostatic equation vertically, and these filtered variables define the reference or base state. Since the ARPS grid is terrain-following in the general case, we first interpolate the model fields to an intermediate Cartesian grid with high vertical resolution that encompasses the entire span of the given ARPS domain. For points that are below ground on the intermediate grid, a zero-vertical-gradient assumption is used for θ and q_v, and p is found by integrating the hydrostatic equation downward. The horizontal filtering is then performed on this intermediate grid, the pressure field is found by integrating the hydrostatic equation upward to the top of the grid, before finally interpolating the resulting filtered θ, q_v and p back to the ARPS grid. Perturbation quantities are then derived by subtracting the filtered field from the total field for each variable. Thus, the perturbation quantities p', θ', and q_v' represent deviations from a local, smoothly varying, hydrostatic "base state" that is time-dependent. In this manner, by considering perturbations as departures from the immediate surroundings (represented by the magnitude of the horizontal filtered variable at a given point), the VPPGF and buoyancy terms in (13) are partitioned in such a way that most of the VPPGF represents the dynamic contribution or little of it is in hydrostatic balance with B. This approach is similar in spirit to that taken by Davies-Jones (2003) in which he defined an "effective buoyancy" that represents a weighted sum of the relative buoyancies in the immediate neighborhood of a given point, that itself was independent of the specification of the base state. In his formulation, the VPPGF term then contains only the dynamic effects (i.e., is dependent only on the flow field). In the future, a more robust examination of the terms in (13) will be performed by

explicitly calculating the fields from the formulas in Davies-Jones (2003) or through the decomposition of the pressure field through the method of Klemp and Rotunno (1983).

The following series of figures shows time-height (TH) contour plots along selected trajectories plotted in Fig. 6.12 (the trajectory chosen for each run is one that enters the tornado in each figure). Table 6.2 summarizes the trajectory start and end times for each run. At the horizontal location (x, y) of each trajectory point at 60 s intervals, model quantities at levels from the surface to 4 km height are interpolated along the coordinate surfaces to this (x, y) location, forming a column of interpolated quantities through this (x, y) location. These columns along the trajectory form the vertical 'curtains' that pass through the trajectories, and are plotted in Fig. 6.13 through Fig. 6.17 for individual experiments as 'time-height' cross sections. The height of the trajectory at each time is also overlaid on each of the panels. The goal of this process is to determine the importance of the forcing terms in (13) along and in the vicinity of the trajectories. We point out here that while efforts were made to pick representative trajectories, the actual trajectories shown here may not be the most representative.

Table 6.2. The start and end times of the trajectories chosen for detailed along-trajectory analysis for the 250-m real-data experiments

Experiment	Start time (UTC/forecast time)	Specification time (UTC/forecast time)	End time (UTC/forecast time)
250mMY1A	0005/4800 s	0020/5400 s	0025/6000 s
250mMY1B	0015/5400 s	0030/6300 s	0035/6600 s
250mMY2	0000/4500 s	0015/5400 s	0020/5700 s
250mMY2DA	0005/4800 s	0020/5700 s	0025/6000 s
250mMY3	0035/6600 s	0050/7500 s	0055/7800 s

Figs. 6.13-6.17 show 4-panel along-trajectory TH plots of w, θ', q_v', p' for each of the 250-m runs. Figs. 6.19-23 show plots of the forcing terms in the vertical momentum equation (except for advection) for the same trajectories, and Figs. 24-28 show the cloud, rain, and hail mixing ratios and their respective cooling rates due to evaporation and melting.

In *250mMY1A*, the parcel begins in the cold-pool northwest of the developing tornado, in negatively-buoyant near-surface air (Fig. 6.13b). At around 5100 s, the parcel begins to rise under the influence of an upward-directed VPPGF (Fig. 6.18c) underneath a strengthening vortex aloft, (Fig. 6.13a), but quickly falls again as the parcel becomes strongly negatively-buoyant (Fig. 6.18a). As the parcel approaches the developing tornado, it experiences only slight upward accelerations due the surface convergence at the tip of the hook echo (c.f. Fig. 6.12a,b), and only a broad, weak vortex forms. Inside the vortex itself, both negative buoyancy and a downward-directed VPPGF (presumably due to stronger rotation near the surface), contribute to

downward acceleration (Fig. 6.18b,c,e). Of note is the fact that vertical velocities above the vortex in the 1.5-3.5 km layer are relatively weak, with a downdraft present between 1.5 and 2.0 km. Examination of the vertical vorticity distribution with height during this period (not shown), indicate that the vortex is tilted to the NW with height, with the surface vortex displaced ~ 1 km to the SE of the vortex in the low-to-mid levels (2-4 km AGL). This decoupling continues at later times (see Fig. 6.23a), and the surface vortex rapidly weakens. It thus appears that both the negatively-buoyant near-surface air and lack of a strong vertical connection to the low-to-mid-level mesocyclone contribute to the lack of significant intensification of the tornado in this case, which is consistent with the results of Snook and Xue (2008). It is also of note that the warm RFD surge seen in Fig. 6.12a,b occurs after this trajectory has already entered the tornado.

In *250mMY1B*, a similar evolution occurs, except that the parcel is initially slightly less negatively-buoyant (Fig. 6.14b). The vortex that forms at the end of the trajectory integration period (6600 s) is stronger than in *250mMY1A* and is also located underneath a stronger updraft above 1.5 km that is associated with the low-level mesocyclone. Though it is not evident from the TH plots, the most significant difference between *250mMY1B* and *250mMY1A* appears to be that the region of maximum surface convergence and associated upward VPPGF (Fig. 6.19c) remains closer to the position of the low-level mesocyclone during this and later times (Fig. 6.23b), and this is due at least partially to the cold outflow being weaker in this run. Accordingly, the tornado in *250mMY1B* continues to intensify after the time window

considered here and lasts through the rest of the forecast period, reaching wind speeds of 50.4 m s^{-1} at the end of the forecast period (1800 s, c.f. Fig. 6.10b, Fig. 6.11c).

In *250mMY2*, the parcel is slightly negatively-buoyant initially, but becomes nearly neutrally-buoyant (Fig. 6.15b) through most of its slow descent as it approaches the tornado, curving cyclonically from the inflow region within the forward flank (c.f. Fig. 6.12e,f). The depth of descent during the whole integration period is shallow (~400m), and total forcing for vertical acceleration is near zero (Fig. 6.20e). Upon reaching the tornado (~5550 s), the trajectory rapidly ascends due to forcing for upward ascent mainly from the upward VPPGF and perturbation pressure buoyancy forcing (Fig. 6.20c,f). Thermal buoyancy at this time is negative (Fig. 6.20b). As in *250mMY1B*, the surface vortex maintains a strong connection with the low-level mesocyclone and updraft after this time (Fig. 6.23c).

In *250mMY2da*, the parcel undergoes a somewhat different evolution than in the previously-discussed runs. Similar to *250mMY2*, the parcel begins in the forward flank baroclinic zone (Fig. 6.12g,h) to the NE of the developing tornado. In this case, however, the parcel becomes entrained in a downdraft that appears to be strongly-forced by the negative VPPGF just above the parcel trajectory between 5400 and 5700 s (Fig. 6.21c). During this descent, the parcel becomes thermally positively buoyant, which corresponds with the relative high θ_e pocket of air seen to the west of the developing tornado in Fig. 6.12g,h. In this case, as opposed to *250mMY1A*, the warm RFD surge does appear to feed directly into the developing tornado. However, the slightly more negatively-buoyant air in *250mMY2da*, as compared to *250mMY2* (compare Fig. 6.15b with Fig. 6.16c near the end of the time window, and also Fig.

6.12e,f with Fig. 6.12g,h), appears to be suppressing the intensification of the tornado somewhat, at least at this time. At later times (not shown), the low θ_e air seen near the tornado in Fig. 6.12g,h for the *250mMY2DA* run is replaced by higher values more consistent with those seen in *250mMY3* (Fig. 6.12i,j), and the tornado intensifies.

Finally, in *250mMY3*, the thermodynamic conditions along the trajectory before reaching the tornado are characterized by weak θ perturbations (Fig. 6.17b), similar to *250mMY2* and *250mMY2DA*, and the overall evolution is very similar to *250mMY2*. One significant difference is that the air rising in the tornado is thermally neutral or positively buoyant throughout the depth of ascent (Fig. 6.22b), as opposed to all the other runs, where the parcel is thermally negatively buoyant in the low-level (< 1 km) tornado updraft. Also, in both *250mMY2* and *250mMY3*, the rapid increase in rotation induces both a strong downward-directed VPPGF above the surface vortex, but also acts to enhance upward acceleration due to the strong positive pressure buoyancy (Fig. 6.20c,f and Fig. 6.22c,f). Thus, once the vortex becomes established and exhibits strong rotation through a significant depth, the pressure buoyancy effect overwhelms other contributions, positive or negative, to buoyancy.

To summarize, the thermodynamic conditions in the near-tornado RFD air have a significant effect on the subsequent development of the tornado in the 250-m runs. In the runs where significant negative buoyancy is present in the outflow of the RFD (*250mMY1A*, *250mMY1B*, and *250mMY2DA*), the tornado develops more slowly and is weaker (or even dissipates quickly after initial development, as in *250mMY1A*). In contrast, in the runs where the near-surface air in the RFD is only weakly

negatively buoyant (*250mMY2* and *250mMY3*), the tornado develops more quickly and becomes more intense. Warm RFD surges are present in all the runs, but in *250mMY1A* and *250mMY2DA*, they are surrounded by significantly colder air initially. These surges appear to be dynamically-forced by either the increasing low-level rotation in the low-level mesocyclone, or the "blocking effect" aloft of the storm's updraft, and work is ongoing to determine the relative importance of these two potential effects. Tornadogenesis occurs in these runs when the warm RFD surge reaches the convergence zone near the tip of the hook echo, where the outflow meets the low-level inflow. The presence of strong cold outflow in the RFD region appears to suppress tornadogenesis and/or intensification for two main reasons. One is that the negative buoyancy of the near surface air leads to significant downward buoyant force when the air is forcibly lifted by the upward VPPGF caused by the strong convergence at the tip of the hook echo or by strong rotation aloft; the negative buoyancy force acts to limit upward accelerations. This is consistent with Markowski's observations (M02, MSR02) and idealized numerical simulations (Markowski et al. 2003). The other reason is that the location of maximum cyclonic surface convergence is strongly determined by the strength of the outflow. In *250mMY1A* in particular, the cold outflow is strong enough to displace the surface vortex progressively SE of the mid-to-low-level mesocyclone which forms above the cold pool. As such, vertical stretching of surface vorticity is inhibited due to the lack of vertical superposition of the updraft associated with the mesocyclone and the developing surface circulation. This result is consistent with the findings of Snook and Xue (2008).

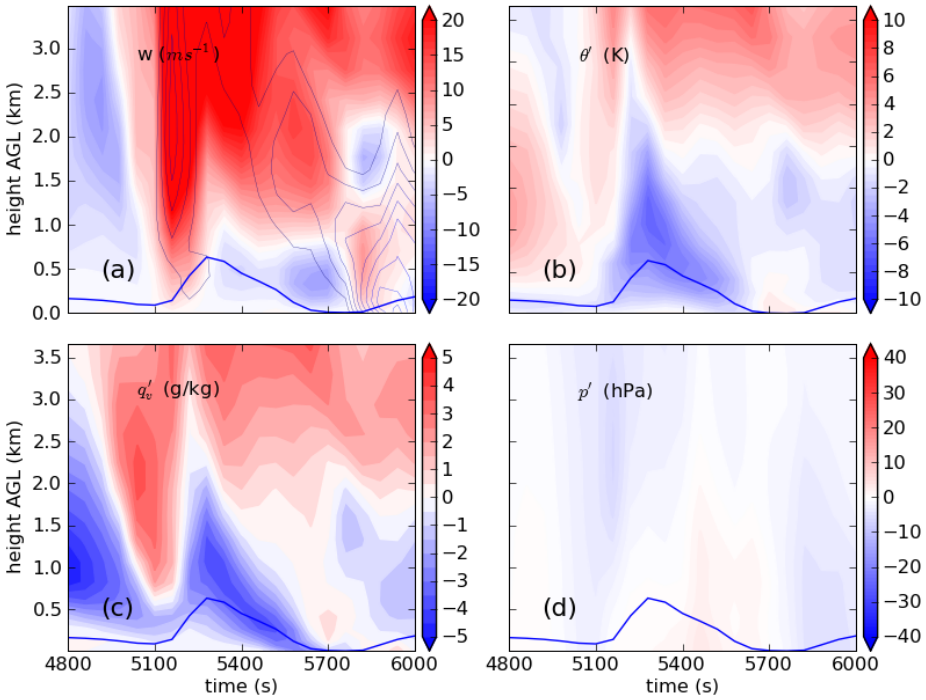

Fig. 6.13. Time-height plots along an RFD trajectory that enters the developing tornado for *250mMY1A*. The blue line in each panel indicates the trajectory height for each time. (a) vertical velocity (m s^{-1} color fill) and vertical vorticity (thin black contours, 0.01 s^{-1} increment, starting at 0.01 s^{-1}), (b) perturbation potential temperature (g kg^{-1}, color fill), (c) perturbation water vapor specific humidity (g kg^{-1}, color fill), and (d) perturbation pressure (g kg^{-1}).

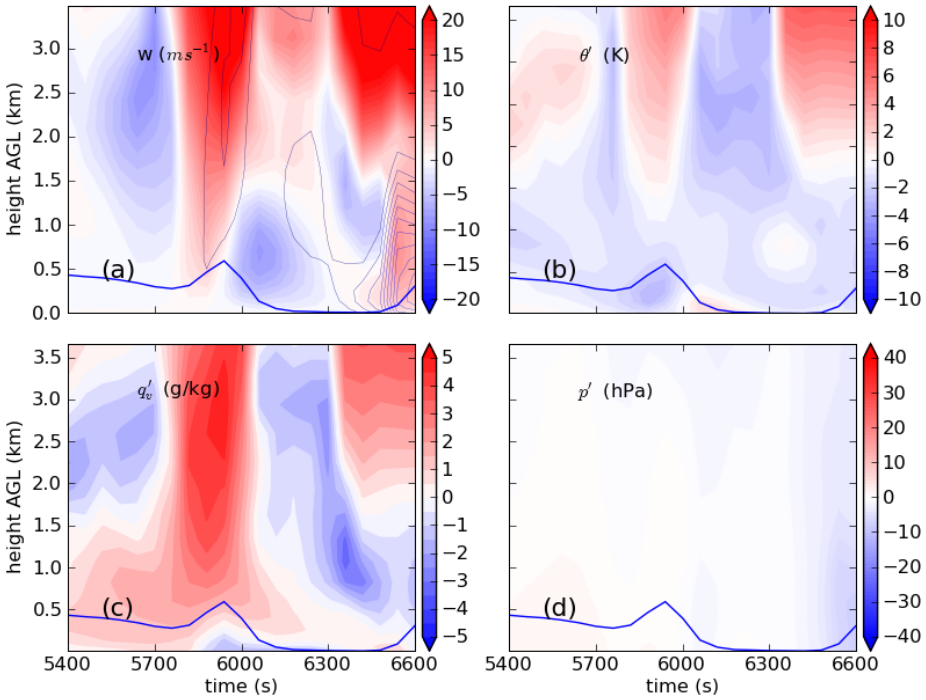

Fig. 6.14. As in Fig. 6.13 but for *250mMY1B*.

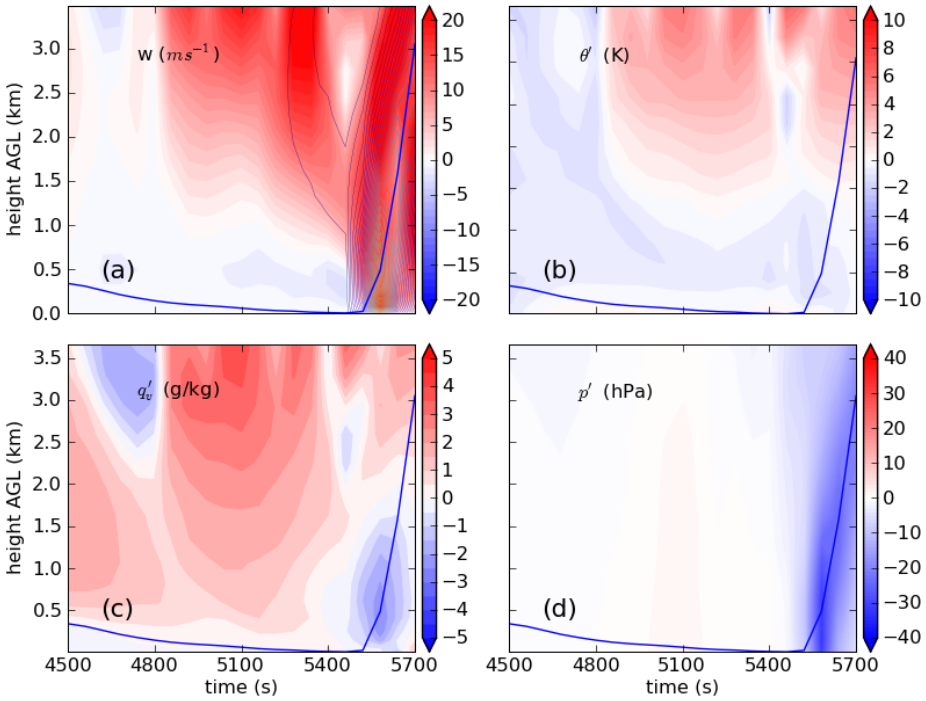

Fig. 6.15. As in Fig. 6.13 but for *250mMY2*.

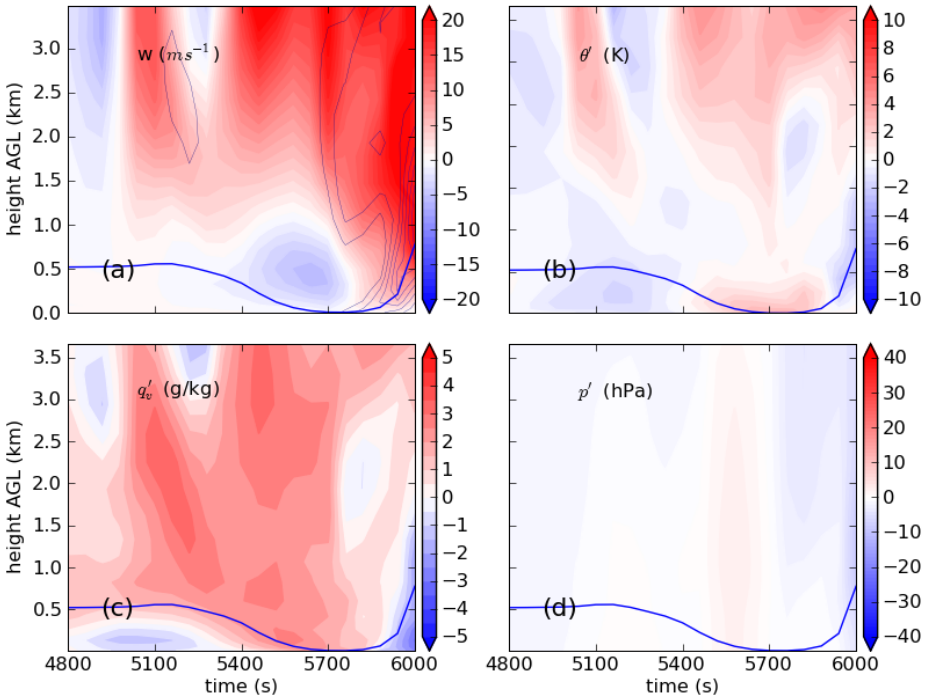

Fig. 6.16. As in Fig. 6.13 but for *250mMY2DA*.

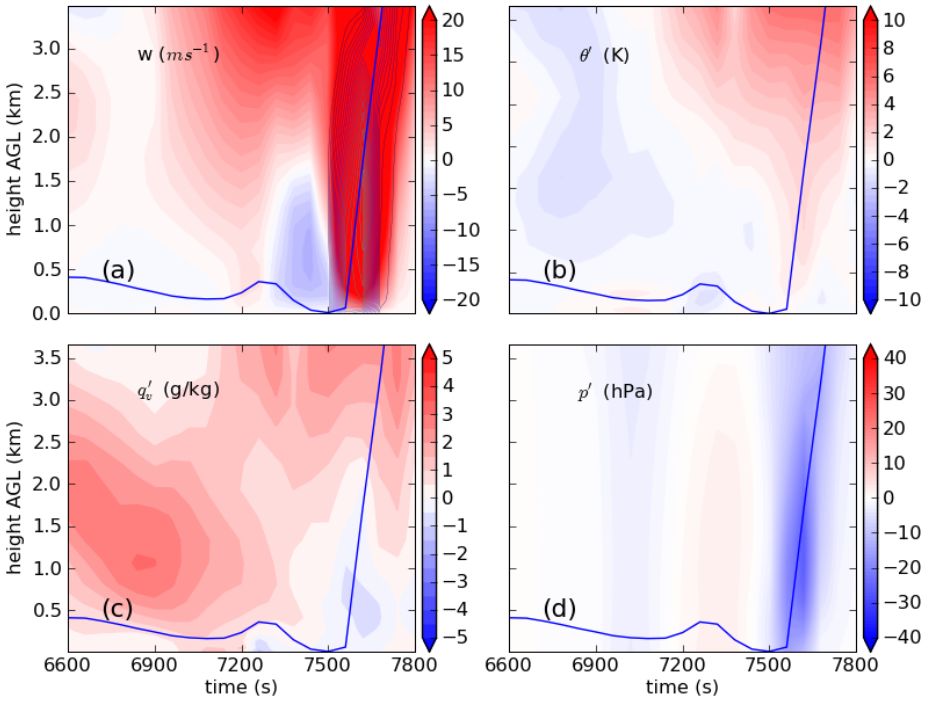

Fig. 6.17. As in Fig. 6.13 but for *250mMY3*.

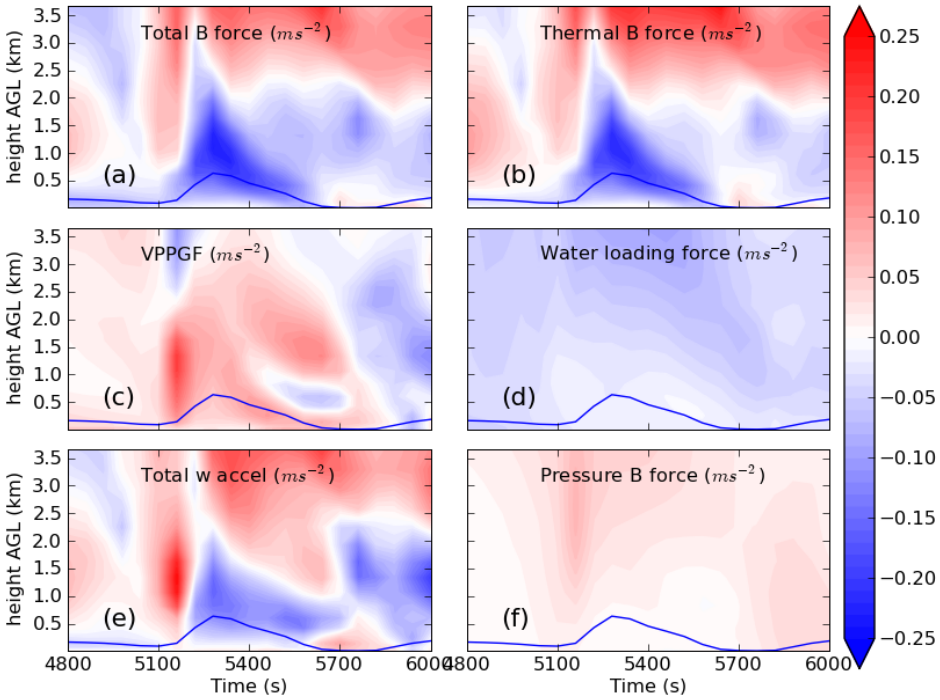

Fig. 6.18. Time-height plots along an RFD trajectory that enters the developing tornado for *250mMY1A*. The blue line in each panel indicates the trajectory height for each time. a) total buoyancy forcing (m s^{-2},color fill), b) thermal buoyancy forcing (m s^{-2},color fill), c) vertical perturbation pressure gradient forcing (m s^{-2},color fill), d) water loading forcing (m s^{-2},color fill), e) total vertical forcing (sum of B and VPPGF, m s^{-2},color fill), and f) pressure buoyancy forcing (m s^{-2},color fill).

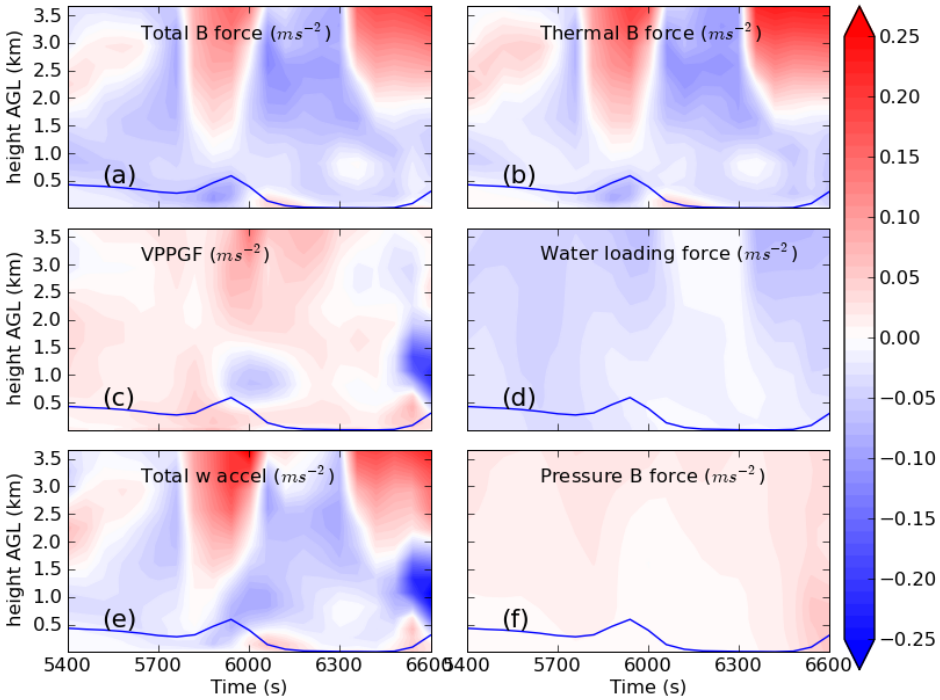

Fig. 6.19. As in Fig. 6.18. but for *250mMY1B*.

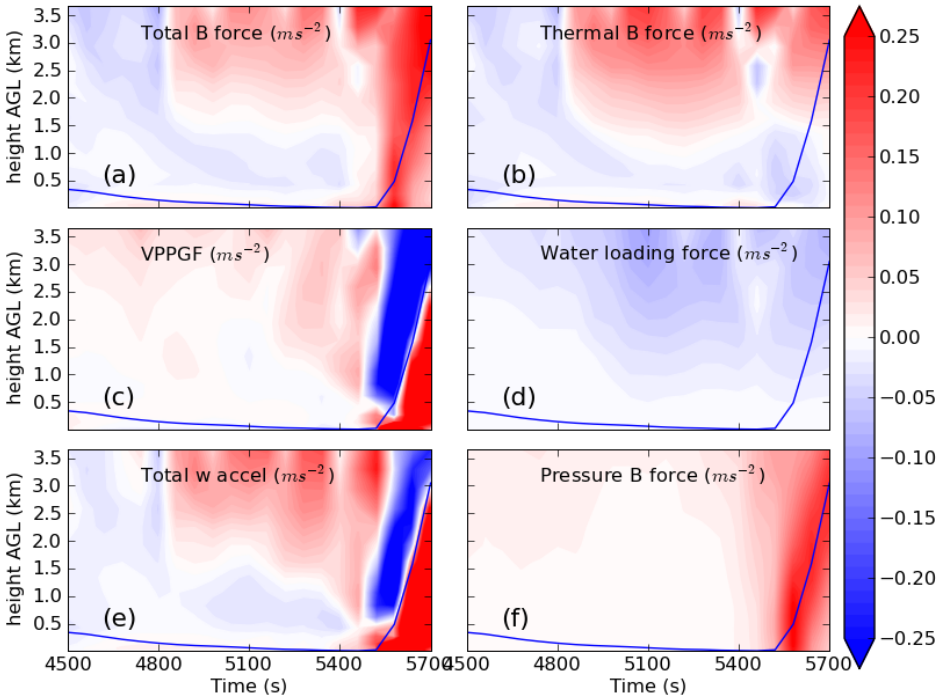

Fig. 6.20. As in Fig. 6.18. but for *250mMY2*.

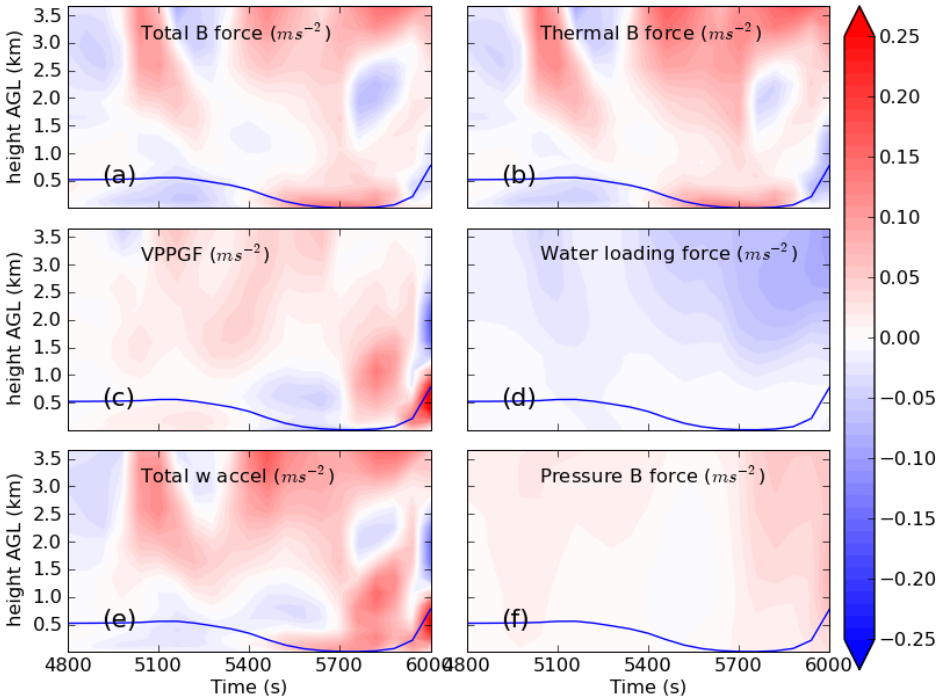

Fig. 6.21. As in Fig. 6.18. but for *250mMY2DA*.

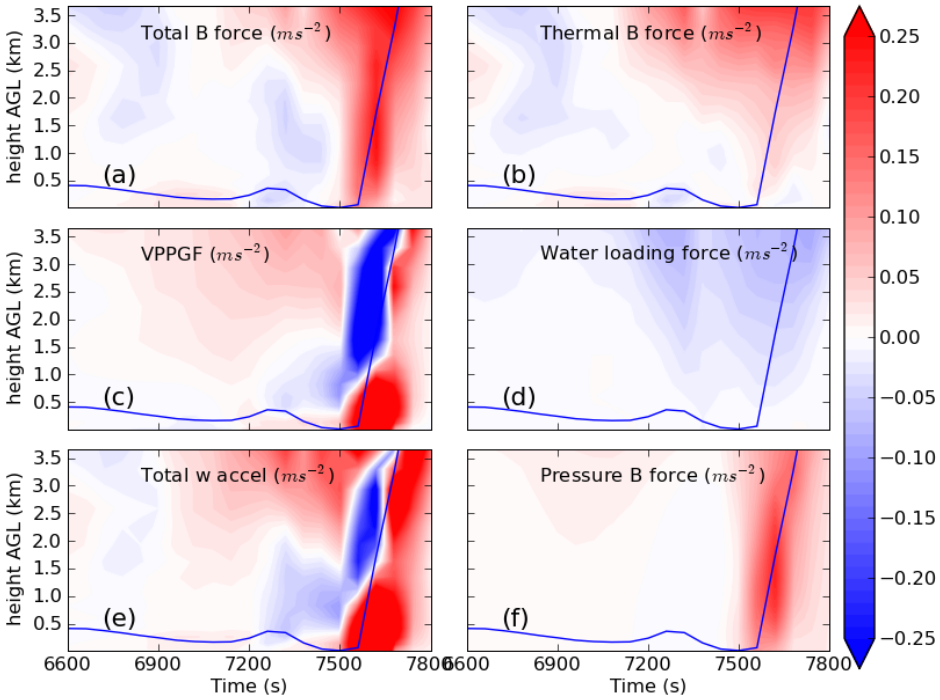

Fig. 6.22. As in Fig. 6.18. but for *250mMY3*.

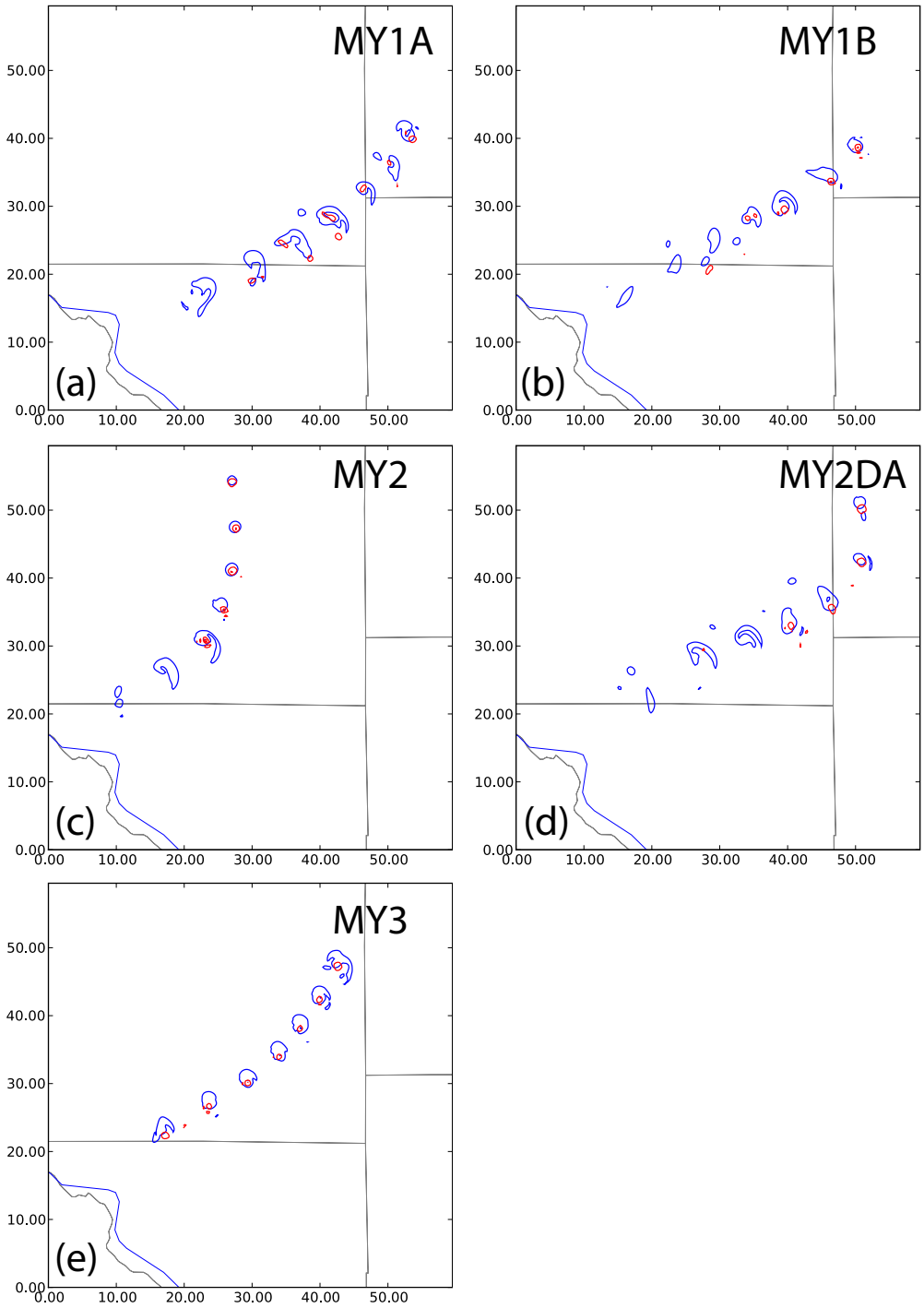

Fig. 6.23. Contours (0.02 s^{-1} and 0.2 s^{-1} shown) of low-level (~1.6 km AGL, blue) and surface (red) vorticity at 10-min intervals from 4500 s to 8100 s for (a) 250mMY1A, (b) 250mMY1B, (c) 250mMY2, (d) 250mMY2DA, (e) 250mMY3.

6.4.4.3 Rain and hail PSD parameters along trajectories

Since, as discussed in previous chapters, variations in the PSD of rain and hail have a profound impact on the amount of evaporative and melting cooling experienced in the low-level downdrafts of storms, it is instructive to examine relevant PSD parameters in the hook echo region of the storms in the 250 m real data experiments and to see how they differ across the schemes used. We present the TH plots in Fig. 6.23 through Fig. 6.27 of various PSD-related parameters of rain and hail for the same trajectories as in the previous section. Shown in each figure are the intercept parameter, mean-mass diameter, and shape parameter for rain and hail. Contours of the mixing ratio and instantaneous evaporative (melting) cooling rate of rain (hail) are also overlaid on the D_m panels for reference. As discussed previously in Chapter 2, however, the intercept parameter's physical meaning changes when the shape parameter is non-zero, and its units depend on the shape parameter. For this reason, a *normalized* N_0 is calculated, based on the formulation of Testud et al.(2001). This normalized N_0 corresponds to the N_0 of an exponential distribution ($\alpha = 0$) with the same water content and mass-weighted mean diameter of the actual distribution, facilitating easier physical interpretation (Testud et al. 2001). (For the case of *250mMY2*, it can be seen that the actual N_0 is in fact equal to the normalized N_0). As in the previous figures, the trajectory height is also overlaid in each panel. Comparison of the various parameters amongst the schemes is very revealing. First we note that in each case, the trajectory chosen passes at some point underneath a concentrated rainshaft (c.f. Figs 6.23-27c), which in each case is associated with the hook echo immediately west of the developing tornado.

In the SM cases (*250mMY1A* and *250mMY1B*; Fig. 6.23 and Fig. 6.24, respectively), due to the constant N_0 specified for rain and hail, D_m is monotonically related to mixing ratio q. D_{mr} is roughly twice as large in *250mMY1B* (Fig. 6.24c) as in *250mMY1A* (Fig. 6.23c), owing to the smaller fixed value of N_{0r} used (Figs. 6.23a, and 6.24a). Accordingly, evaporation rates are significantly larger in *250mMY1A* than in *250mMY1B*, particularly in the first 5 min of the TH plot from the surface to ~2.5 km AGL (Fig. 6.23,24c). This was a time when the trajectories in both runs were passing under a deep rain- and hail-filled downdraft (c.f. Fig. 6.13,14a) in the precipitation core.

In contrast, in the MM runs, the variable N_0 for rain and hail allows for significant variation in the PSD characteristics in different parts of the storm, even for comparable magnitudes of the mixing ratio. First, we note that N_{0r} is significantly smaller than the default M-P value of 8.0×10^6 m^{-4} in most regions (Figs. 6.25-27a), which is associated with D_{mr} values ranging from ~2.0 to 3.5 mm in most regions where $q_r > 1.0$ g kg^{-1} (Figs. 6.25c-27c). In addition, the shape parameter α_r is rather large in *250mMY2DA* (~25-30) and *250mMY3* (~4-6) in these regions, indicating relatively narrow distributions biased toward medium-to-large size drops, particularly in the hook echo rainshaft. The bias towards relatively large drops as inferred from these parameters in the MM runs is consistent with the likely origin of these drops from melted hail (see, e.g., Kumjian and Ryzhkov 2008) and is also consistent with informal observations of the relatively translucent visual appearance of rainshafts in the hook echoes of the 3 May 1999 storms (M02). The flexibility in the DSD offered by the MM formulation is clearly advantageous in this regard, but more confirmation

from observations is needed. For the hail category, the MM runs have regions with larger values of D_{mh} (Figs 6.25d-27d) than is ever reached in the SM runs. In *250mMY2*, for example, D_{mh} reaches 2.5-3.0 cm in the hook echo region. Finally, it should also be pointed out that the mixing ratios for both rain and hail are reduced at the low levels (< ~ 1km) compared to those in the SM runs (Figs. 6.25c,d-27c,d versus Figs. 6.23d-24c,d); this can be attributed to the size-sorting mechanism which is active in the MM runs, but not in the SM runs (see the discussion in Chapter 5 and Fig. 3 of MY05a). The relatively large particle sizes inferred here are, as previously discussed extensively in Chapters 2 and 5, associated with less effective evaporation and melting (physically this is due to the smaller surface area to volume ratio for large drops/stones), and indeed, significant evaporation and melting in the hook echo region in the MM runs is practically non-existent (Figs. 25-27c,d).

In summary, we show that the MM runs tend to produce PSDs of rain and hail in the hook echo that are relatively narrow (large α) and characterized by relatively large drops, as compared with the exponential PSD case with the M-P intercept parameter value for rain in *250mMY1A*. *250mMY1B* produces rain PSDs with D_{mr} closer to the MM runs, but only through a judicious choice of a reduced value of N_{0r}. It cannot be overemphasized that this is an *a priori* specification that may not produce results that are applicable to other types of storms in other environments, or even to other areas of the same storm (such as on the anticyclonic flank, where a stronger cold pool is noted, and plots indicate overall smaller D_{mr} there in the MM runs [not shown]). A final point about the differences in rain evaporation in these real data runs: in all cases the low-levels in the hook echo region were characterized by

relatively high RH, which intrinsically limits evaporation regardless of the nature of the rain DSD. Nevertheless, to the extent at which significant deep downdrafts can be established that entrain low-RH air from mid-levels and also drive the RH down by adiabatic warming, the differences in the DSD and the corresponding evaporation rates can be significant, as found in the idealized simulations of Chapter 5.

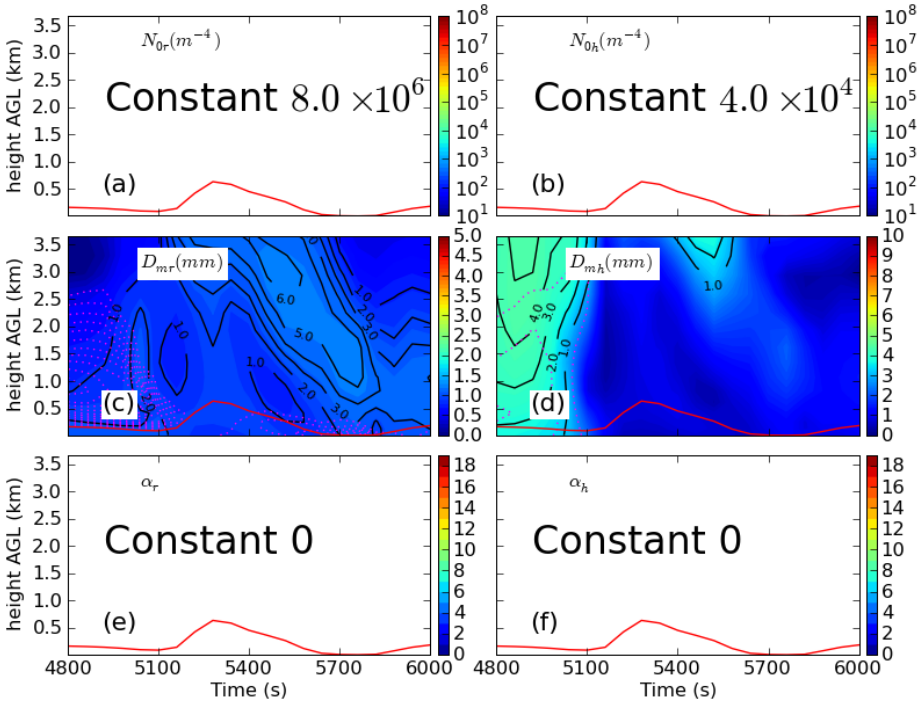

Fig. 6.24. As in Fig. 6.13 but for vertical profiles of PSD parameters for rain (left) and hail (right) along the trajectory path for *250mMY1A*. a) rain intercept parameter N_{0r}, b) hail intercept parameter N_{0h}, c) rain mean-mass diameter D_{mr}, d) hail mean-mass diameter D_{mh}, e) rain shape parameter α_r, f) hail shape parameter α_h. Also shown in c) and d) are rain and hail mixing ratio q_r and q_h, (black solid contours, 1.0 g kg^{-1} increment, starting at 1.0 g kg^{-1}), respectively and instantaneous rain evaporative cooling rate and hail melting cooling rate (dotted magenta contours, 0.0025 K s^{-1} increment, starting at 0.0025 K s^{-1}). Overlaid in each panel is the trajectory height (bold red contour).

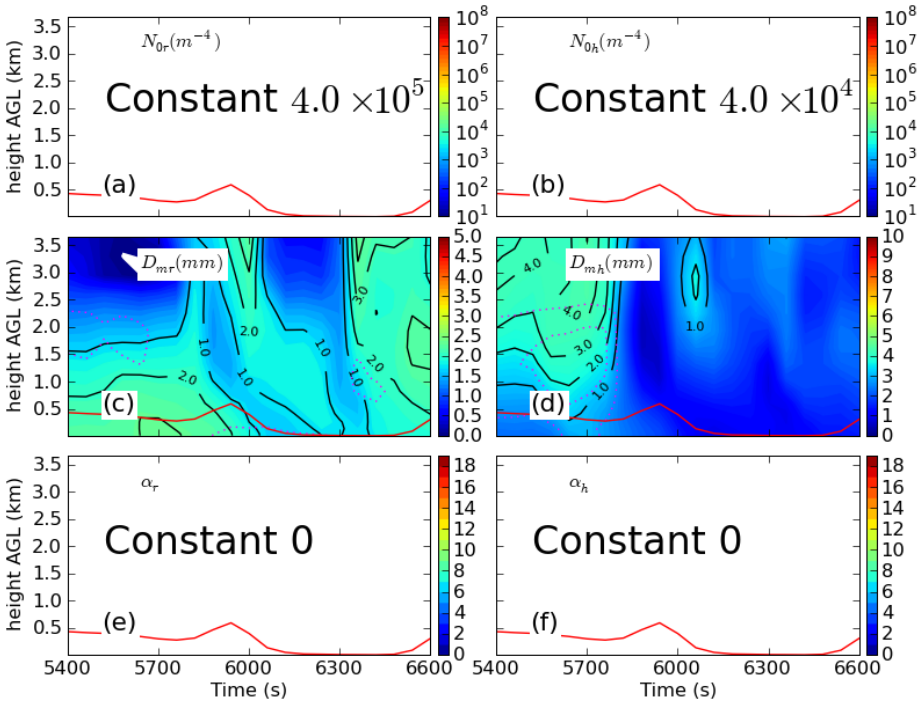

Fig. 6.25. As in Fig. 6.24 but for *250mMY1B*.

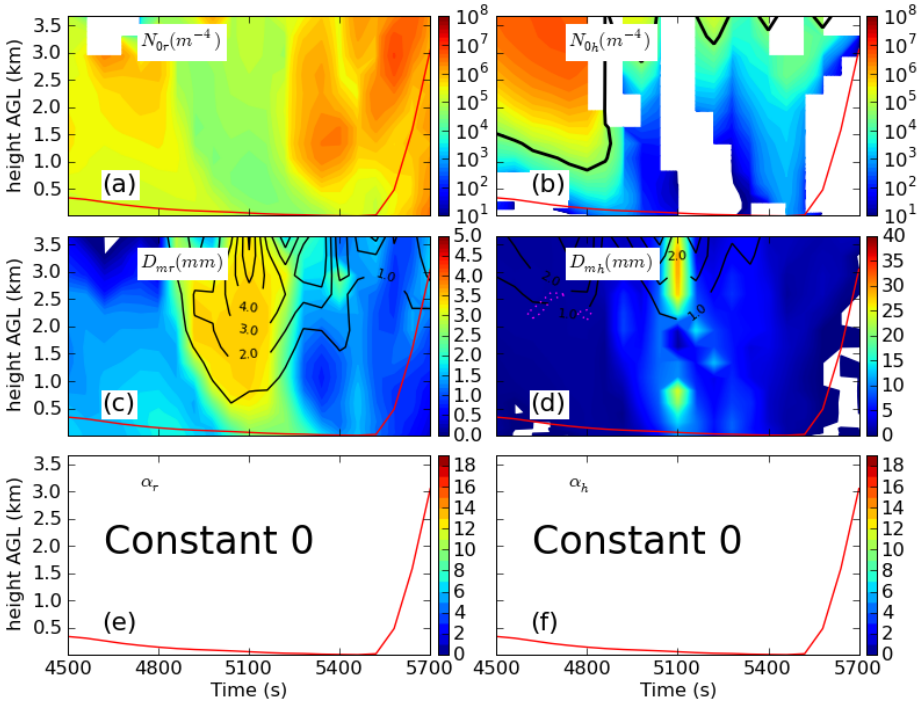

Fig. 6.26. As in Fig. 6.24 but for *250mMY2*. In (b), the SM default fixed N_{0h} = 4.0 x 10^4 m^{-4} is shown as a bold black contour for reference. Note that the scale for D_{mh} in (d) is different than for that in Fig. 6.23.

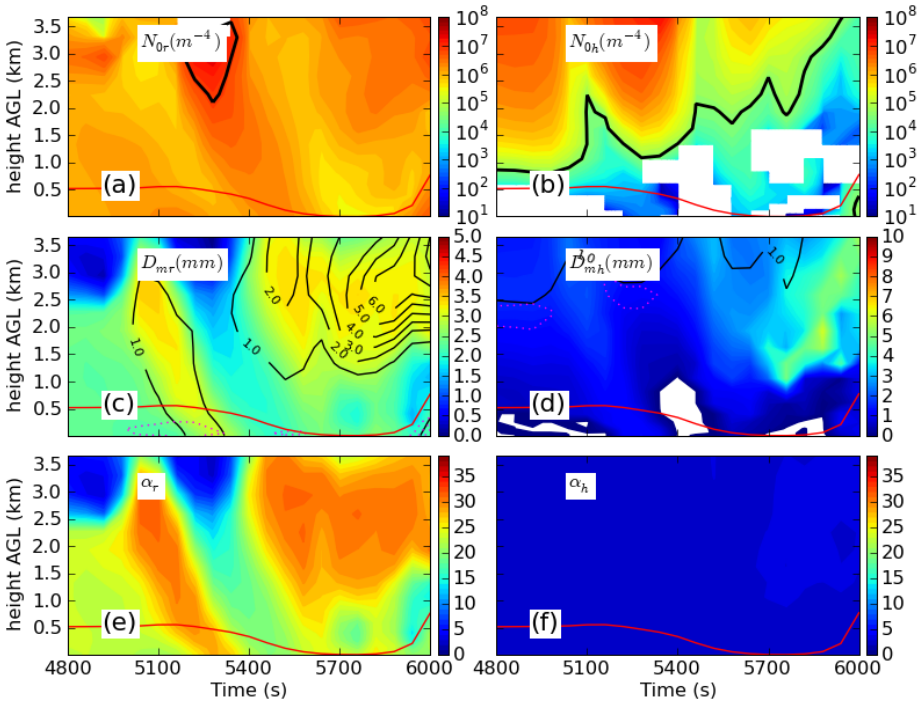

Fig. 6.27. As in Fig. 6.24 but for *250mMY2DA*. In (a) the M-P value of N_{0r} = 8.0 x 10^6 m^{-4} (that used in *250mMY1A*) and in (b) the SM default fixed N_{0h} = 4.0 x 10^4 m^{-4} are shown as bold black contours for reference. Note that the scale for α_r and α_h in (e) and (f) is different than that in Fig. 6.23.

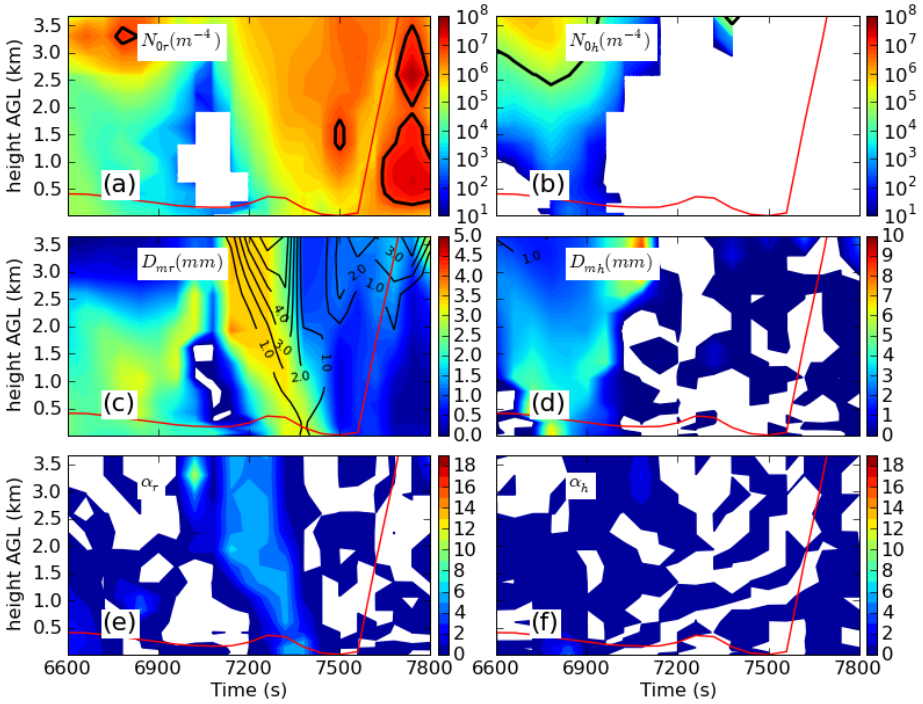

Fig. 6.28. As in Fig. 6.24 but for *250mMY3*.

6.5 Conclusions and Future Research

In this chapter, we have presented results from a set of high-resolution real-data simulations of the 3 May 1999 tornado outbreak, with a focus on storm A, the parent storm of the Bridge Creek-Oklahoma City-Moore F5 tornado (SDS02). The experiments utilized telescoping one-way nested grids from 3 km down to 100 m grid spacing, with intermediate grids of 1 km and 250 m. Results from the 1-km and 250-m experiments were discussed in detail. The 1 km grid was utilized mainly to assimilate mesoscale and radar data, via a 3DVAR+Cloud analysis setup similar to that used in Hu et al. (2006; 2006). It serves to build up the two initial storms in the outbreak during their developing stages (from 2100 UTC to 2230 UTC 3 May 1999) through intermittent data assimilation cycles, and predicts the storms over the ensuing hours (from 2230 UTC to 0300 UTC). We demonstrated that the assimilation of both reflectivity and radial velocity NEXRAD Level-II radar data over a time period of 90 min at 10 min intervals was able to result in a reasonably realistic forecast of the storms and their tracks over 3+ hours, when using a three-moment microphysics scheme.

Starting from the 15-min forecast (valid 2245 UTC) of the 1 km grid, several forecasts at a 250-m horizontal grid spacing were spawned, each with a different version or configuration of the MY microphysics scheme. The 250-m experiments were designed to assess the ability of the model to predict the tornadic behavior of storm A during the time frame when the real storm was producing the long-track F5 tornado, and to examine the microphysics impact on the cold pool, RFD, and tornadogenesis. The results indicate that the findings of the idealized simulations in Chapter 5, in general, hold also for the more complicated real-data, full-physics

framework of these experiments. That is, in general, the MM runs (with the exception of *250mMY2DA* in the first ~¾ of the forecast period) displayed relatively weaker cold pools (as indicated by the extent and magnitude of negative θ_e perturbations) than the SM run using the standard M-P value of N_{0r} = 8.0 x 10^6 m^{-4} (*250mMY1A*). The SM run with N_{0r} = 4.0 x 10^5 m^{-4} (*250mMY1B*) displayed cold pool intensities comparable or even weaker than the MM runs. However, the MM runs all had better reflectivity structure in the forward flank region, as compared with the SM runs, which had forward flank reflectivity regions that were too small in the E-W extent compared to observations; these results are also consistent with the idealized simulations of Chapter 5. The latter results were attributed to the process of size-sorting, which is parameterized in the MM runs through the differential sedimentation of the predicted moments, while it is absent entirely within the same hydrometeor category in the SM runs (a single mass-weighted mean fall speed is used for the hydrometeor field at a given point). The hook echo region was also found to be simulated much more realistically in the MM runs, particularly in *250mMY2* and *250mMY3*, with relatively small θ_e perturbations (~5 K or less) in this region through most of the simulation period. This is consistent with mobile mesonet observations near the hook echo and tornado regions of storms A and B (Markowski 2002); relatively small θ_e perturbations were observed there.

In addition to the above results, the simulation of tornadic circulations within the 250-m experiments was also improved in the MM runs. *250mMY3* produced a long-track tornado which was qualitatively similar in both length and duration to the observed F5 tornado track. In contrast, the tornado development was delayed by

approximately 45 min in *250mMY2*, by approximately 1 h in *250mMY2DA*, by almost 1 h 15 min in *250mMY1B*. *250mMY1A*, which had the strongest cold pools, produced only weak, short-lived vortices. An analysis of the vertical momentum equation forcing terms along trajectories that passed through the near-tornado RFD on their way to the tornado was performed for each simulation. Although more work needs to be done (i.e., examining more trajectories at different times), preliminary results indicate that the greater negative buoyancy in the low-level hook echo/RFD regions of *250mMY1A*, *250mMY1B*, and *250mMY2DA* suppresses tornadogenesis and/or intensification and also leads to vertical decoupling of the developing surface vortex from the mid-to-low-level mesocyclone by virtue of stronger low-level outflow. In contrast, the negative buoyancy is weak or nearly non-existent in *250mMY2* and *250mMY3* which produce the strongest, longest-lasting, tornadoes. These results were shown to be consistent with recent numerical and observational studies on the relationship between RFD thermodynamics and tornadogenesis. Finally, an examination of the PSD parameters of rain and hail in the RFD region showed that the MM runs tend to produce PSDs biased towards larger raindrops and hailstones, and in the case of the MM runs (*250mMY2DA* and *250mMY3*) with variable PSD shape parameter, the PSDs obtained are relatively narrow. In contrast, the typical values of the fixed intercept parameters for rain and hail in the SM runs tended to produce PSDs weighted toward smaller drops/stones.

In future work, we plan to continue the analysis of the impact of microphysics on RFD thermodynamics and tornadogenesis. In addition to completing the analysis of the 100-m grid results to examine the impact of further refinement of the horizontal

grid, there are other potential avenues for fruitful research. The work described here focused on the near-tornado RFD environment in both time and space. Comparatively little attention was given to the differences across the cold pool in time and space within even a single run. Most of the simulations had times when regions of relatively colder outflow penetrated into the hook echo region. We plan to investigate the source of this cold air, which likely was derived from the relatively dry mid-level storm-relative inflow, as opposed to the mainly recycled BL air that is seen in the "warm RFD surges". It is believed that the relative frequency of cold outflow vs. warm outflow episodes is determined by how effectively the potentially cold storm-relative mid-level dry air can penetrate to the surface, which in turn is dependent on the diabatic cooling effects of microphysics. In the current simulations, even though the MM runs have relatively strong cold pools, they are mostly confined near and northwest of the core reflectivity region, whereas in the SM runs, even in *250mMY1B*, there is a tendency for relatively cold air to also be present in the hook echo region. It is believed that the flexibility of the MM schemes, with their ability to predict PSDs, and allow for size sorting within the species, combined with the complex 3D nature of the storms, is leading to variations in the PSD across different regions of the storm that in turn is leading to these cold pool differences. The SM runs would have comparatively less variation since the PSD is tied uniquely to the mixing ratio, which would explain why the cold pool is more uniformly distributed throughout the precipitating region of the storm, including the hook echo region.

We wish also to inspect the source and sink terms in the vorticity equation to assess the dominant mechanisms responsible for vorticity generation and transport to

the developing tornadoes. While past modeling work has investigated this problem (e.g., Klemp and Rotunno 1983; Wicker and Wilhelmson 1993; Xue et al. 1993; Grasso and Cotton 1995; Wicker and Wilhelmson 1995, M03), this has not been, in general, done in the context of variations in PSDs of hydrometeors in the tornado environment, and their impacts, e.g., on baroclinic vorticity production or transport of angular momentum to low-levels by hydrometeor drag; the relative importance of these and other processes in different situations in which microphysics can vary significantly still requires much research.

Finally, an investigation of the modeled tornado structure itself is planned. As an example of possible tornado-scale features that might be investigated, Fig. X shows TH plots of the vertical momentum forcing terms, following the developing tornado, for experiment *250mMY2*. At each time, the maximum vorticity at each height below 4 km within a box 3 km on a side centered on the surface vortex center (to allow for tilt of the vortex) was used to produce the TH plot. Of interest is the vertical structure of the VPPGF seen in Fig. 6.29c, which may be due to centrifugal wave instability in the vortex. Since, as already mentioned, 250-m grid spacing is probably too coarse to resolve sub-tornado scale features, and in fact the tornado itself is only marginally resolved, this will require simulations at smaller horizontal grid spacings (100 m or less) to determine if such features are actual physical features of the flow, are computational artifacts, or artifacts due to the use of the inherently noisy field of vorticity to fix the vortex location for the TH plots.

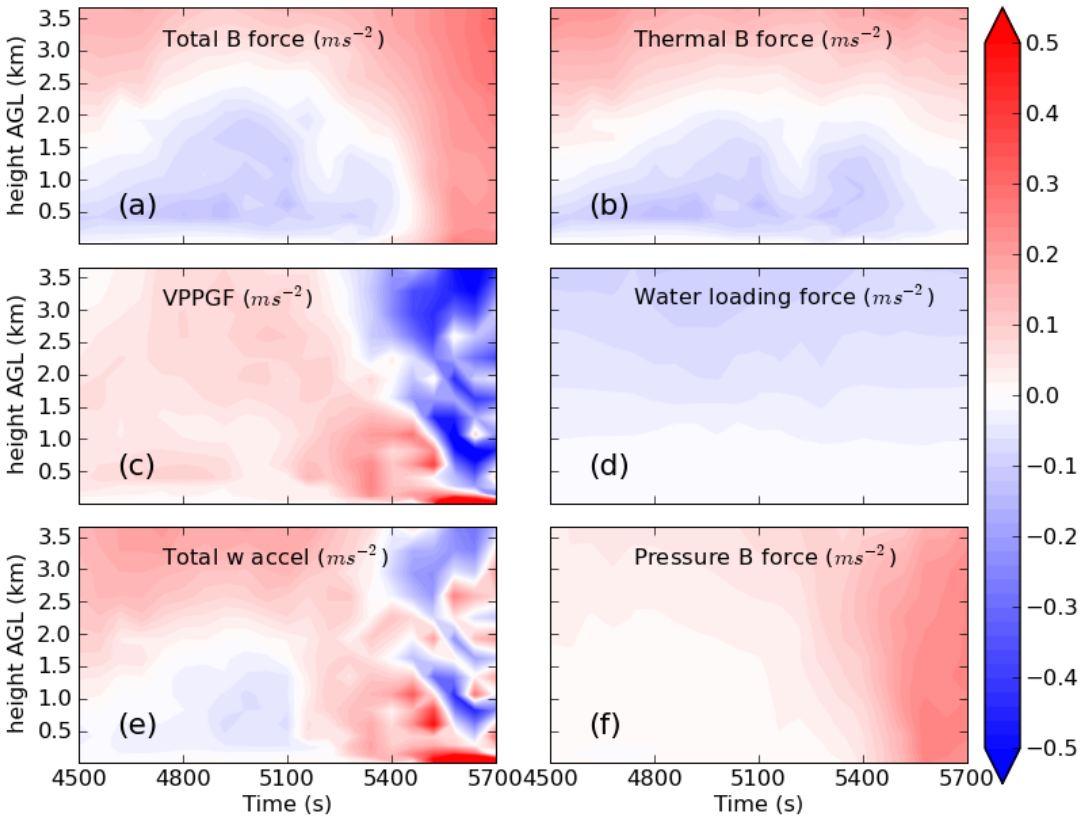

Fig. 6.29. As in Fig. 6.18 but for *250mMY2* and for the (tilted) column following the tornado vortex between 4500 s and 5700 s.

Chapter 7 Conclusions

7.1 General Summary

Cloud and precipitation microphysics is one of the most important and fundamental physical characteristics of deep moist convection, and also one of the most complex and poorly understood. Numerous observational, theoretical, and numerical studies have vastly improved our understanding of these processes within cloud and storm systems, but much remains to be learned. This work has attempted to build up our understanding by focusing on the particular line of investigation of bulk microphysical parameterizations (BMPs) as applied to simulations of supercell convection, using the Advanced Regional Prediction System (ARPS) model. We have shown, in agreement with much past work, that many details of the behavior of simulated supercells is sensitively-dependent on the choice of type of microphysics scheme, or parameters within a given scheme. The main emphasis of this work was ascertaining the impact of microphysics on the low-level downdrafts, associated cold pools, and reflectivity structure in supercells, understanding the physical mechanisms behind the main processes responsible for cold pool development and intensity changes, and their feedbacks to storm structure and tornadogenesis potential. In particular, we have shown that multi-moment (MM) schemes have several inherent advantages over their single-moment (SM) counterparts in their treatment of the processes of evaporation and melting -- which are partially due to the additional flexibility in the particle size distribution (PSD) -- that lead to significant improvements in the simulation of supercell cold pools. This study represents one of the first of its kind to systematically investigate MM microphysics parameterizations

in the context of simulation and prediction of supercell thunderstorms and associated tornadoes. In the particular case studied in this dissertation, the 3 May 1999 outbreak, the most significant improvement seen was a removal or reduction in the common "cold bias" seen in many past numerical studies of supercells (Markowski 2002; Markowski et al. 2002). In the following section, we provide a chapter-by-chapter summary of the dissertation that illustrates the main findings of this research.

7.2 Chapter Summary

In the first section of Chapter 2, an overview of the BMP method was given along with a brief comparison to other methods, such as the spectral bin method. A description of the hydrometeor categories commonly-used in BMPs was given. Two common functional forms of the PSD, which must be specified in BMPs for the various hydrometeor categories, the exponential and gamma distributions, were described. Past studies exploring the sensitivity of simulated storm characteristics, such as precipitation amount and cold pool strength, to variations in parameters of SM schemes were summarized. Improvements over the SM moment approach that have the effect of mitigating some of this sensitivity were discussed, including the increasingly-popular MM approach, the use of which is a main focus of this dissertation. The attractiveness of the MM approach lies mainly in the greater flexibility in the PSD obtained, by virtue of allowing the fixed parameters in the PSD function to vary independently (e.g. the intercept parameter N_0 in the exponential distribution, which must be fixed or diagnosed in a SM scheme, can vary independently from the slope parameter λ in a double-moment or higher scheme).

The last two sections of Chapter 2 focused on a description of the microphysics schemes available in the ARPS model that were used in this study, including a version of the popular LFO scheme (Lin et al. 1983; Tao and Simpson 1993), the WRF Single-Moment 6-Class scheme (WSM6, Hong and Lim 2006), and the Milbrandt and Yau multi-moment scheme (MY, Milbrandt and Yau 2005; Milbrandt and Yau 2005), which can be run in any of four modes (single-moment, double-moment, double-moment with diagnostic α, and the full triple-moment formulation). A comparison was made between the various schemes used in this study, with a focus on the processes most responsible for latent heat changes in the low-level downdrafts of convective storms: cloud and rain evaporation, melting of hail, and collection of rain by hail.

In Chapter 3, a brief overview of the 3 May 1999 outbreak is given from a synoptic to tornado-scale perspective, and past studies are summarized. An account of the tornadic supercell that produced the Moore, OK F5 tornado (tornado "A9" of storm "A") was given.

In Chapter 4, a brief summary of an initial set of real-data experiments from which a sounding was extracted to provide the homogeneous environment for the idealized simulations of chapter 5 was given. It was found that at the relatively course horizontal grid spacings of 3 km used in these experiments, that all the microphysics schemes tested over-predicted cold pool intensity and area, which was attributed potentially to the relatively course resolution used, in which mixing processes are poorly resolved.

In Chapter 5, a set of idealized high-resolution single-sounding supercell storm simulations (at 500 m and 250 m grid spacing) were presented, making use of an extracted sounding from a prior real-data experiment. Several different microphysics schemes and configurations were tested, including three SM schemes, and three MM schemes. It was found that the MM schemes performed better than the SM schemes in producing storms with relatively weak and small cold pools without any tuning, which was much more consistent with the observations. In contrast, the SM schemes showed a tendency to produce strong and large cold pools when typical values of the intercept parameters for the various hydrometeor exponential PSDs were chosen. Furthermore, changes in these fixed intercept parameters had large first-order effects on the cold pool size and strength. Several important advantages of the MM schemes over the SM ones were brought to light by these results. These include the better physical representation of the evaporation and melting processes (in particular, by allowing N_0 to decrease during these processes), and the process of size-sorting, which is modeled through the differential sedimentation of the predicted moments, which, taken together lead to overall smaller magnitudes of evaporation and melting, all other things being equal, than in a typical SM scheme. Accordingly, it was argued that the MM approach is very attractive for storm modeling, since it provides for better physical realism and reduces the amount of "tuning" required for a given case.

In Chapter 6, a set of high-resolution real-data experiments of the 3 May 1999 outbreak, with a focus on the prediction of storm A and its associated long-track F5 tornado were described. Telescoping one-way nested grids were utilized with grid

spacings of 3 km, 1 km, 250 m, and 100 m, the later two grids of which were designed to simulate tornadoes within the storms. These experiments were designed to confirm the results of the idealized simulations within the context of the more complicated real-data, full-physics approach. This more sophisticated setup, which included 3DVAR assimilation of various sources of data, including Oklahoma mesonet data and NEXRAD Level II reflectivity data was also ideal to test the impact of MM vs. SM microphysics on realistic simulation and prediction of the storms and tornadoes, both to assess the sensitivity of the forecast to these different schemes, and also to examine the physical processes impacting tornadogenesis. It was found that, in general, the results of the idealized simulations held true for the real-data experiments as well, in that the MM runs were generally superior to the SM runs in prediction of cold pool intensity and reflectivity structure.

Considerable variability in the timing of tornadogenesis and intensity of tornadoes was seen across the simulations performed at 250 m grid spacing, indicating that microphysical processes are an important component of the cascade of physical processes leading to tornadogenesis. In general, the MM runs performed significantly better than the SM runs in predicting the intensity, timing, and longevity of tornadoes. The MY3 scheme produced the best track prediction, with a qualitatively very similar track (both length and duration) to the observed F5 tornado track. In contrast, the MY1 scheme, using the typical M-P distribution for rain (MY1A) produced only weak, short-lived tornadoes. An analysis of the forcing for vertical motion in the near-tornado RFD air indicated that in the runs (mostly the SM runs) in which cold, low-θ_e surface air was present in this region, the development of

a strong tornadic vortex was impeded. This was due at least partially to the negative buoyancy impeding upward vertical acceleration of the air entering the incipient tornado at low-levels, but also due to the decoupling of the developing low-level circulation from the low-level mesocyclone circulation and associated updraft, due to the stronger undercutting outflow.

In contrast, in the runs (especially the MY2 and MY3 runs) in which the near-tornado RFD air was relatively warm (having originated from the warm, moist BL inflow and re-circulated through the RFD), stronger, long-lived tornadic vortices formed more readily, both because of less impedance to vertical acceleration by the less negatively-buoyant (or even positively buoyant) near-surface air entering the tornado, and because of greater vertical continuity of the developing surface circulation with the low-level mesocyclone. The latter allows for stronger vertical stretching of vorticity over the developing tornadic circulation, which leads to enhanced convergence and greater near-surface upward VPPGF to help overcome any weak negative buoyancy at low levels.

7.3 Future work and implications for storm-scale NWP

The results of this dissertation research indicate that multi-moment bulk microphysics parameterization is a robust and promising approach for convective storm simulation and prediction, even down to the scale of tornadic circulations. The comparison of the various SM and MM schemes also indicate that cloud and precipitation microphysics in general is one of the greatest sources of uncertainty in numerical simulation and prediction of severe convective storms. Thus, the choice of microphysics parameterization has wide-sweeping implications for the numerical

simulation and prediction of convection. We will describe in this section some avenues for future work that will attempt to address some of these implications.

In the immediate future, we plan to continue the analysis of the 3 May 1999 real-data simulations discussed in Chapter 6 with the following foci:

1) Examine further the mechanisms important for tornadogenesis (or tornadogenesis failure), tornado longevity and intensity across the simulations by vorticity and circulation budget analyses, with an emphasis on the impact of microphysical processes. Questions needing answers include: what are the feedbacks, both dynamic and thermodynamic, of the PSD of rain and hail in the hook echo region to the development of low-level rotation and subsequent stretching and intensification into a tornado-intensity vortex?

2) Repeat the analyses on the 100-m simulation results to examine the impact of further refinement of the horizontal grid, and on the possible improvement to the tornado prediction.

Of great interest to both the storm research and forecasting communities are the salient differences between nontornadic and tornadic supercells that lead to their respective behaviors. As pointed out by MSR02, there appears to be no systematic differences between the radar presentations of nontornadic and tornadic supercells. As discussed in Chapter 6 of this dissertation, the results of the real-data simulations strongly support the conclusions of MSR02 and M03 that significant tornadoes are more likely in supercells in which relatively warm low-level air is present in the RFD region, as is the case in general in the MM simulations herein. The particular case chosen for this study, the 3 May 1999 tornado outbreak, was one of the most prolific

tornado-producing outbreaks in history, especially when considering that nearly every right-moving supercell of the outbreak was tornadic (SDS02), and often significantly so. In many other supercell events, there may be several supercells, none (or only a few) of which are tornadic. Thus, in future work we would like to extend this investigation into one or more cases that include mostly nontornadic supercells and those that are "marginally" tornadic (that is, produce no significant tornadoes, where significant in this context means no tornadoes greater than EF2 intensity). Other scenarios--in which the microphysical processes may vary significantly from the typical mid-latitude continental supercell environment--that may be investigated are tornadoes that occur in "mini-supercells" in the presence of a cold-core mid-tropospheric closed lows (see, e.g., Davies 2006; Snyder et al. 2006) or in the outer rainbands of tropical cyclones (see, e.g., McCaul 1991; McCaul and Weisman 1996; Suzuki et al. 2000). Can the MM microphysics approach reliably discriminate between tornadic and nontornadic supercells in these varied environments? In addition to supercells, it is clear that the sensitivity to microphysics extends to other types of convective systems, including multi-cell clusters, squall lines, bow-echoes, and mesoscale convective vortices, all possible avenues for future research.

Finally, the superiority of the MM over the SM approach has important implications in the area of storm-scale radar data assimilation, especially when polarimetric data are available. Jung et al. (2009) found that their polarimetric radar data emulator, when applied to idealized supercell storm simulations using the ARPS model and the DM version of the MY BMP, was able to accurately reproduce many distinctive polarimetric radar signatures seen in observations of supercell storms (see,

e.g., Kumjian and Ryzhkov 2008; Romine et al. 2008), while the SM scheme performed very poorly. Jung et al. (2009) suggest that assimilation of polarimetric radar data may thus only be useful if a DM or higher bulk microphysics scheme is used. In addition to these considerations, while it might first appear attractive, in, e.g., an Ensemble Kalman Filter (EnKF) data assimilation paradigm, to take advantage of the spread of solutions provided in an ensemble that varies the parameters in a SM scheme across the ensemble members, the results of this study indicate that SM schemes are physically deficient in several important microphysical processes and that these deficiencies have important detrimental feedbacks to storm structure and behavior. Thus such ensemble spread would not accurately reproduce the actual spread of uncertainty of a given situation. In such a case, it might be better to utilize a more advanced and accurate MM scheme for most if not all ensemble members, and provide for ensemble spread through standard variation of initial and boundary conditions, or through the varying of certain other uncertain microphysical parameters, such as initial CCN concentration, which is not directly related to the physics of the microphysical processes themselves. Clearly, much more research is needed in this area, and the application of MM schemes to advanced storm-scale data assimilation and prediction is a medium-to-long-term goal of the author's research.

REFERENCES

Adlerman, E. J. and K. K. Droegemeier, 2002: The sensitivity of numerically simulated cyclic mesocyclogenesis to variations in model physical and computational parameters. *Mon. Wea. Rev.*, **130,** 2671-2691.

——, 2005: The dependence of numerically simulated cyclic mesocyclogenesis upon environmental vertical wind shear. *Mon. Wea. Rev.*, **133,** 3595-3623.

——, 2005: A numerical simulation of cyclic tornadogenesis. *J. Atmos. Sci.*, Submitted.

Adlerman, E. J., K. K. Droegemeier, and R. Davies-Jones, 1999: A numerical simulation of cyclic mesocyclogenesis. *J. Atmos. Sci.*, **56,** 2045–2069.

Bolton, D., 1980: The computation of equivalent potential temperature. *Mon. Wea. Rev.*, **108,** 1046-1053.

Brewster, K., 1996: Application of a Bratseth analysis scheme including Doppler radar data. *Preprints, 15th Conf. Wea. Anal. Forecasting*, Norfolk, VA, Amer. Meteor. Soc., 92-95.

——, 2002: Recent advances in the diabatic initialization of a non-hydrostatic numerical model. *Preprints, 15th Conf on Numerical Weather Prediction and 21st Conf on Severe Local Storms*, San Antonio, TX, Amer. Meteor. Soc., J6.3.

Brooks, H. E. and C. A. Doswell, 2002: Deaths in the 3 May 1999 Oklahoma City tornado from a historical perspective. *Wea. Forecasting*, **17,** 354-361.

Bryan, G. H., J. C. Wyngaard, and J. M. Fritsch, 2003: Resolution requirements for the simulation of deep moist convection. *Mon. Wea. Rev.*, **131,** 2394-2416.

Byers, H. R., 1965: Elements of Cloud Physics. *The University of Chicago Press*, 191.

Cohen, C. and E. W. McCaul, 2006: The sensitivity of simulated convective storms to variations in prescribed single-moment microphysics parameters that describe particle distributions, sizes, and numbers. *Mon. Wea. Rev.*, **134,** 2547-2565.

Cooper, W. A., 1986: Ice initiation in natural clouds. *Precipitation Enhancement-A Scientific Challenge, Meteor. Monogr.*, Amer. Meteor. Soc., 29-32.

Davies-Jones, R., 2003: An expression for effective buoyancy in surroundings with horizontal density gradients. *J. Atmos. Sci.*, **60,** 2922-2925.

Davies, J. M., 2006: Tornadoes with cold core 500-mb lows. *Wea. Forecasting,* **21,** 1051-1062.

Dawson, D. T., II, M. Xue, J. A. Milbrandt, and M. K. Yau, 2009: The effects of evaporation and melting in a multi-moment bulk microphysics scheme on the low-level downdrafts and surface cold pools in simulations of the 3 May 1999 Oklahoma tornadic thunderstorms. *Mon. Wea. Rev.***,** Conditionally accepted.

Dawson, D. T., II, M. Xue, J. A. Milbrandt, M. K. Yau, and G. Zhang, 2007: Impact of multi-moment microphysics and model resolution on predicted cold pool and reflectivity intensity and structures in the Oklahoma tornadic supercell storms of 3 May 1999. *22nd Conf. Wea. Anal. Forecasting/18th Conf. Num. Wea. Pred.*, Salt Lake City, Utah, Amer. Meteor. Soc., CDROM 10B.2.

Doswell, C. A. and P. M. Markowski, 2004: Is buoyancy a relative quantity? *Mon. Wea. Rev.*, **132,** 853-863.

Doswell, C. A., III and D. W. Burgess, 1993: Tornadoes and tornadic storms: A review of conceptual models. *The Tornado: Its Structure, Dynamics, Prediction, and Hazards, Geophys. Monogr.*, Amer. Geophys. Union, 75-88.

Feingold, G., Z. Levin, and S. Tzivion, 1991: The evolution of raindrop spectra. Part III: Downdraft generation in an axisymmetrical rainshaft model. *J. Atmos. Sci.*, **48,** 315-330.

Feltz, W. F. and J. R. Mecikalski, 2002: Monitoring high-temporal-resolution convective stability indices using the ground-based Atmospheric Emitted Radiance Interferometer (AERI) during the 3 May 1999 Oklahoma-Kansas tornado outbreak. *Wea. Forecasting*, **17,** 445-455.

Ferrier, B. S., 1994: A double-moment multiple-phase four-class bulk ice scheme. Part I: Description. *J. Atmos. Sci.*, **51,** 249-280.

Ferrier, B. S., W.-K. Tao, and J. Simpson, 1995: A double-moment multiple-phase four-class bulk ice scheme. Part II: Simulations of convective storms in different large-scale environments and comparisons with other bulk parameterizations. *J. Atmos. Sci.*, **52,** 1001-1033.

Fujita, T. T., 1971: A proposed characterization of tornadoes and hurricanes by area and intensity. SMRP Res. Paper 91. *Dept. of Geophysical Sciences*, **University of Chicago,** 42.

Gao, J.-D., M. Xue, K. Brewster, and K. K. Droegemeier, 2004: A three-dimensional variational data analysis method with recursive filter for Doppler radars. *J. Atmos. Ocean. Tech.*, **21,** 457-469.

Gilmore, M. S. and L. J. Wicker, 1998: The influence of midtropospheric dryness on supercell morphology and evolution. *Mon. Wea. Rev.*, **126,** 943-958.

Gilmore, M. S., J. M. Straka, and E. N. Rasmussen, 2004: Precipitation and evolution sensitivity in simulated deep convective storms: Comparisons between liquid-only and simple ice and liquid phase microphysics. *Mon. Wea. Rev.*, **132,** 1897-1916.

——, 2004: Precipitation uncertainty due to variations in precipitation particle parameters within a simple microphysics scheme. *Mon. Wea. Rev.*, **132,** 2610-2627.

Grasso, L. D. and W. R. Cotton, 1995: Numerical Simulation of a tornado vortex. *J. Atmos. Sci.*, **52,** 1192-1203.

Gunn, K. L. S. and J. S. Marshall, 1958: The distribution with size of aggregate snow flakes. *J. Meteor.*, **15,** 452-461.

Hong, S.-y. and J.-O. J. Lim, 2006: The WRF single-moment 6-class microphysics scheme (WSM6). *J. Korean Meteor. Soc.*, **42,** 129-151.

Hong, S.-Y., J. Dudhia, and S.-H. Chen, 2004: A revised approach to ice microphysical processes for the bulk parameterization of clouds and precipitation. *Mon. Wea. Rev.*, **132,** 103-120.

Hu, M. and M. Xue, 2007: Impact of configurations of rapid intermittent assimilation of WSR-88D radar data for the 8 May 2003 Oklahoma City tornadic thunderstorm case. *Mon. Wea. Rev.*, **135,** 507–525.

Hu, M., M. Xue, and K. Brewster, 2006: 3DVAR and cloud analysis with WSR-88D level-II data for the prediction of Fort Worth tornadic thunderstorms. Part I: Cloud analysis and its impact. *Mon. Wea. Rev.*, **134,** 675-698.

Hu, M., M. Xue, J. Gao, and K. Brewster, 2006: 3DVAR and cloud analysis with WSR-88D level-II data for the prediction of Fort Worth tornadic thunderstorms. Part II: Impact of radial velocity analysis via 3DVAR. *Mon. Wea. Rev.*, **134,** 699-721.

Johnson, D. E., P. K. Wang, and J. M. Straka, 1993: Numerical simulations of the 2 August 1981 CCOPE supercell storm with and without ice microphysics. *J. Appl. Meteor.*, **32,** 745-759.

Jung, Y., M. Xue, and G. Zhang, 2009: Polarimetric radar signatures of a simulated supercell storm using a two-moment microphysics scheme and polarimetric radar emulator. *J. Appl. Meteor. Climatol.***,** Submitted.

Kessler, E. I., 1969: *On the distribution and continuity of water substance in atmospheric circulations. Meteor. Monogr. No. 32,* Amer. Meteor. Soc., 84 pp.

Klemp, J. B. and R. B. Wilhelmson, 1978: Simulations of right- and left-moving thunderstorms produced through storm splitting. *J. Atmos. Sci.*, **35,** 1097-1110.

——, 1978: The simulation of three-dimensional convective storm dynamics. *J. Atmos. Sci.*, **35,** 1070-1096.

Klemp, J. B. and R. Rotunno, 1983: A study of the tornadic region within a supercell thunderstorm. *J. Atmos. Sci.*, **40,** 359-377.

Klemp, J. B., R. B. Wilhelmson, and P. S. Ray, 1981: Observed and numerically simulated structure of a mature supercell thunderstorm. *J. Atmos. Sci.*, **38,** 1558-1580.

Kong, F. Y. and M. K. Yau, 1997: An explicit approach to microphysics in MC2. *Atmos.-Ocean*, **35,** 257-291.

Kumjian, M. R. and A. V. Ryzhkov, 2008: Polarimetric signatures in supercell thunderstorms. *J. Appl. Meteor. Climatol.*, **47,** 1940-1961.

Li, X. and R. C. Srivastava, 2001: An analytical solution for raindrop evaporation and its application to radar rainfall measurements. *J. Appl. Meteor.*, **40,** 1607-1616.

Lin, Y.-L., R. D. Farley, and H. D. Orville, 1983: Bulk parameterization of the snow field in a cloud model. *J. Climate Appl. Meteor.*, **22,** 1065-1092.

Lynn, B. H., A. P. Khain, J. Dudhia, D. Rosenfeld, A. Pokrovsky, and A. Seifert, 2005: Spectral (bin) microphysics coupled with a mesoscale model (MM5). Part I: Model description and first results. *Mon. Wea. Rev.*, **133,** 44-58.

——, 2005: Spectral (bin) microphysics coupled with a mesoscale model (MM5). Part II: Simulation of a CaPE rain event with a squall line. *Mon. Wea. Rev.*, **133,** 59-71.

Mansell, 2008: EnKF analysis and forecast predictability of a tornadic supercell storm. *24th Conference on Severe Local Storms*, Savannah, GA, American Meteorological Society, P5.2.

Markowski, P. M., 2002: Mobile mesonet observations on 3 May 1999. *Wea. Forecasting*, **17,** 430–444.

——, 2002: Hook echoes and rear-flank downdrafts: A review. *Mon. Wea. Rev.*, **130,** 852-876.

Markowski, P. M., J. M. Straka, and E. N. Rasmussen, 2002: Direct surface thermodynamic observations within the rear-flank downdrafts of nontornadic and tornadic supercells. *Mon. Wea. Rev.*, **130,** 1692-1721.

——, 2003: Tornadogenesis resulting from the transport of circulation by a downdraft: Idealized numerical simulations. *J. Atmos. Sci.*, **60,** 795-823.

Marshall, J. S. and W. M. Palmer, 1948: The distribution of raindrops with size. *J. Meteor.*, **5,** 165-166.

McCaul, E. W., 1991: Buoyancy and shear characteristics of hurricane tornado environments. *Mon. Wea. Rev.*, **119,** 1954-1978.

McCaul, E. W. and M. L. Weisman, 1996: Simulations of shallow supercell storms in landfalling hurricane environments. *Mon. Wea. Rev.*, **124,** 408-429.

McCumber, M., W.-K. Tao, and J. Simpson, 1991: Comparison of ice-phase microphysical parameterization schemes using numerical simulations of tropical convection. *J. Appl. Meteor.*, **30,** 985-1004.

McDonald, J. R. and K. C. Mehta: A recommendation for an enhanced Fujita scale (EF-Scale) submitted to the National Weather Service and other interested users. [Available online from http://www.wind.ttu.edu/EFScale.pdf.]

Mesinger, F., G. DiMego, E. Kalnay, K. Mitchell, P. C. Shafran, W. Ebisuzaki, Jovi, Du, an, J. Woollen, E. Rogers, E. H. Berbery, M. B. Ek, Y. Fan, R. Grumbine, W. Higgins, H. Li, Y. Lin, G. Manikin, D. Parrish, and W. Shi, 2006: North American Regional Reanalysis. *Bull. Amer. Meteor. Soc.*, **87,** 343-360.

Meyers, M. P., R. L. Walko, J. R. Harrintong, and W. R. Cotton, 1997: New RAMS cloud microphysics parameterization. Part II: The two-moment scheme. *Atmos. Res.*, **45,** 3-39.

Milbrandt, J. A. and M. K. Yau, 2005: A multi-moment bulk microphysics parameterization. Part I: Aanlysis of the role of the spectral shape parameter. *J. Atmos. Sci.*, **62,** 3051-3064.

——, 2005: A multi-moment bulk microphysics parameterization. Part II: A proposed three-moment closure and scheme description. *J. Atmos. Sci.*, **62,** 3065-3081.

——, 2006: A multimoment bulk microphysics parameterization. Part IV: Sensitivity experiments. *J. Atmos. Sci.*, **63,** 3137-3159.

——, 2006: A multimoment bulk microphysics parameterization. Part III: Control simulation of a hailstorm. *J. Atmos. Sci.*, **63,** 3114-3136.

Morrison, H., G. Thompson, and V. Tatarskii, 2008: Impact of cloud microphysics on the development of trailing stratiform precipitation in a simulated squall line: Comparison of one- and two-moment schemes. *Mon. Wea. Rev.*, In Press.

Murakami, M., 1990: Numerical modeling of dynamic and microphysical evolution of an isolated convective cloud-The 19 July 1981 CCOPE cloud. *J. Meteor. Soc. Japan.,* **68,** 107-127.

Nickerson, E. C., E. Richard, R. Rosset, and D. R. Smith, 1986: The numerical simulation of clouds, rain and air flow over the Vosges and Black Forest Mountains: A meso-beta-model with parameterized microphysics. *Mon. Wea. Rev.,* **114,** 398-414.

Pruppacher, H. R. and J. D. Klett, 1978: *Microphysics of Clouds and Precipitation*. D. Reidel Publishers, 714 pp.

Reisner, J., R. M. Rasmussen, and R. T. Bruintjes, 1998: Explicit forecasting of supercooled liquid water in winter storms using the MM5 mesoscale model. *Quart. J. Roy. Meteor. Soc.*, **124,** 1071–1107.

Roebber, P. J., D. M. Schultz, and R. Romero, 2002: Synoptic regulation of the 3 May 1999 tornado outbreak. *Wea. Forecasting,* **17,** 399-429.

Rogers, R. R. and M. K. Yau, 1989: *A Short Course in Cloud Physics*. 3rd ed. Pergamon Press, 293 pp.

Romine, G. S., D. C. Dowell, and R. B. Wilhelmson, 2008: Bridging the gap between observed and simulated supercell cold pool characteristics. *24th Conf. Severe Local Storms,* Savannah, GA, Amer. Meteor. Soc., 15.6.

Romine, G. S., D. W. Burgess, and R. B. Wilhelmson, 2008: A dual-polarization-radar-based assessment of the 8 May 2003 Oklahoma City area tornadic supercell. *Mon. Wea. Rev.,* **136,** 2849-2870.

Rotunno, R. and J. B. Klemp, 1982: The influence of the shear-induced pressure gradient on thunderstorm motion. *Mon. Wea. Rev.,* **110,** 136-151.

——, 1985: On the rotation and propagation of simulated supercell thunderstorms. *J. Atmos. Sci.,* **42,** 271-292.

Schlesinger, R. E., 1980: A three-dimensional numerical model of an isolated thunderstorm. Part II: Dynamics of updraft splitting and mesovortex couplet evolution. *J. Atmos. Sci.,* **37,** 395-420.

Schultz, P., 1995: An explicit cloud physics parameterization for operational numerical weather prediction. *Mon. Wea. Rev.*, **123,** 3331-3343.

Seifert, A., 2008: On the parameterization of evaporation of raindrops as simulated by a one-dimensional rainshaft model. *J. Atmos. Sci.*, **65,** 3608-3619.

Seifert, A. and K. D. Beheng, 2001: A double-moment parameterization for simulating autoconversion, accretion and selfcollection. *Atmos. Res.*, **59-60,** 265-281.

——, 2006: A two-moment cloud microphysics parameterization for mixed-phase clouds. Part 1: Model description. *Meteor. Atmos. Phys.*, **92,** 45-66.

Seifert, A., A. Khain, A. Pokrovsky, and K. D. Beheng, 2006: A comparison of spectral bin and two-moment bulk mixed-phase cloud microphysics. *Atmos. Res.*, **80,** 46-66.

Skamarock, W. C. and M. L. Weisman, 2009: The impact of positive-definite moisture transport on NWP precipitation forecasts. *Mon. Wea. Rev.*, **137,** 488-494.

Skamarock, W. C., J. B. Klemp, J. Dudhia, D. O. Gill, D. M. Barker, W. Wang, and J. D. Powers, 2005: A Description of the Advanced Research WRF Version 2, 88 pp.

Smith, P. L., 2003: Raindrop size distributions: exponential or gamma; does the difference matter? *J. Appl. Meteor.*, **42,** 1031-1034.

Snook, N. and M. Xue, 2006: Sensitivity of supercell tornado simulations to variations in microphysical parameters. *Preprint, Fourth Joint Korea-U.S. Workshop on Mesoscale Observation, Data Assimilation and Modeling for Severe Weather*, Soul, Korea.

——, 2008: Effects of microphysical drop size distribution on tornadogenesis in supercell thunderstorms. *Geophys. Res. Lett.*, **35,** L24803, doi:10.1029/2008GL035866.

Snyder, J. C., D. T. Dawson, and H. B. Bluestein, 2006: Tornadoes associated with cold-core, closed 500mb lows: The 20 March 2006, northwestern Oklahoma tornadoes. *23rd Conf. on Severe Local Storms*, St. Louis, MO, Amer. Meteor. Soc., P1.2.

Speheger, D. A., C. A. Doswell, and G. J. Stumpf, 2002: The Tornadoes of 3 May 1999: Event verification in Central Oklahoma and related issues. *Wea. Forecasting*, **17,** 362-381.

Straka, J. M. and J. R. Anderson, 1993: Numerical simulations of microburst producing storms: Some results from storms observed during COHMEX. *J. Atmos. Sci.*, **50,** 1329-1348.

Straka, J. M. and E. R. Mansell, 2005: A bulk microphysics parameterization with multiple ice precipitation categories. *J. Appl. Meteor.***,** Accepted.

Suzuki, O., H. Niino, H. Ohno, and H. Nirasawa, 2000: Tornado-producing mini supercells associated with Typhoon 9019. *Mon. Wea. Rev.*, **128,** 1868-1882.

Tao, W.-K. and J. Simpson, 1993: Goddard cumulus ensemble model. Part I: Model description. *Terres. Atmos. Ocean Sci.*, **4,** 35-72.

Tao, W.-K., J. Simpson, and M. McCumber, 1989: An ice-water saturation adjustment. *Mon. Wea. Rev.*, **117,** 231-235.

Testud, J., S. Oury, R. A. Black, P. Amayenc, and X. Dou, 2001: The concept of "normalized" distribution to describe raindrop spectra: a tool for cloud physics and cloud remote sensing. *J. Appl. Meteor.*, **40,** 1118-1140.

Thompson, R. L. and R. Edwards, 2000: An overview of environmental conditions and forecast implications of the 3 May 1999 tornado outbreak. *Wea. Forecasting*, **15,** 682-699.

Tzivion, S., G. Feingold, and Z. Levin, 1989: The evolution of raindrop spectra. Part II: Collisional collection/breakup and evaporation in a rainshaft. *J. Atmos. Sci.*, **46,** 3312-3328.

Ulbrich, C. W., 1983: Natural variations in the analytical form of the raindrop size distribution. *J. Climate Appl. Meteor.*, **22,** 1204-1215.

van den Heever, S. C. and W. R. Cotton, 2004: The impact of hail size on simulated supercell storms. *J. Atmos. Sci.*, **61,** 1596-1609.

Waldvogel, A., 1974: The N0-jump of raindrop spectra. *J. Atmos. Sci.*, **31,** 1067-1078.

Walko, R. L., W. R. Cotton, M. P. Meyers, and J. L. Harrington, 1995: New RAMS cloud microphysics parameterization. Part I: The single-moment scheme. *Atmos. Res.*, **38,** 29-62.

Wang, C. and J. S. Chang, 1993: A three-dimensional numerical model of cloud dynamics, microphysics, and chemistry. 1. concepts and formulation. *J. Geophys. Res.*, **98,** 14827-14844.

Weisman, M. L. and J. B. Klemp, 1982: The dependence of numerically simulated convective storms on vertical wind shear and buoyancy. *Mon. Wea. Rev.*, **110,** 504-520.

——, 1984: The structure and classification of numerically simulated convective storms in directionally varying wind shears. *Mon. Wea. Rev.*, **112,** 2479-2498.

Wicker, L. J. and R. B. Wilhelmson, 1993: Numerical simulation of tornadogenesis within a supercell thunderstorm. The Tornado: Its Structure, Dynamics,

Prediction and Hazards. *Geophys. Monogr.*, **No. 79,** Amer. Geophys. Union, 75-88.

——, 1995: Simulation and analysis of tornado development and decay within a three-dimensional supercell thunderstorm. *J. Atmos. Sci.*, **52,** 2675-2703.

Wilhelmson, R. B. and J. B. Klemp, 1978: A numerical study of storm splitting that leads to long-lived storms. *J. Atmos. Sci.*, **35,** 1975-1986.

——, 1981: A three-dimensional numerical simulation of splitting severe storms on 3 April 1964. *J. Atmos. Sci.*, **38,** 1581-1600.

Xue, M., 2000: High-order monotonic numerical diffusion and smoothing. *Mon. Wea. Rev.*, **128,** 2853-2864.

Xue, M., K. K. Droegemeier, and P. R. Woodward, 1993: Simulation of tornado vortices within a supercell storm using adaptive grid refinement technique. *Preprints, 17th Conf. on Severe Local Storms, St. Louis, MO,* Amer. Meteor. Soc., 362-365.

Xue, M., K. K. Droegemeier, and V. Wong, 2000: The Advanced Regional Prediction System (ARPS) - A multiscale nonhydrostatic atmospheric simulation and prediction tool. Part I: Model dynamics and verification. *Meteor. Atmos. Physics,* **75,** 161-193.

Xue, M., D.-H. Wang, J.-D. Gao, K. Brewster, and K. K. Droegemeier, 2003: The Advanced Regional Prediction System (ARPS), storm-scale numerical weather prediction and data assimilation. *Meteor. Atmos. Physics*, **82,** 139-170.

Xue, M., K. K. Droegemeier, V. Wong, A. Shapiro, K. Brewster, F. Carr, D. Weber, Y. Liu, and D.-H. Wang, 2001: The Advanced Regional Prediction System (ARPS) - A multiscale nonhydrostatic atmospheric simulation and prediction tool. Part II: Model physics and applications. *Meteor. Atmos. Phy.*, **76,** 143-165.

Xue, M., K. K. Droegemeier, V. Wong, A. Shapiro, K. Brewster, F. Carr, D. Weber, Y. Liu, and D. Wang, 2001: The Advanced Regional Prediction System (ARPS) - A multi-scale nonhydrostatic atmospheric simulation and prediction tool. Part II: Model physics and applications. *Meteor. Atmos. Phys.*, **76,** 143-166.

Zalesak, S. T., 1979: Fully multidimensional flux-corrected transport algorithms for fluids. *J. Comput. Phys.*, **31,** 335-362.

Zhang, G., J. Sun, and E. A. Brandes, 2006: Improving parameterization of rain microphysics with disdrometer and radar observations. *J. Atmos. Sci.*, **63,** 1273-1290.

Zhang, G., M. Xue, Q. Cao, and D. Dawson, 2008: Diagnosing the intercept parameter for exponential raindrop size distribution based on video disdrometer observations: model development. *J. Appl. Meteor. Climatol.,* **47,** 2983-2992.

Zhang, J., F. Carr, and K. Brewster, 1998: ADAS cloud analysis. *Preprints, 12th Conf. on Num. Wea. Pred.*, Phoenix, AZ., Amer. Met. Soc., 185-188.

Ziegler, C. L., 1985: Retrieval of thermal and microphysical variables in observed convective storms. Part I: Model development and preliminary testing. *J. Atmos. Sci.*, **42,** 1487-1509.